Cascade Organic Photovoltaics

by

Adam Joseph Barito

A dissertation submitted in partial fulfillment
of the requirements for the degree of
Doctor of Philosophy
(Materials Science and Engineering)
in The University of Michigan
2015

Doctoral Committee:

Professor Max Shtein, Chair
Professor Stephen R. Forrest
Professor Peter F. Green
Professor Jinsang Kim

© 2015 Adam Joseph Barito
All Rights Reserved

ACKNOWLEDGEMENTS

Any and all of the work presented in this thesis would not have been possible without the teachings and/or support from the many people I've known during my last five years in Ann Arbor. I'm going to attempt to properly thank everyone here, but there's a good chance I leave somebody out. If I do, it's only because I'm forgetful.

First, I have to acknowledge the members of the Shtein group. I knew nothing of organic electronics before coming here, but I've learned so much from all of you. Thanks to Nina Abani, Sneha Agarwal, Kanika Agrawal, Shaurjo Biswas, Sandro Gvakharia, Mark Hendryx, Yansha Jin, Gwan Ho Jung, Aaron Lamoureux, Steve Morris, Neil Poulin, Sam Raney, Erin Regan, Olga Shalev, Matt Sykes, and Jessa Webber. To Matt and Steve, especially, thank you for fielding the simplest of questions when I started, for training me on how to make and test devices, and for teaching me more about device physics than I thought possible. Matt, you and I both know just about everything in this thesis was a collaboration. To Kanika, I think it's more than fitting that we came in together and we go out together – I'll always appreciate our quiet friendship and getting to know you better towards the end of our time here. To Mark, we worked on some tough projects together – they may not have ended as we hoped, but there's something to be said for fighting through them. I'm glad we did that together. To Sam, my first undergrad that "clicked", I can't emphasize enough how impressed I've been with your work and your work ethic. The final chapter of this thesis wouldn't have happened without your

help (I knew I could ask you to make and test a device and have no doubt it would be done correctly). Any future employer will be lucky to have you. To Jessa and Sneha, I wish we could have started working together a little sooner, but I'm still so impressed with what you've accomplished in such a short amount of time. Jessa, the GUI for the EQE code will be a useful tool for many, and Sneha, I still think you've got a shot at hitting 10% with those tandem devices. To all in the Shtein group, thanks for your camaraderie. You've been my closest friends here, and I wouldn't have made it through some of the tougher times without you.

A great many thanks are due to my family and friends who've kept me sane and always moving forward. Mom and Dad, I will always appreciate the way you've pushed and loved and supported me. I know sometimes you worry I'm working too hard, but I'm not even sure what else would be worth doing. At the end of the day, I'm not scared of failing because I know I'll have your support no matter what. Bobb, writing and recording music together has been a powerful antidote for any sadness and stress – let's keep doing it. Laura, I think our wavelengths are as close as they've ever been, and your surprise attendance at my defense was a big deal to me – let's keep fine-tuning those wavelengths. Zeke, maybe we're not related by blood, but your friendship (not affected by me falling off the grid for months at a time) has always been a steadying one. That box of PayDay bars during the last push in the lab couldn't have come at a better time. To those who shared drinks, and those who texted packets of solar-cell-luck, and those who sang bad karaoke with me, you know who you are – I'm thankful for all of you.

To my thesis committee, I am thankful for your support, insights, and willingness to teach me. Professor Green and Professor Kim, the collaborations between our groups

are apparent throughout this thesis and I'm thankful for the opportunity to work closely with you and your students. To Professor Forrest, I am grateful for your challenging questions and insights – this thesis is better for them. Finally, I am thankful for my advisor, Max Shtein, who convinced me to come to Ann Arbor during a chance meeting while I was on a grad school visit to Stanford. Max, your apparent excitement about research during that first meeting was every bit indicative of what was to come, and that enthusiasm has helped carry me through extended "droughts" in the lab more than a few times. I've learned so much from you about designing experiments, thinking critically, and (maybe most importantly) communicating scientific results clearly and in a manner that is aesthetically pleasing. Coming to the University of Michigan to join this group was an easy choice to make at the time, and with five years worth of collected experiences and data, I know I'd make the same choice again.

Now for the formal acknowledgements: This work was supported by the U.S. Department of Energy, Office of Basic Energy Sciences, as part of the Center for Solar and Thermal Energy Conversion, an Energy Frontier Research Center (Award No. DE-SC0000957). Additional support was provided by the National Science Foundation *via* Grant EFRI-ODISSEI #1240264 and by the Air Force Office of Scientific Research through Grant FA9550-12-1-0435. I thank the NSF for their support of this work *via* the National Science Foundation Graduate Student Research Fellowship under Grant No. 1256260.

TABLE OF CONTENTS

LIST OF TABLES

LIST OF FIGURES

ABSTRACT

Within the last decade, organic photovoltaics (OPVs) have emerged as a potentially viable part of the solution for carbon-neutral energy production due to their low cost, flexibility, and compatibility with large-scale, roll-to-roll processing. However, while the maximum theoretical efficiency of OPVs is only slightly below that of their inorganic counterparts, demonstrated OPV efficiencies have still only reached ~11%. While the cost and energy required to fabricate OPVs is lower than inorganic PVs, practical efficiency is a primary driver of adoption in the marketplace and OPV efficiencies must approach 15-20% before having a chance to become commercially competitive. In this thesis, we present our work on the relatively new class of cascade organic photovoltaics and through that work we discover some critical factors that must be resolved to enable significant further gains in OPV efficiencies.

In the first part of this thesis, we focus on the tradeoff between photo-absorption and exciton diffusion efficiencies in organic heterojunction solar cells. Working with planar (as opposed to bulk) heterojunction device architectures, we employ rigorous modeling and experiments to demonstrate the physical mechanisms by which energy can be lost in OPVs (namely non-radiative recombination of excitons, either *via* bulk recombination or parasitic quenching at traps or conductive interfaces) and detail the ways in which this tradeoff has been previously addressed. We show that MoO_3, a material frequently used in OPV cells as an anode buffer layer and work function modifier, quenches excitons. We propose a new type of anode

buffer layer to prevent quenching at the anode, which we term an exciton dissociation layer (EDL). By inserting an EDL into a single heterojunction (SHJ) device, an additional heterojunction is created, converting the device into a multiple (cascade) heterojunction (CHJ) structure. We establish that the multiple heterojunctions (termed "subjunctions") in CHJs are operating electrically in parallel and develop an optical and diffusion based model that can predict their external quantum efficiency. In the second part of the thesis, through a systematic combinatorial study, we develop practical design rules for CHJ devices, requiring that charge injection barriers be minimized and the maximum power point voltage of each subjunction be closely matched. Applying these design rules, we demonstrate a 40% improvement in PCE by introducing a thin transparent EDL into a SHJ device. In the third and final part of the thesis, we develop a new model for interlayer Förster resonant energy transfer (FRET) in OPVs and show that the FRET process (present in most devices) can actually significantly hinder device efficiencies. With this new model, we propose specific material and device design rules that if employed, can prevent any efficiency losses due to FRET and instead achieve major efficiency enhancements. While the specific materials following those design rules do not yet exist, we are still able to optimize devices using the new model and pre-existing materials, demonstrating a 93% improvement in power conversion efficiency for a CHJ with 4 absorbers (up to 7.3% demonstrated here) compared to an optimized SHJ device (3.7%).

Chapter 1

Introduction to Organic Photovoltaics

1.1 Introduction

Organic photovoltaics (OPVs) have recently emerged as a potentially inexpensive source of energy due to their low-cost of fabrication, short energy payback time, compatibility with flexible substrates,[1-5] and reported power conversion efficiencies greater than 11%.[6] However, when compared with their inorganic counterparts, OPVs still exhibit substantially lower short-circuit current densities (J_{sc}), owing largely to their limited coverage of the solar spectrum and non-radiative losses involving the diffusion and dissociation of strongly bound excitons during the photoconversion process. In this chapter, we will discuss the fundamental factors that determine the absorption and exciton diffusion efficiencies in OPVs. Then, once that groundwork has been laid, we will spend the ensuing chapters attempting to stretch the tradeoff that occurs between those efficiencies.

1.2 OPV Fundamentals

In their simplest configuration, modern OPV devices consist of four materials (though additional materials can be added to improve efficiency or increase functionality). Two of those materials, the electron donor (ED) and electron acceptor (EA) absorb photons and transport holes and electrons, respectively. The other two materials are electrodes (anode and cathode) used to apply an electric field for collecting those free charges as current (holes and electrons, respectively).

Generally, at least one electrode is semitransparent such that light can enter the device and be absorbed by the ED and EA layers. If the other electrode is completely reflective, then light makes two passes through the device, effectively increasing the path length and number of absorbed photons in the active layers. This type of cell with separate ED and EA layers was first introduced by C.W. Tang in 1986, and is by far the most ubiquitous and successful OPV architecture used today.[7] In the following sections, we will discuss the electrical, optical, and excitonic processes in these devices as well as the ways those processes can be characterized *via* experiment and modeling.

1.3 Current-Voltage Characteristics

For all photovoltaic devices (organic or inorganic), the current-voltage (*J-V*) behavior can be characterized by four major parameters, as shown in **Figure 1.1**.

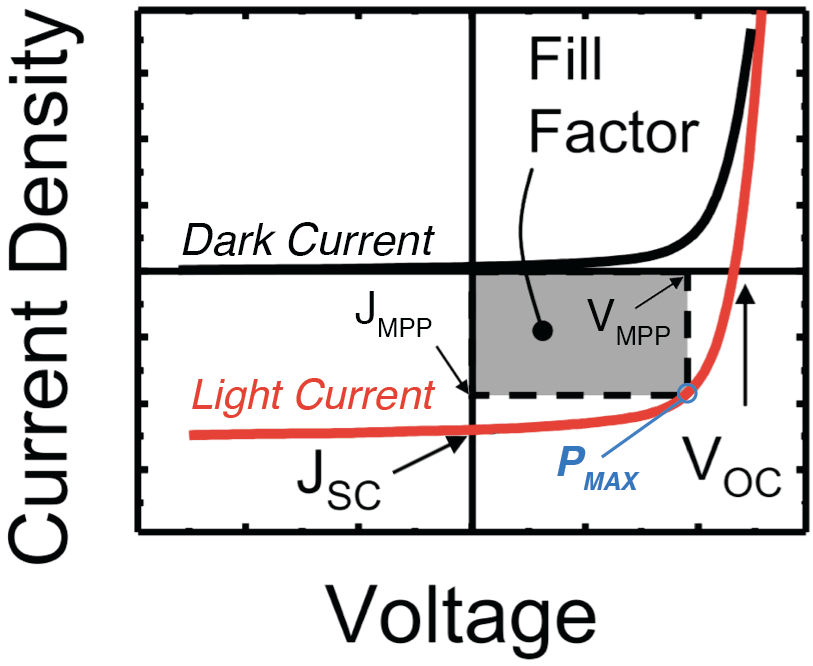

Figure 1.1 A characteristic plot (and important parameters) of current density (*J*) versus voltage for a solar cell. The dark current is the curve generated when the device is biased under dark conditions. The light current is the curve produced from the same device under illumination.

The power conversion efficiency (PCE) of the solar cell, defined as the electrical power out divided by optical power in, is determined by Equation (1.1):

$$PCE = \frac{J_{sc} \cdot V_{oc} \cdot FF}{P_{inc}} \tag{1.1}$$

where the short-circuit current density (J_{sc}) is the current density at zero bias, the open-circuit voltage (V_{oc}) is the bias at which the current density is zero, and P_{inc} is the power density of the incident light. The fill factor (FF) is a useful metric for describing the "squareness" of the light curve and compares the operating maximum power point (MPP) of the device to the "ideal" maximum power point that would come from operating at both J_{sc} and V_{oc} simultaneously.

$$FF = \frac{J_{MPP} \cdot V_{MPP}}{J_{sc} \cdot V_{oc}} \tag{1.2}$$

Throughout this thesis, we will primarily focus on improving the short-circuit current density of these devices in an effort to improve power conversion efficiency. J_{sc} is determined by:

$$J_{sc} = \int S(\lambda) \cdot EQE(\lambda) d\lambda + J_d \big|_{V=0} \tag{1.3}$$

Where $S(\lambda)$ is the wavelength-dependent spectrum of incident light from the sun, EQE is the wavelength-dependent external quantum efficiency of the solar cell, and J_d is the amount of current produced by the diode under dark conditions (no illumination). In **Figure 1.2**, we show the international standard AM1.5G solar spectrum and an example EQE spectrum containing one ED and one EA layer. Separate contributions to the EQE from the ED and EA layers are also plotted. The J_{sc}, as calculated from Equation (1.3), is plotted as the shaded gray region underneath the product of EQE and S(λ).

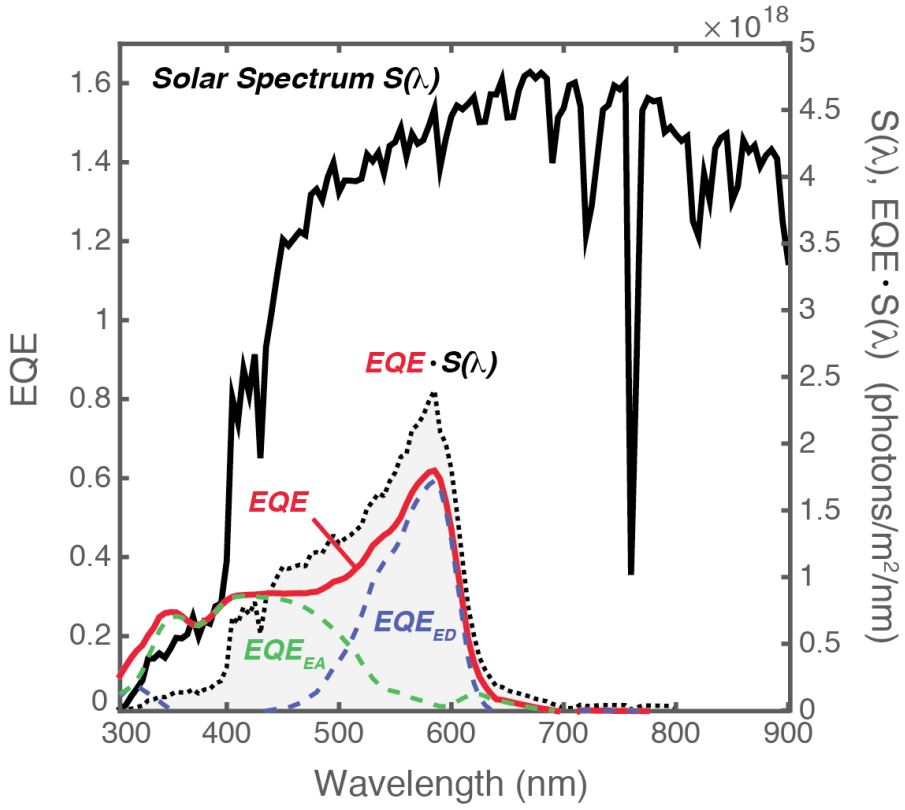

Figure 1.2 A plot of the solar spectrum $S(\lambda)$ (solid black); the external quantum efficiency spectrum of an example OPV device (solid red); EQE contributions from the ED (dotted blue) and EA (dotted green) layers; and the product of the EQE and solar spectrum (dashed black). The J_{sc} of the device is determined by the integral of EQE · S(λ), denoted by the filled gray area on the plot.

Because the solar spectrum is fixed (and J_d is negligible at short-circuit conditions), any improvements to the J_{sc} of OPVs must come from improving the EQE. To improve the EQE, we must first understand the specific physical properties in organic materials that determine the EQE, which we will now discuss.

1.4 Optically Generated Excitons

Upon absorption of a photon within a material, an electron gains energy and is promoted from the highest occupied molecular orbital (HOMO) level (valence band in inorganics) to the lowest unoccupied molecular orbital (LUMO) level (conduction band), leaving behind a hole. The electron and hole are attracted by an electrostatic Coulomb force, resulting in a exciton binding energy of $E_{B,exciton}$, determined by:

$$E_{B,exciton} = \frac{q^2}{4\pi\varepsilon_0\varepsilon_r r} \tag{1.4}$$

Where q is the electron charge, ε_0 is the permittivity of free space, ε_r is the relative permittivity (or dielectric constant) of the material, and r is the radius of the exciton. There are three types of excitons that can exist: Wannier-Mott, charge-transfer (CT), and Frenkel. Of the three, Wannier-Mott excitons have the lowest binding energy (on the order of 0.01 eV) and occur in materials where the dielectric constant is large (such as silicon, where $\varepsilon_r = 11.7$). These excitons have a radius larger than the lattice spacing and can be dissociated merely from thermal energy at room temperature. Thus Wannier-Mott excitons generated at room temperature are quickly dissociated into free charges. CT excitons exhibit an intermediate binding energy and radius compared to Frenkel and Wannier-Mott states, existing across adjacent molecules. Frenkel excitons have the highest binding energy of the three (on the order of 0.1 to 1 eV) and are generally localized to a single molecule. In organic films, the lower dielectric constant (~3) results in less charge screening and tightly bound Frenkel excitons residing in the HOMO and LUMO levels of one molecule.

1.5 Heterojunction at ED/EA Interface

Since Frenkel excitons in organic semiconductors are stable at room temperature and electrically neutral, externally applied electric fields cannot be used to separate them into free charges for collection as current. This requires additional device design considerations for OPVs compared to inorganic devices (where free charges are generated upon photon absorption). As previously noted, in 1986 C.W. Tang introduced the heterojunction OPV in which one electron-donating material and one electron-accepting material are used to separate charges. If the energy levels are aligned such that both the HOMO and LUMO of the ED are closer to the vacuum level than the

EA, then at the ED/EA interface the energy offset between the LUMO levels (or the HOMO levels) of the ED and EA cause the electron (hole) of an exciton to transfer to the adjacent EA (ED) molecule at the heterojunction. While excitons that charge transfer are still Coulombically bound between the ED and EA molecules across the heterojunction, the increased separation distance allows for an externally applied electric field to pull the charges apart for collection at their respective electrodes.

1.6 Exciton Diffusion and Loss Mechanisms

For the charge transfer process to occur, excitons must diffuse to the heterojunction. However, we note again that excitons are neutral quasi-particles so electric fields cannot be used to drive excitons in a preferred direction (i.e. toward the heterojunction). Instead, excitons diffuse isotropically within the ED and EA layers until they either recombine or reach the heterojunction to charge transfer.

1.6.1 Diffusion Mechanisms

Excitons diffuse in organic films *via* three main types of energy transfer: Dexter transfer, cascade energy transfer, and Förster resonant energy transfer (FRET).[8] In the case of Dexter transfer, excitons will diffuse through the film *via* a thermally activated "hopping" mechanism, with transfer occurring between neighboring molecules. In the cases of both cascade and Förster energy transfer, diffusion occurs over longer length scales and depends upon the emission spectrum of one molecule and the absorption spectrum of another. In the case of cascade energy transfer, excitons are transferred *via* radiative emission of a photon from one molecule and the subsequent absorption of that photon on another molecule. This energy transfer process occurs over large length scales, on the order of the absorption path length. FRET, on the other hand, is a non-radiative process in which dipoles between two molecules are Coulombically coupled.

While it can be helpful to consider FRET as the emission and absorption of a "virtual photon", no light is emitted during the Förster energy transfer process. FRET generally occurs over length scales of 1-100 nm. Until Chapter 4, we will only consider *intralayer* exciton diffusion, which primarily occurs *via* Dexter transfer and self-Förster transfer (i.e. non-radiative coupling between molecules of the same type). In Chapter 4, we will account for *interlayer* exciton diffusion, which can occur *via* Förster transfer of excitons between films of different materials. At that point, we will consider in detail the governing equations that determine the rate of Förster transfer between molecules.

1.6.2 Diffusion Loss Mechanisms

There are two major loss mechanisms that can prevent excitons from diffusing to the heterojunction (thus lowering η_{Diff}). The first mechanism is non-radiative recombination of excitons within the bulk, as shown in **Figure 1.4a**. Excitons have a characteristic lifetime (τ) and diffusion length (L_D) after which only 1/e of initially generated excitons will remain. If excitons recombine in the bulk of the material before reaching a heterojunction to undergo charge transfer, they will not contribute to photocurrent. The other major diffusion loss mechanism in OPVs is quenching of excitons at a trap or conductive interface. As we will discuss at length in Chapter 2, most electrodes act as efficient quenching interfaces where excitons can recombine. Again, if excitons recombine at a quenching interface before reaching a heterojunction they cannot contribute to photocurrent.

1.7 External Quantum Efficiency

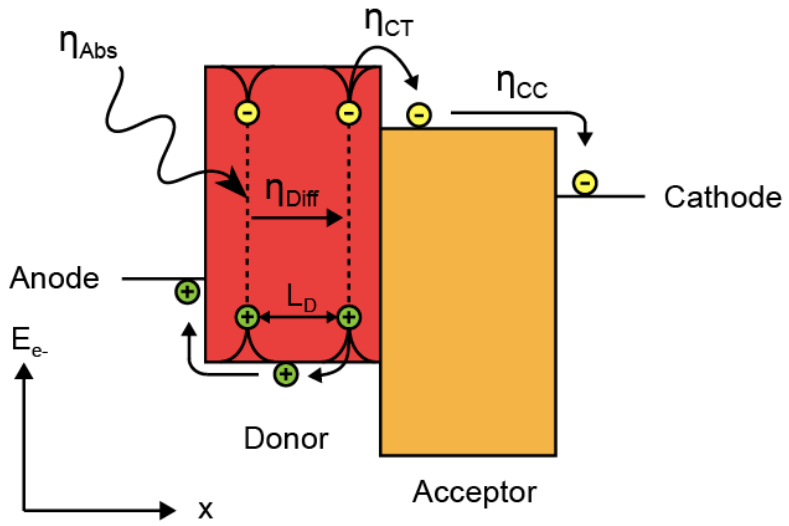

Figure 1.3 Energy level diagram of a planar bilayer organic photovoltaic device depicting the four major energy transfer steps during the photoconversion process.

As we have discussed thus far, the photoconversion process in OPVs consists of four major energy transfer steps, each of which is depicted in **Figure 1.3**, with a corresponding efficiency associated with each step.

$$EQE(\lambda) = \eta_{Abs}(\lambda) \cdot \eta_{Diff}(\lambda) \cdot \eta_{CT}(V_a) \cdot \eta_{CC}(V_a) \tag{1.5}$$

where $\eta_{Abs}, \eta_{Diff}, \eta_{CT}$, and η_{CC} correspond to the active layer photon absorption, exciton diffusion, exciton dissociation, and charge collection efficiencies, respectively.[9] As denoted in Equation (1.5), the absorption and exciton diffusion efficiencies are only wavelength dependent, while the charge transfer and charge collection efficiencies are only dependent on the applied voltage (V_a). For devices that do not have any abnormal energy barriers or other impediments at the heterojunction, we generally assume that any exciton that diffuses to a heterojunction will undergo charge transfer (i.e. η_{CT} = 100%) In the case of planar OPVs where the ED and EA layers are neat (i.e. not mixed), we can also assume η_{CC} = 100% at short-circuit conditions (for optimized devices, η_{CC} will remain close to unity until $V_a > V_{oc}$). Therefore, at least for planar

OPVs, we can calculate EQE at each wavelength by modeling η_{Abs} and η_{Diff}. We now consider in detail ways to model both. The code for the model (including additional modifications that we present in later chapters) can be found in the Appendix.

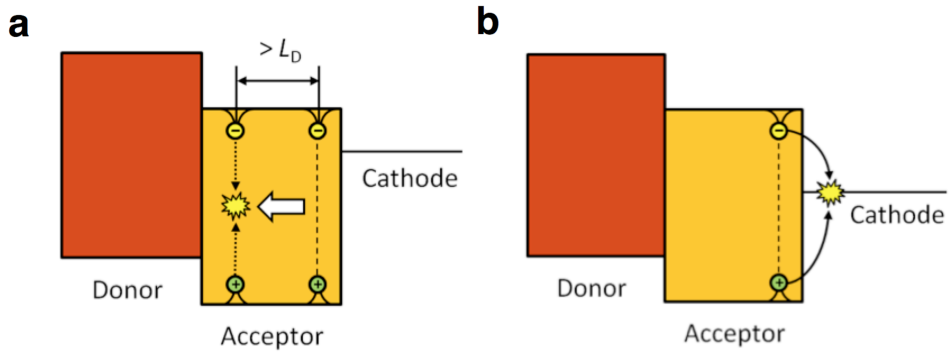

Figure 1.4 Possible exciton diffusion loss mechanisms in organic photovoltaics. a) non-radiative recombination in the bulk of the material. b) quenching at a conductive interface such as a trap or electrode.

1.7.1 Modeling Optical Fields

To calculate η_{Abs} for a device, we must carefully account for all optical properties of a thin film stack. Because the total thickness of organic and metal layers in OPVs are much thinner than the wavelengths of visible light (300 nm-1000 nm), our model must also account for any near-field constructive or destructive interference effects as well as phase changes due to propagation in each layer. Furthermore, we must account for where photons are being absorbed in the device – specifically in which layers they are being absorbed (i.e. photons that are parasitically absorbed in the electrodes will not have a chance to contribute to photocurrent), as well as the spatial position at which they are absorbed within each layer. To account for reflections at each interface as was as propagation through each layer, we use a transfer matrix formalism to model all of the optics in our devices. For the model to produce accurate predictions, we must know the refractive index and thickness of each layer to a high level of accuracy. We follow the general framework established by Pettersson *et al* (and further elaborated upon by Peumans *et al*.) which we will now detail below.[10,11]

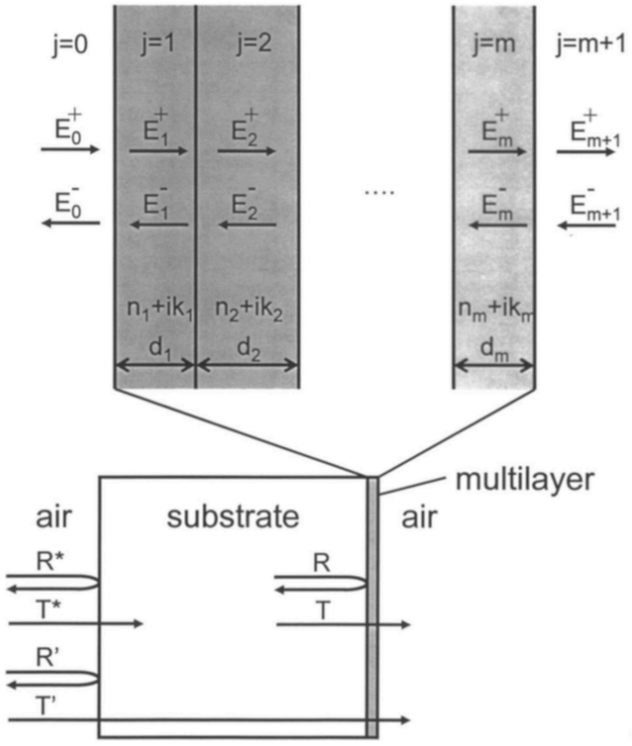

Figure 1.5 Geometry an example device stack used in the transfer matrix optical field simulations. Reflection and transmission are accounted for at each interface as well as any phase changes due to propagation through each layer. From Ref. [11]

Figure 1.5 provides a schematic for a generalized OPV device consisting of a thick (optically incoherent) substrate and *m* thin (optically coherent) layers. First, we can consider a plane wave (such as light from the sun) incident on the stack from a semi-infinite medium. At each interface, some fraction of the light will reflect and the rest will transmit (at an infinitesimally thin interface, there will be no absorption of the light). We can describe the reflection and transmission at each interface with an interface matrix:

$$I_{jk} = \frac{1}{t_{jk}} \begin{bmatrix} 1 & r_{jk} \\ r_{jk} & 1 \end{bmatrix} \tag{1.6}$$

where r_{jk} and t_{jk} are the Fresnel complex reflection and transmission coefficients at the interface between layers *j* and *k*.

For light propagating normal to the device (as is the case for all simulations presented in this thesis), the Fresnel coefficients are defined as:

$$r_{jk} = \frac{n_j - n_k}{n_j + n_k} \tag{1.7}$$

$$t_{jk} = \frac{2n_j}{n_j + n_k} \tag{1.8}$$

where n_j is the complex refractive index of layer j. The layer matrix, which accounts for phase change due to propagation through each layer is described by

$$L_j = \begin{bmatrix} e^{-i\xi_j d_j} & 0 \\ 0 & e^{-i\xi_j d_j} \end{bmatrix} \tag{1.9}$$

where, at normal incidence

$$\xi_j = \frac{2\pi}{\lambda} n_j \tag{1.10}$$

and λ is the wavelength of the incident light. We can then construct a total system matrix **S**

$$S = \begin{bmatrix} S_{11} & S_{12} \\ S_{21} & S_{22} \end{bmatrix} = \left(\prod_{i=1}^{m} I_{(i-1)i} L_i \right) \cdot I_{m(m+1)} \tag{1.11}$$

and relate the electric field in the outermost layers ($j = 0$ and $j = m + 1$) by

$$\begin{bmatrix} E_0^+ \\ E_0^- \end{bmatrix} = S \begin{bmatrix} E_{m+1}^+ \\ E_{m+1}^- \end{bmatrix} \tag{1.12}$$

where E_0^+ and E_0^- are the right and left propagating waves on the incident (leftmost) side, respectively, and E_{m+1}^+ and E_{m+1}^- are the right and left propagating waves on the rightmost side. For all simulations in this thesis, there is only incident light from one side, so E_{m+1}^+ is always zero. To determine the complex reflection and transmission coefficients for the entire stack, we can use elements from the entire system matrix, **S**:

$$t = \frac{E_{m+1}^{+}}{E_0^{+}} = \frac{1}{S_{11}} \tag{1.13}$$

$$r = \frac{E_0^{-}}{E_0^{+}} = \frac{S_{21}}{S_{11}} \tag{1.14}$$

However, for simulating the EQE, what we care about the most are photons being absorbed within the active layers. In order to calculate the electric field profile within any layer *j* in the stack, we can separate the system into two subsets surrounding layer *j*. We can then write the total layer matrix as

$$S = S_j^{-} L_j S_j^{+} \tag{1.15}$$

where

$$S_j^{-} = \left(\prod_{n=1}^{j-1} I_{(n-1)n} L_n \right) I_{(j-1)j} \tag{1.16}$$

and

$$S_j^{+} = \left(\prod_{n=j+1}^{m} I_{(n-1)n} L_n \right) I_{m(m+1)} \tag{1.17}$$

Finally, we can relate the electric fields propagating in the positive and negative directions at the left interface to the incident plane wave by

$$\frac{E_j^{+}}{E_0^{+}} = t_j^{+} = \frac{\dfrac{1}{S_{j11}^{-}}}{1 + \dfrac{S_{j12}^{-} S_{j21}^{+}}{S_{j11}^{-} S_{j11}^{+}} e^{i2\xi_j d_j}} \tag{1.18}$$

$$\frac{E_j^{-}}{E_0^{+}} = t_j^{-} = t_j^{+} \frac{S_{j21}^{+}}{S_{j11}^{+}} e^{i2\xi_j d_j} \tag{1.19}$$

To calculate the total electric field within layer *j*, we add the positive and negative propagating electric fields together and account for phase change due to propagation through the layer

$$E_j(x) = E_j^+(x) + E_j^-(x) = (t_j^+ e^{i\xi_j x} + t_j^- e^{-i\xi_j x})E_0^+ \tag{1.20}$$

1.7.2 Modeling Exciton Generation

Upon solving the transfer matrix, we can determine the optical electric field at each wavelength for any point within any material in the device. Accounting for the electric field intensity within each layer and the attenuation of the electric field due to the imaginary part of each layer's refractive index (k), we can calculate the amount of absorbed power, Q(x) at any point in the device:

$$Q_j(x) = \frac{c\varepsilon_0}{2} \cdot \frac{4\pi k_j n_j}{\lambda n_0 \cos(\theta_0)} \left|E_j(z)\right|^2 \tag{1.21}$$

where c is the speed of light, ε_0 is the permittivity of free space, k_j and n_j are the imaginary and real components of the refractive index, respectively, n_0 is the refractive index of the surrounding medium, and θ_0 is the incidence angle of the incoming light in the surrounding medium.[10] From there, we can calculate the optical exciton generation rate (G_A) at any point in any layer *j* using Equation (1.22).

$$G_A = \frac{Q(x)}{h\upsilon} \tag{1.22}$$

where h is Planck's constant and v is the frequency of the incoming light.

1.7.3 Modeling Exciton Diffusion and Solving for the Steady State Exciton Population Density in OPV Active Layers

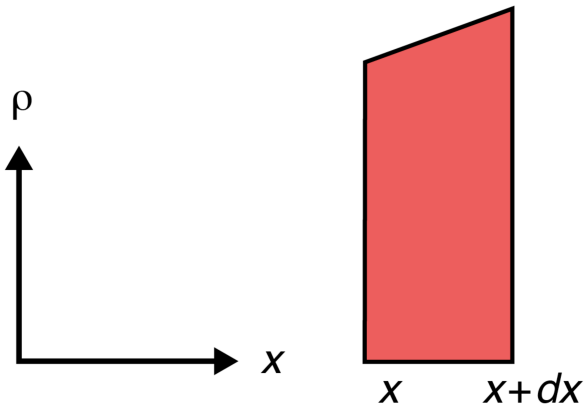

Figure 1.6 A control volume to be considered within an active layer.

To simulate exciton diffusion within the active layers, we use the standard Feng-Ghosh model,[12] which we will now present. If we consider a control volume of width *dx* within the active layer and perform a mass balance on the exciton density between *x* and *x*+*dx*, we can determine the overall change in exciton density as a function of time, which gives

$$\frac{\partial \rho}{\partial t} = J\Big|_x - J\Big|_{x+dx} - \frac{\rho}{\tau} + G_A \tag{1.23}$$

where ρ is the spatially varying exciton population density within the layer, t is time, J is the exciton flux, τ is the characteristic exciton lifetime, hv is the energy of the incident photon, and G_A is the time-averaged absorbed power as determined in Section 1.7.2. In Equation (1.23) the first two terms on the right represent exciton diffusion into and out of the control volume, the second term represents exciton recombination in the bulk, and the third term corresponds to the exciton photogeneration rate. For very small *dx*, we can approximate:

$$\frac{\partial J}{\partial x} = J\Big|_x - J\Big|_{x+dx} \tag{1.24}$$

Using Fick's first law to describe exciton diffusion

$$J = -D\frac{\partial \rho}{\partial x} \tag{1.25}$$

taking its derivative

$$-\frac{\partial J}{\partial x} = \left(\frac{\partial D}{\partial x}\right)\left(\frac{\partial \rho}{\partial x}\right) + D\frac{\partial^2 \rho}{\partial x^2} \tag{1.26}$$

and substituting into Equation (1.23), we get

$$\frac{\partial \rho}{\partial t} = \left(\frac{\partial D}{\partial x}\right)\left(\frac{\partial \rho}{\partial x}\right) + D\frac{\partial^2 \rho}{\partial x^2} - \frac{\rho}{\tau} + G_A \tag{1.27}$$

If we assume steady state conditions (no changes in ρ versus time) and a constant diffusivity (no spatial changes in D within the layer), then the term on the left and the first term on the right go to zero and we arrive at the standard drift-diffusion model.

$$0 = D\frac{d^2 \rho}{dx^2} - \frac{\rho}{\tau} + G_A \tag{1.28}$$

We note here that we can also define the diffusivity in terms of measureable quantities, the exciton diffusion length and lifetime:

$$D = \frac{L_D^2}{\tau} \tag{1.29}$$

Now we can determine a numerical solution for the exciton population profile by imposing boundary conditions at the active layer interfaces. As seen in **Figure 1.7**, there are three boundary conditions that we can apply at active layer interfaces. For the cases of a heterojunction (where charge transfer occurs) or a quenching interface such as a conductive electrode (where non-radiative recombination occurs), the exciton population is constrained to be zero. In the case of a perfectly reflecting interface, the slope of the exciton population density is set to zero.

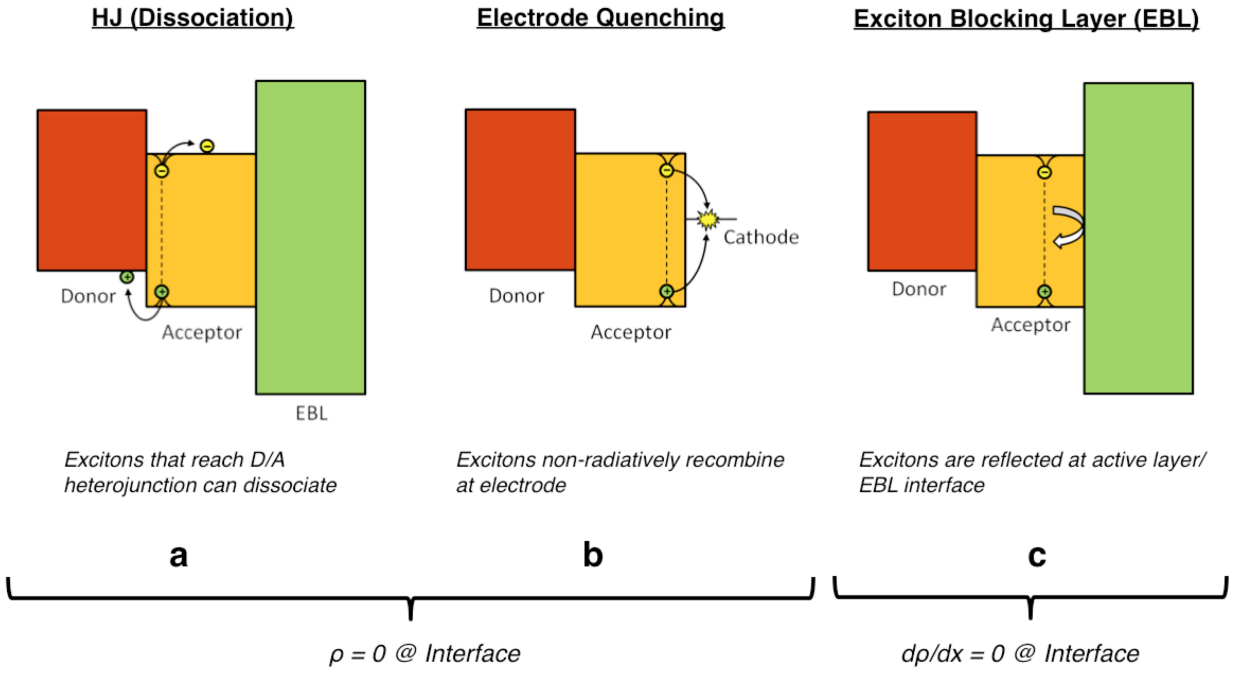

Figure 1.7 Possible steady state exciton boundary conditions that can be applied at active layer interfaces. At a) heterojunctions and b) quenching interfaces, the exciton population density is set to zero. At reflecting interfaces such as an exciton blocking layer, the slope of the exciton population density is set to zero (i.e. the flux of excitons at that interface is zero).

To solve Equation (1.28) at each mesh point, we use finite difference approximations for the first and second spatial derivatives of the exciton population density:

$$\frac{d\rho}{dx} = \frac{\rho_{i+1} - \rho_{i-1}}{2dx} \tag{1.30}$$

$$\frac{d^2\rho}{dx^2} = \frac{\rho_{i+1} + \rho_{i-1} - 2\rho_i}{dx^2} \tag{1.31}$$

Substituting those approximations into Equation (1.28) and multiplying both sides by D, we get

$$\frac{\rho_{i+1} + \rho_{i-1} - 2\rho_i}{dx^2} - \frac{\rho}{D\tau} + \frac{G_A}{D} = 0 \tag{1.32}$$

Finally, we move the generation rate term to the right side and multiply both sides by dx^2:

$$\rho_{i-1} - \left(2 + \frac{dx^2}{D\tau}\right)\rho_i + \rho_{i+1} = -\frac{dx^2}{D}G_A \tag{1.33}$$

Now we have a set of equations that govern the steady state exciton population density at each mesh point *i*. With the first and last rows of our matrix, we can set the necessary boundary conditions. Setting $\rho = 0$ for a quenching or dissociating interface is straightforward (we merely set ρ_1 or $\rho_n = 0$). To set the slope of ρ to zero for a reflecting interface, we employ the finite different approximation for the first derivative as provided in Equation (1.30). Simply, ρ_{i+1} must be set equal to ρ_{i-1}. Substituting this identity into Equation (1.28), we get

$$2\rho_{i-1} - \left(2 + \frac{dx^2}{D\tau}\right)\rho_i = -\frac{dx^2}{D}G_A \tag{1.34}$$

To demonstrate how to set up the matrix for solving the steady state population density, we show an example in Equation (1.35) where the population density is set to zero at x = 0 ($i = 1$) and the slope of the population density is set to zero at the last point of the layer ($i = n$).

$$\begin{bmatrix} 1 & 0 & 0 & 0 \cdots 0 & 0 & 0 \\ 1 & -\left(2+\frac{dx^2}{D\tau}\right) & 1 & 0 \cdots 0 & 0 & 0 \\ 0 & 1 & -\left(2+\frac{dx^2}{D\tau}\right) & 1 \cdots 0 & 0 & 0 \\ \vdots & \vdots & \vdots & \vdots \ddots \vdots & \vdots & \vdots \\ 0 & 0 & 0 & 0 \cdots 1 & -\left(2+\frac{dx^2}{D\tau}\right) & 1 \\ 0 & 0 & 0 & 0 \cdots 0 & 2 & -\left(2+\frac{dx^2}{D\tau}\right) \end{bmatrix} \cdot \begin{bmatrix} \rho_1 \\ \rho_2 \\ \rho_3 \\ \vdots \\ \rho_{n-1} \\ \rho_n \end{bmatrix} = \begin{bmatrix} 0 \\ G_{A,2} \\ G_{A,3} \\ \vdots \\ G_{A,n-1} \\ G_{A,n} \end{bmatrix} \tag{1.35}$$

Finally, to determine the exciton population density at each mesh point *i* (ρ_i), we divide the matrix on the right side by the leftmost matrix to solve for a vector of values from ρ_1 to ρ_n.

1.7.4 Internal Quantum Efficiency

We also note that it can be helpful to separate changes in absorption from other processes comprising EQE by defining the IQE as (assuming no voltage dependence)

$$\eta_{IQE}(\lambda) = \frac{\eta_{EQE}(\lambda)}{\eta_{Abs}(\lambda)} \tag{1.36}$$

which describes the efficiency of converting photogenerated excitons into electrical current. In planar devices where we assume η_{CT} and η_{CC} to be unity, then we can assume that IQE = η_{Diff}. At times in this thesis, we will consider both EQE and IQE as metrics for understanding device operation and performance.

1.7.5 Potential Modifications to the EQE Model

Throughout the rest of this thesis, we will propose additional modifications to the drift-diffusion part of the EQE model to more accurately account for exciton diffusion and energy transfer within OPVs. Specifically, we will account for the existence of multiple heterojunctions in Chapter 2 and interlayer Förster resonant energy transfer in Chapter 4.

1.8 Absorption/Diffusion Bottleneck in OPVs

1.8.1 Inherent Tradeoff Between Diffusion and Absorption Lengths

While the optical absorption length (L_A) of typical organic materials used for active layers is ~30-100 nm, the characteristic diffusion length (L_D) for photogenerated excitons is approximately an order of magnitude lower (~5-20 nm),[11,13] leading to an efficiency trade-off with respect to layer thickness.[7,9] As we've established, the photoconversion process in OPVs requires that optically generated, tightly bound excitons diffuse to the heterojunction interface between electron donating and electron accepting materials. Upon reaching the heterojunction,

excitons undergo charge-transfer and the resulting free charges can be collected at the electrodes.[11]

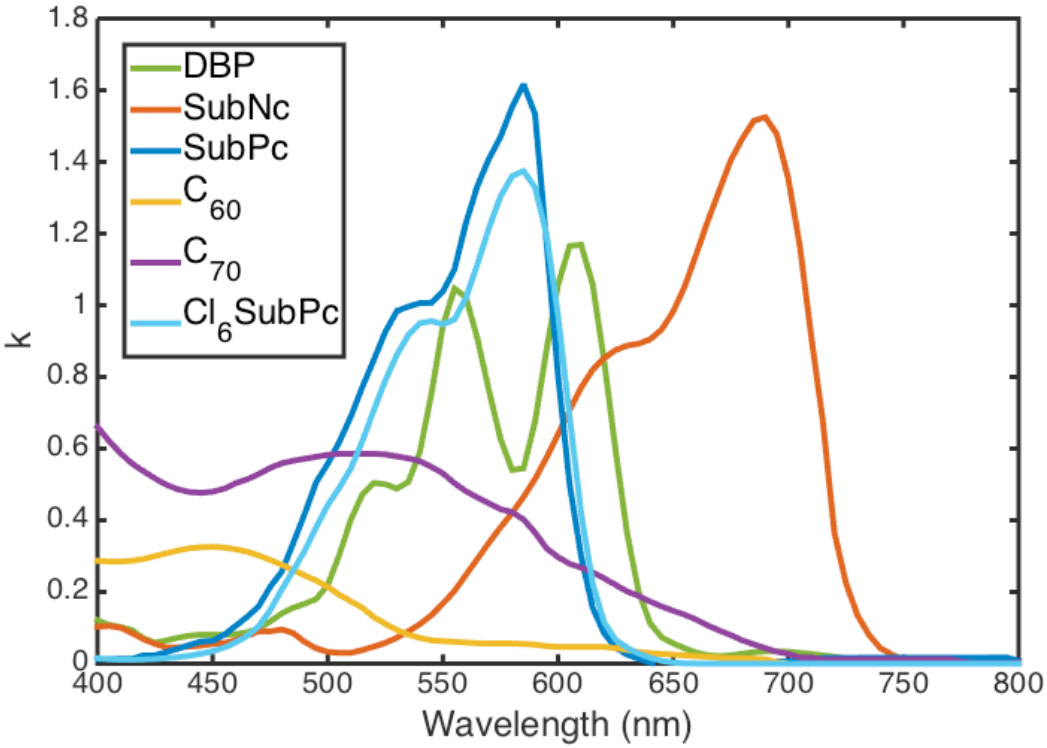

Figure 1.8 Extinction coefficients versus wavelength for commonly used active materials in OPVs. Most organic materials have relatively sharp absorption peaks, resulting in poor coverage of the solar spectrum.

In **Table 1.1**, we provide L_D and L_A values for common organic materials used as active layers in OPV devices. The extinction coefficients (the imaginary part of the refractive index) for each material are shown in **Figure 1.8**. Since the absorption length is a wavelength-dependent property, we calculate it at the peak absorption wavelength (greater than 400 nm) for each material. The quantities are defined as such: L_D is the distance from the point of exciton generation where 1/e excitons remain (have not recombined in the bulk) and L_A is the distance of light propagation into a material where 1/e of the original photons remain (have not been absorbed by the material). L_A for each material is calculated as the inverse of the absorption coefficient, or

$$L_A = \frac{\lambda}{4\pi k} \tag{1.37}$$

Even at the absorption peak of each material (where L_A is minimized), the ratio of L_D/L_A ranges from 0.13 – 0.3. Off of the peak absorption, that ratio will decrease further, which is a significant issue due to the narrow absorption peaks of most organic materials.

Table 1.1 Absorption and exciton diffusion lengths for common active materials used in OPV devices.

Material	L_D (nm)	L_A (nm)	L_D/L_A	Abs. Peak (nm)
Electron Donors				
DBP	8	42	0.19	610
SubNc	6	26	0.17	690
SubPc	8.5	29	0.30	585
Electron Acceptors				
C_{60}	17	109	0.16	450
C_{70}	17	70	0.24	520
Cl_6SubPc	4.5	34	0.13	585

While many attempts have been made to bypass the absorption/diffusion bottleneck, either by improving absorption efficiency or diffusion efficiency, the tradeoff has yet to be fully mitigated. We present the two most ubiquitous and successful methods in the next section, and then will spend the ensuing chapters attempting to stretch the tradeoff even further.

1.8.2 Planar/Bulk Heterojunctions and Series Tandems

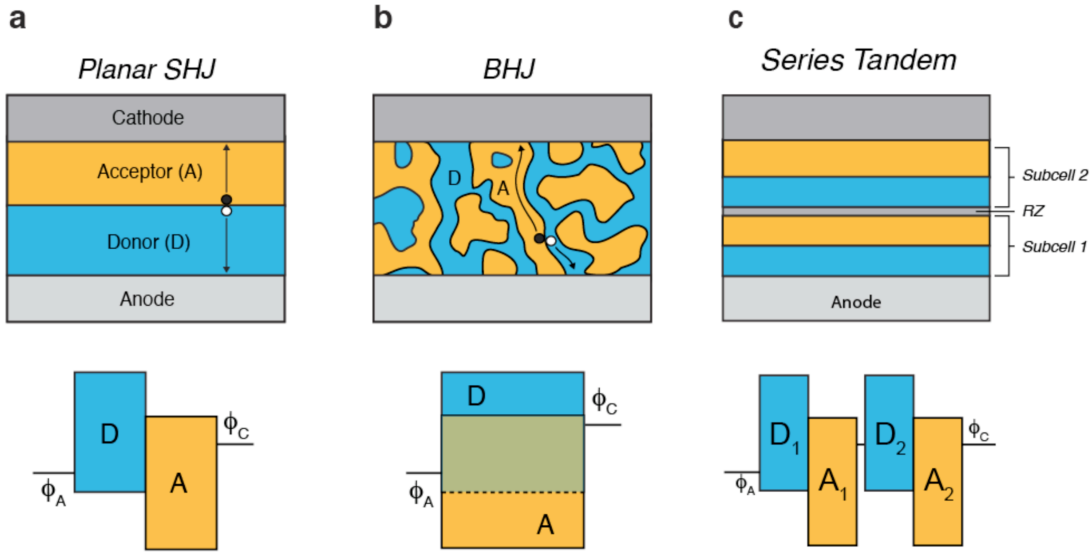

Figure 1.9 Device schematics and energy band diagrams for a) planar single heterojunction, b) bulk heterojunction, and c) series tandem OPV devices.

Thus far, we have discussed EQE modeling loosely in terms of planar device architectures (**Figure 1.9a**) in which there are discrete layers and a single interface for exciton dissociation. However, there have been two other major types of device architectures that have been used to partially circumvent the absorption/diffusion tradeoff: bulk heterojunctions (BHJs)[14-17] and vertically stacked, series-connected tandem devices.[18,19] In BHJs, the active layers are intermixed to create a spatially distributed heterojunction (**Figure 1.9b**). With careful morphological control, the size of any donor or acceptor domain within the bulk can be decreased to less than the active materials' L_D. Without the thickness limitation by L_D, the active layer thickness can be increased to improve absorption efficiency, although this can lead to an increase in non-geminate recombination.[20] Furthermore, control of the BHJ active layer morphology remains the primary challenge for both device optimization and materials design. In the case of series tandems, multiple subcells with complementary absorption peaks are used to achieve higher absorption efficiency across the visible spectrum (**Figure 1.9c**). The latter approach is generalizable, as the

subcells in principle can comprise either planar or bulk heterojunctions. However, because tandem devices are connected electrically in series, the resulting device performance is voltage-additive and current-limited by the lowest current of either subcell.[19]

1.9 Onsager-Braun Model for Simulating Photocurrent in OPVs

While the focus of this thesis is exciton generation and diffusion within OPVs at zero applied bias, simulating *J-V* curves is a necessary tool for predicting the actual PCE of devices under forward bias. In this section, we detail how the voltage dependence of photocurrent in OPV devices can be simulated using the Onsager-Braun (OB) model,[21] whereby bound polaron pairs (PPs) at the heterojunction are treated as Coulombically-bound charges with a fixed separation distance (a_0). The temperature-dependent, field-assisted dissociation rate of PPs (k_{PPd}) is described by:

$$k_{PPd} = \frac{3q}{4\pi\varepsilon_r\varepsilon_0 a_0^3}\exp\left(\frac{-E_{B,PP}}{k_b T}\right)\frac{J\left[2\sqrt{2}(-b)^{1/2}\right]}{\sqrt{2}(-b)^{1/2}} \tag{1.38}$$

where q is the electron charge, ε_r is the relative permittivity to the vacuum permittivity (ε_0), a_0 is the separation distance between the electron and hole, $k_B T$ is the thermal energy, and J is the first-order Bessel function. The PP binding energy ($E_{B,PP}$) is again the Coulombic binding energy between the electron and hole across the interface:

$$E_{B,PP} = \frac{q^2}{4\pi\varepsilon_r\varepsilon_0 a_0} \tag{1.39}$$

and the term b is defined as:

$$b = \frac{q^3(V_a - V_{bi})}{8\pi d\varepsilon_r\varepsilon_0 k_b^2 T^2} \tag{1.40}$$

where V_{bi} is the built-in voltage defined by the difference in Fermi levels in the organic layers adjacent to the contacts at zero bias, V_a is the applied bias voltage, and d is the thickness of the

active layers. In this thesis, we assume the net field in the active layers is constant as a function of position, which is a reasonable assumption as long as charge injection from the contacts is minimal below V_{bi}. Furthermore the study of photocurrent alone (and not total current) allows one to neglect the effects of charge injection and transport through the active layers and focus solely on the dynamics of the heterojunction. Along with a_0 and V_{bi}, the recombination rate (k_r) of the bound charges across the interface is then used as a fitting parameter, and the overall PP dissociation efficiency at the heterojunction can be defined as:

$$\eta_{PPd} = \frac{k_{PPd}}{k_{PPd} + k_r} \tag{1.41}$$

In the case where charge collection efficiency is 100% once the polaron pairs are dissociated (i.e. there are barrier free paths to each electrode), then $\eta_{CC} = \eta_{PPd}$. In Chapter 3 we will consider devices where η_{PPd} (and thus η_{CC}) drops precipitously at $V_a < V_{oc}$.

Chapter 2

Exciton Dissociation Layers and Cascade Heterojunction OPVs

Photocurrent generation in OPVs relies on exciton diffusion to the donor/acceptor heterojunction. Excitons that fail to reach the heterojunction are lost to recombination via quenching at the electrodes or relaxation in the bulk. Bulk recombination has been mitigated largely through the use of bulk heterojunctions, while quenching at the metal cathode has been previously circumvented through the introduction of exciton blocking layers that "reflect" excitons. Here, we introduce an alternative concept of a transparent exciton dissociation layer (EDL), a single layer that prevents exciton quenching at the electrode while also providing an additional interface for exciton dissociation. The additional heterojunction reduces the distance excitons must travel to dissociate, recovering the electricity-generating potential of excitons otherwise lost to heat. We model and experimentally demonstrate this concept in an archetypal subpthalocyanine/fullerene planar heterojunction OPV, generating an extra 66% of photocurrent in the donor layer (resulting in a 27% increase in short-circuit current density from 3.94 to 4.90 mA/cm^2). Because the EDL relaxes the trade-off between exciton diffusion and optical absorption efficiencies in the active layers, it has broad implications for the design of OPV architectures and offers additional benefits over the previously demonstrated exciton blocking layer for photocurrent generation.

2.1 Introduction

As was discussed in Chapter 1, significant problems with exciton management must be resolved before OPVs can compete with their inorganic counterparts for broad-based application. One such problem is non-radiative recombination of excitons at the organic/electrode interface, which lowers the internal quantum efficiency of the organic layer. Recombination at the electron acceptor/cathode interface has received the most attention to date, due to exciton quenching by metal clusters formed in the top-most regions of the organic layers during cathode deposition. This problem has been mitigated by inserting a buffer layer between the organic absorbing film and the cathode. Additionally, using a large bandgap material for the buffer layer results in an exciton blocking layer (EBL)[22,23] that reflects excitons before they reach the cathode. The EBL can also be tuned to improve electron injection and act as a spacer to increase the optical field intensity inside the absorbing layers. Several recent improvements have been made to cathode EBLs, including doping of the EBL to increase conductivity[24,25] and ensuring alignment of the LUMO level to facilitate low-resistance electron extraction.[26]

It is indeed possible that exciton quenching can occur at the anode. Molybdenum trioxide (MoO_3) is often used to increase the anode work function,[27] improving solar cell performance overall, yet our results indicate that MoO_3 actually quenches excitons in boron subphthalocyanine chloride (SubPc), contrary to previous reports.[28,29] Another widely used anodic buffer layer, poly(3,4-ethylenedioxythiophene):poly(4-styrene sulfonate) (PEDOT:PSS), has also been shown to quench excitons.[30] In these cases, and others where quenching may occur (eg. metallic anodes), it would be advantageous to introduce an additional buffer layer between the anode and donor layer. Anode EBLs have recently been shown to increase the short-circuit current density (J_{sc}) of OPVs by preventing quenching at the anode/donor interface.[31] However,

by introducing an entirely "passive" EBL that only reflects excitons, the net flux of excitons at the single heterojunction is increased only slightly, while a large portion of excitons generated nearest the EBL will still recombine parasitically in the bulk. Bulk heterojunctions (BHJs) have been used previously to mitigate bulk recombination,[14,16] but they can be limited by poor charge collection efficiency, especially under forward bias.[20]

In this work, we investigate the use of an exciton dissociation layer (EDL), an optically transparent layer that is placed between the anode and donor layer to prevent quenching. The principal difference between this EDL and a conventional EBL is that the EDL material is chosen such that its HOMO and LUMO levels are closer to the vaccum level than the donor layer, [32-35] facilitating exciton dissociation at the EDL/donor interface (**Figure 2.1b**). With the incorporation of such an EDL, the exciton concentration profile within the active layer is identical to the profile in the case of quenching at the electrode, but instead of being lost to parasitic recombination, the excitons at the EDL/active layer heterojunction also contribute to photocurrent (**Figure 2.2c**). By effectively decreasing the distance required for excitons to diffuse before dissociation, the EDL/donor heterojunction relaxes the requirement for long exciton diffusion lengths and improves the IQE of any given donor material. To be precise in our terminology, we define these types of OPVs as cascade heterojunction (CHJ) devices throughout the rest of this thesis. While CHJs are similar to other types of energy cascade OPVs that have been presented previously in the literature,[36,37], the main distinction between energy cascade and CHJ devices is that CHJs contain multiple spatially separated heterojunctions.

Below we validate the EDL/CHJ concept by fabricating devices with N,N'-bis(naphthalen-1-yl)-N,N'-bis(phenyl)-2,2'-dimethylbenzidine (α-NPD) inserted between SubPc and MoO_3 in an archetypal SubPc/C_{60} heterojunction OPV cell. This approach increases the photocurrent

contribution of SubPc by 66% (leading to a 27% enhancement in device J_{sc}), without changing the number of photons absorbed by SubPc. In other words, inserting the EDL substantially boosts the IQE of the SubPc layer. The EDL functionality is further confirmed with a rigorous physical model of EQE and IQE in CHJ structures.

2.2 Theory

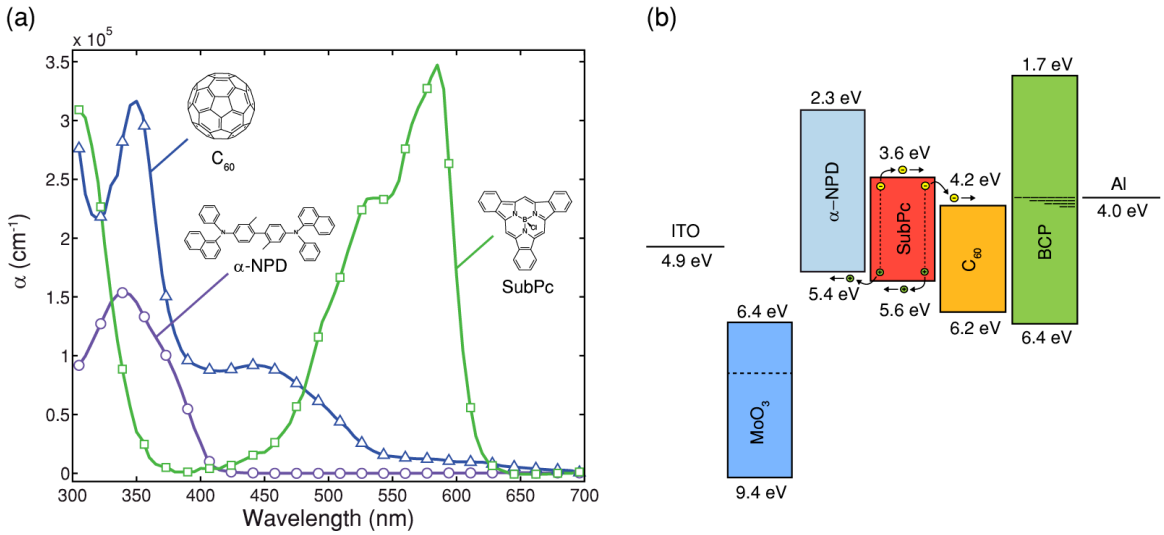

Figure 2.1 a) Active molecules used within this study and their absorption spectra calculated from refractive index values measured by spectroscopic ellipsometry. b) An energy level diagram for a SubPc/C_{60} device with an α-NPD exciton dissociation layer inserted between the SubPc and MoO_3 layers.

The molecules used in this study and their respective absorption coefficients are shown in **Figure 2.1a**. The base device structure employed is an archetypal planar SubPc/C_{60} heterojunction, which has been well studied.[38-42] In **Figure 2.1b**, an energy level diagram is shown for the devices under investigation.[43-46] Optical analysis shows negligible light absorption in the EDL, allowing us to isolate its ability to increase the IQE of SubPc.

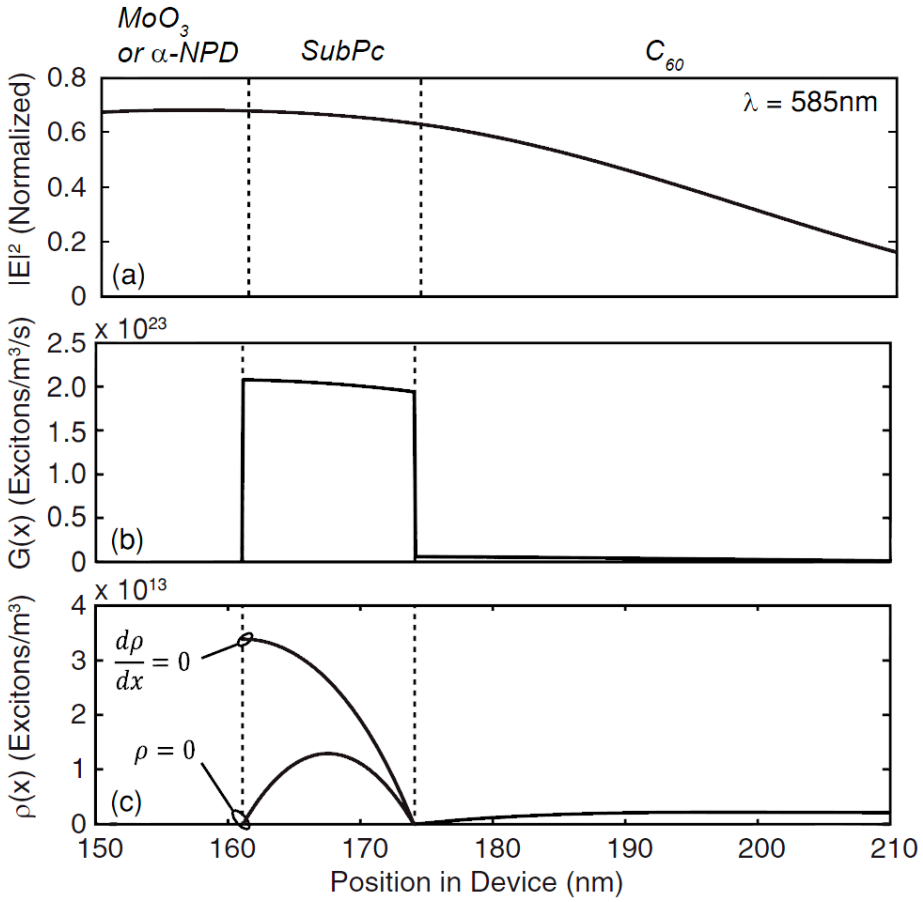

Figure 2.2 Modeled a) electric field, b) exciton generation, and c) exciton population density profiles within the OPV device used in this study. Boundary conditions (which only affect the exciton population density) at the SubPc/MoO_3 or SubPc/α-NPD interface are shown for both perfect exciton reflection ($d\rho/dx$ = 0) and 100% exciton quenching or dissociation (ρ = 0).

We first consider a physical model of an archetypal single heterojunction (SHJ) photovoltaic cell. Light is absorbed within the active donor and acceptor layers, generating excitons that can then diffuse isotropically. For the excitons to be converted into free charges and subsequently collected as current, they must diffuse to the heterojunction where they can undergo charge transfer. Exciton lifetime (τ) and diffusivity in the organic layers determine the average exciton diffusion length (L_D), which is typically on the order of 10 nm[2,47] – excitons generated further than L_D from a heterojunction are less likely to contribute to photocurrent. To model the internal exciton transport and EQE of our devices, we utilized the framework established by Pettersson et

al.,[10] calculating the electric field profiles and exciton generation profiles within the device as detailed in Section 1.7 (**Figure 2.2a,b**). The thick glass substrate was treated as optically incoherent.[48]

The Feng-Ghosh model is used to model the diffusion in the device, as discussed in 1.7.3. For each case, we assume 100% dissociation at the SubPc/C_{60} heterojunction, consistent with standard practice.[11] Because bathocuproine (BCP) is a large bandgap EBL, the C_{60}/BCP interface is treated as an exciton reflector ($d\rho/dx$ = 0 at the interface). The MoO_3/SubPc interface has previously been assumed to behave identically, under the assumption that MoO_3 also functions as an EBL.[28] Alternatively, we can consider either 100% quenching at the interface or 100% dissociation if an EDL is present, both of which impose a zero value for the population density.[11] In the presence of an EDL, exciton flux at the interface contributes to the total photocurrent of the device; in the absence of an EDL, and assuming quenching by the MoO_3, exciton flux at the interface is lost to recombination and does not contribute to photocurrent generation.

In the device containing an EDL, we assume that a second exciton dissociating junction is operating alongside the conventional donor/acceptor junction. To predict its EQE spectrum, we must make an assumption as to whether the two heterojunctions are operating as diodes connected in series or parallel. To date, heterojunctions in CHJs have been described in literature as individual diodes connected in series.[32,33] However, our results indicate that while the layers themselves are spatially positioned in series, they behave electrically as parallel photodiodes. Due to the cascading nature of the HOMO and LUMO levels, charges dissociated from either interface experience a barrier-free transit to the electrodes, regardless of their position within the structure (**Figure 2.1b**). Thus our modeling treats the photocurrents from each junction as additive (electrically in parallel), with the caveat that there is negligible recombination of non-

geminate carriers within the bulk of the central device layers (consistent with previous findings for cascade devices with SubPc used as an ambipolar interlayer).[33]

While our model focuses primarily on exciton and charge transport at short-circuit conditions ($V_a = 0$), it is important to note that current injection under bias in a CHJ device will not be identical to current injection in a SHJ device. Although photocurrent extraction remains unimpeded, the extra heterojunction contributes an additional barrier to current injection that increases the total series resistance of each HJ in the cascade device over that in its SHJ counterpart. Additionally, in the case of strongly unipolar materials, internal layers can also become transport limiting and exhibit space-charge limited (SCL) current behavior. This non-ideal case could result in a lower fill factor relative to the case of two trap-charge limited (TCL) heterojunctions in parallel, due to a large difference in the internal electric field at each heterojunction.

2.3 Experimental

2.3.1 Device Fabrication

Devices and samples were fabricated on commercially available ITO (Delta Technologies, 150 nm thick, R_s<15 Ω/□). Substrates were cleaned via heated (40^0C) sonication in detergent, water, acetone, trichloroethylene, and isopropanol, followed by boiling in isopropanol and 10 minutes of ultraviolet/ozone treatment to remove carbon residues and increase the anode work function. Device layers were deposited via vacuum thermal evaporation (VTE) using an Ångstrom AMOD deposition system. Fabrication was performed in a glovebox filled by an inert nitrogen environment (<1 ppm O_2 and H_2O), and samples were only exposed to atmosphere during testing. To minimize degradation in atmosphere during testing, devices were deposited on three

substrates simultaneously, so that one of each could be used for testing *J-V*, EQE, and absorption, respectively. Devices were kept in the glovebox until immediately before testing.

All organic materials were purchased from Luminescence Technology Corp. and deposited with no further purification. SubPc, BCP, and α-NPD (all >99%) and C_{60} (>99.5%) were all sublimed grade. MoO_3 (>99.99%) was purchased from Sigma Aldrich. Aluminum island electrodes were deposited through a shadow mask with a diameter of 1 mm, defining a nominal device area of 0.7865 mm^2, and contacted by a thin gold wire for testing.

2.3.2 Device Characterization

J-V data for all devices were recorded using an HP 4156B precision semiconductor parameter analyzer. The cells were illuminated with a Newport solar simulator (model# 91191-1000) calibrated to AM1.5 (100 mW/cm^2) using an NREL Si reference cell (Model PVM233 KG5). EQE was measured by directing a collimated beam of optically chopped light (185 Hz) from a halogen lamp coupled to a Newport 1/8m monochromator (5 nm FWHM) incident on the sample. The photocurrent was measured using a Stanford Research Systems SR530 Lock-in Amplifier and compared to the output from a calibrated Si photodiode. Total absorption of devices was measured using a Perkin Elmer Lambda 750 UV/Vis/NIR spectrometer. IQE was calculated by dividing EQE by experimental absorption at each wavelength. All device areas were measured using a Carl Zeiss Scope A.1 optical microscope and included explicitly in calculating J_{sc} and PCE.

2.3.3 Photoluminescence Measurements

Photoluminescent quantum yield measurements were taken with a Photon Technology International QuantaMaster spectrofluorometer. Luminescence between 550-800 nm was

measured in an integrating sphere under 530 nm (<10 nm FWHM) illumination from a Xenon lamp.

2.3.4 Morphology Measurements

All AFM measurements were performed on ITO-coated glass substrates using an Asylum Research Labs MFP-3D standalone system in tapping mode. XRD measurements were performed using a Rigaku Rotating Anode X-Ray Diffractometer in θ-2θ geometry with Cu-Kα radiation (wavelength of 1.5418 Å). Sample materials were deposited onto <100> Si. The SubPc control sample for XRD was annealed post-deposition for 15 minutes at 95°C to induce crystallization.

2.4 Results and Discussion

2.4.1 Archetypal SubPc/C_{60} Device

We first examine an archetypal SHJ SubPc/C_{60} device deposited on indium tin oxide (ITO), with MoO_3 implemented as a work function modifier (**Figure 2.3a**). The J_{sc} is slightly lower than the highest reported values for the same material system, likely due to variances among labs in material purity and instrument calibration.[39] Because of these variations, a common practice is to fit L_D of each active material to experimental EQE curves. Alternatively, L_D can be treated as a constant material property (when morphology is consistent), allowing EQE fitting to be accomplished by only modifying boundary conditions within the device. Using L_D values from literature[47,49-52] (**Table 2.1**), we note that EQE curves with the best fit to experiment suggest substantial exciton quenching at the MoO_3/SubPc interface. The value of L_D = 8.5 nm for SubPc deduced from our fits is consistent across all devices in this study and closely approximates SubPc diffusion lengths measured independently by Luhman *et al.* [47] and Lunt *et al.*[50] While

MoO_3 is typically used for its high work function and purported ability to block excitons, these results suggest that a more physically sound and consistent interpretation is that MoO_3 quenches excitons. Work by Xiao *et al*. also showed that MoO_3 quenches excitons in both tetraphenyldibenzoperiflanthene (DBP) and C_{70}, further corroborating this conclusion.[53]

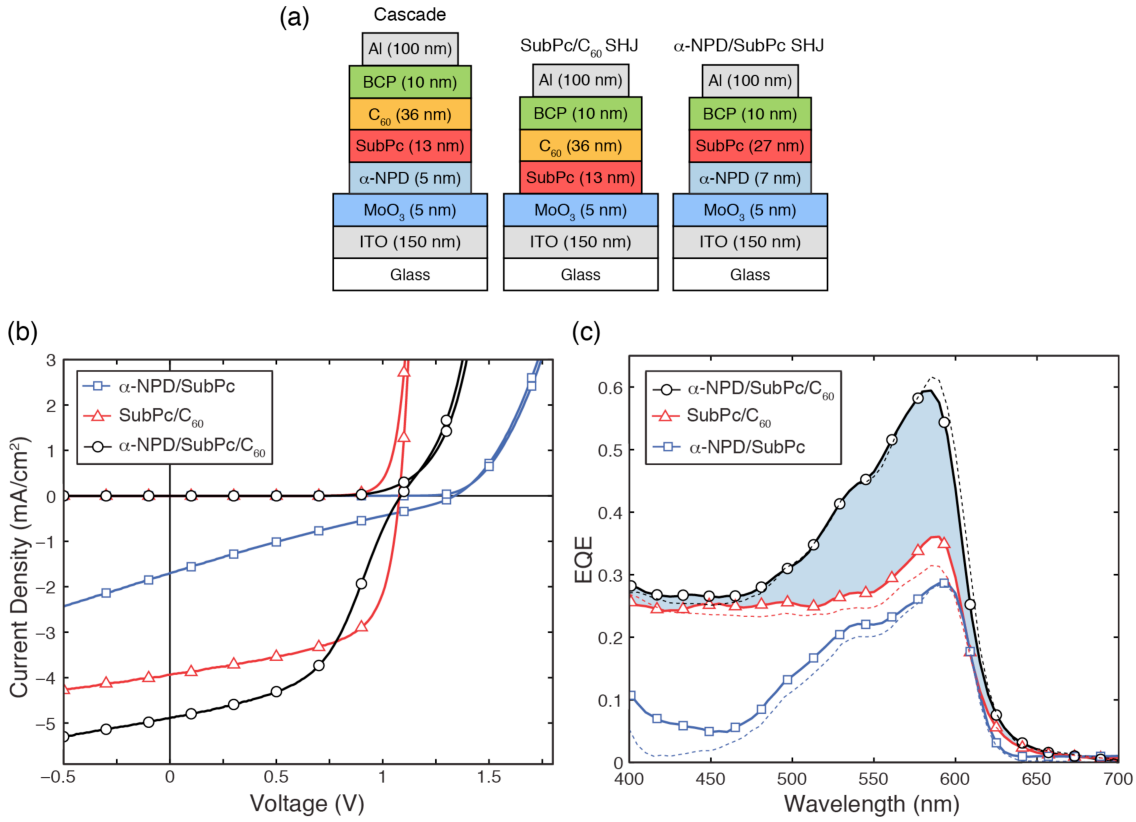

Figure 2.3 a) Device structures for α-NPD/SubPc/C_{60}, SubPc/C_{60}, and α-NPD/SubPc OPV cells. b) *J-V* data under 1-sun illumination for α-NPD/SubPc (squares), SubPc/C_{60} (triangles), and α-NPD/SubPc/C_{60} (circles) devices. c) For each device, experimental EQE data (solid lines) is compared to model (dashed lines).

Table 2.1 Literature and fitted values of exciton lifetimes and diffusion lengths for active materials used in this study.

Material	$L_{D,Ref.}$ (nm)	$L_{D,Fit}$ (nm)	$\tau_{,Ref.}$ (ns)	$\tau_{,Fit}$ (ns)
SubPc	7.7[27], 8.0[32]	8.5	<1[32]	0.3
C_{60}	11[6]	16	1.2[34]	1
α-NPD	5.1[32]	5	3.5[33]	5

2.4.2 α-NPD/SubPc as a Functional Heterojunction

To validate our hypothesis that α-NPD would enable exciton dissociation, we created a SHJ device with α-NPD acting as the ED and SubPc as the EA. SubPc has been previously shown to exhibit ambipolar behavior in devices[54] and has been successfully used as both a donor and acceptor layer within cascade geometries.[33] The α-NPD/SubPc SHJ device (**Figure 2.3a**) exhibits a J_{sc} of 1.72 mA/cm^2, indicating that it indeed enables exciton dissociation and photocurrent generation. The majority of the photocurrent in the device is due to contributions from the SubPc layer, as indicated by the modeled and experimental EQE curves in **Figure 2.3c**. Although the HOMO-LUMO gap of the heterojunction is nearly equivalent to that of SubPc/C_{60} (1.8 eV vs. 1.9 eV respectively), the device exhibits an unusually high open-circuit voltage (V_{oc}) of 1.34 V. This V_{oc} seems to indicate a lower binding energy of the polaron pair state, likely due to a different molecular separation distance between SubPc and α-NPD as compared to SubPc and C_{60}.[55]

While SubPc is capable of transporting electrons, devices tested in this study appear to be electron transport-limited. Due to a low electron mobility (compared to hole mobility) in SubPc,[56] the device exhibits SCL current behavior under forward bias, described by the Mott-Gurney Law.[57] Because both α-NPD and SubPc exhibit high hole mobilities,[58] the device experiences a large drop in shunt resistance (R_p) due to photoconductivity,[59] resulting in a FF of 23.5%. Minority carrier mobility can be especially sensitive to material impurities, and the low electron mobility in our SubPc may be due to differences in impurity concentration from that used by Beaumont *et al.* [54] (Impurities affecting electron conductivity do not necessarily influence exciton diffusion.) Improvements in the FF of this device may be accomplished either by choosing another donor material with higher electron mobility or by improving the electron

mobility of SubPc *via* purification, doping, or molecular ordering. (We note that when this junction is examined in the MoO_3/α-NPD/SubPc/C_{60} device, the transport limitation is partially mitigated by a more favorable electric field profile.)

2.4.3 Quantum Yield Measurements

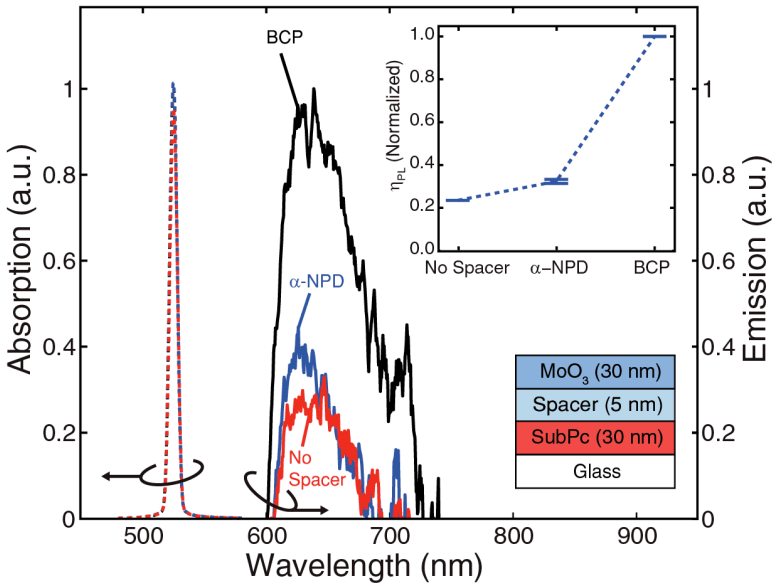

Figure 2.4 Experimentally determined absorption and emission spectra for SubPc/Spacer/MoO_3 stacks deposited on glass. Inset: normalized quantum yield measurements for each stack. Quantum yield was determined using no spacer as well as spacers of BCP and α-NPD.

The parasitic quenching behavior of the MoO_3/SubPc interface and the exciton dissociating ability of the α-NPD/SubPc interfaces were verified by performing photoluminescent quantum yield (η_{PL}) measurements on a multilayer stack composed of Glass/SubPc (30 nm)/Spacer (5 nm)/MoO_3 (30 nm). For spacers, we used α-NPD, BCP, and no spacer. As seen in **Figure 2.4**, light absorption was approximately equivalent for each multilayer stack. The position of the HOMO and LUMO energy levels in BCP relative to SubPc prevent charge transfer from SubPc into MoO_3, which is indicated by the highest PL signal from the stack with a BCP spacer. In contrast, the signal for the stack with an α-NPD spacer was nearly identical to that with no spacer. Since the LUMO level of the α-NPD prevents exciton transfer from the the SubPc layer

into the α-NPD layer, it is highly unlikely that excitons generated in the SubPc are making it to the MoO_3 interface to be quenched. Thus we conclude that charge transfer of SubPc excitons must be occuring at the α-NPD/SubPc interface, reducing the η_{PL} of the stack. From the α-NPD/SubPc device in **Figure 2.2**, it is apparent that charges transferred from SubPc to α-NPD can be collected as photocurrent. However, the stack with no spacer exhibited a similar η_{PL} to that of the stack containing the α-NPD spacer, indicating significant quenching of excitons at the SubPc/MoO_3 interface. This result further confirms the fit of modeled EQE to experiment, where 100% quenching is predicted at the SubPc/MoO_3 interface.

2.4.4 Thickness Dependence of the EDL Functionality

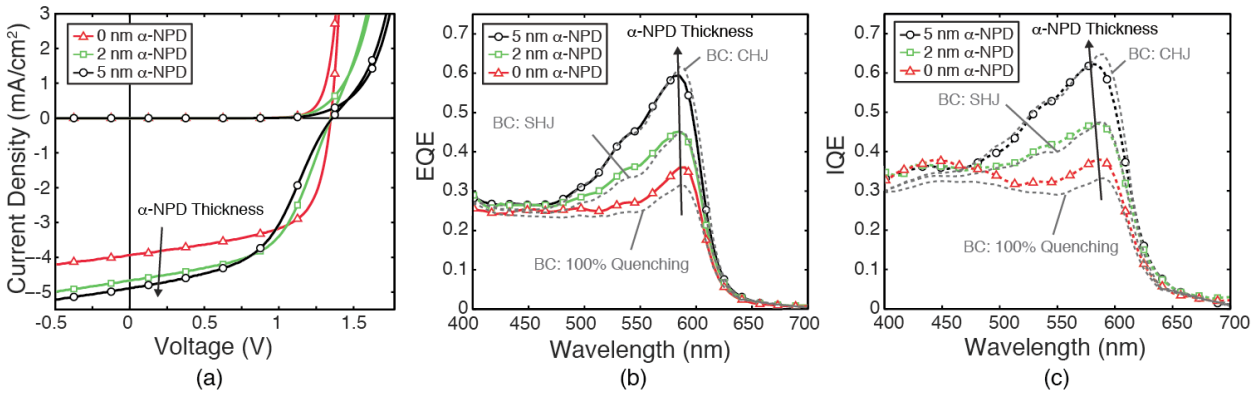

Figure 2.5 Experimentally determined a) *J-V*, b) EQE, and c) IQE data for Glass/ITO/MoO_3 (5 nm)/α-NPD (*x* nm)/SubPc (13 nm)/C_{60} (36 nm)/BCP (10 nm)/Al (100 nm). Three α-NPD thicknesses are shown: 0 nm (triangles), 2 nm (squares), and 5 nm (circles). Modeled EQE and IQE (dotted lines) are shown with three possible boundary conditions at the SubPc/MoO_3 or SubPc/α-NPD interface: 100% quenching, exciton reflection (SHJ), and 100% dissociation (CHJ).

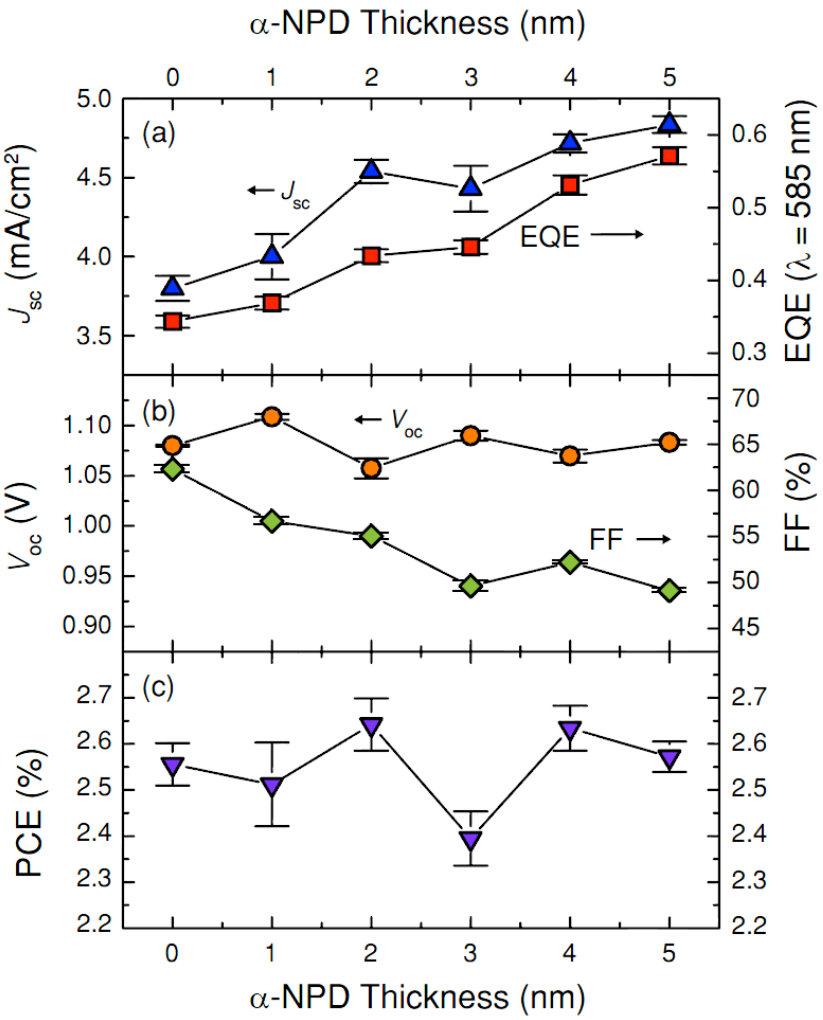

Figure 2.6 Dependence of a) J_{sc}, EQE at λ = 585nm, b) V_{oc}, FF, and c) PCE on α-NPD layer thickness for a device comprising Glass/ITO/MoO_3 (5 nm)/α-NPD (*x* nm)/SubPc (13 nm)/C_{60} (36 nm)/BCP (10 nm)/Al (100 nm). Error bars represent standard deviations calculated from a sample size of >8 devices.

From **Figure 2.3**, it is clear that the addition of the 5 nm α-NPD layer to the SubPc/C_{60} device substantially increases both EQE and J_{sc}. To further probe the transition from quenching to exciton dissociation in these structures, we studied CHJ devices while varying the α-NPD EDL thickness from 0-5 nm (thicknesses up to 10 nm are considered in Chapter 3, with no discernable differences in J_{sc} between 5 nm and 10 nm). Because there is minimal optical cavity confinement within the device and the α-NPD layer is located furthest from the reflective cathode, increasing the α-NPD thicknesses from 0-5 nm has a negligible effect on the optical field profile within the active layers. Therefore, all noticeable effects on device performance can be attributed to

interfacial properties at the SubPc/α-NPD junction. **Figure 2.5a-c** shows select *J-V* and spectroscopic characteristics of devices as the α-NPD thickness is increased, with each device demonstrating an EQE spectrum corresponding to modeled EQE for one of three boundary conditions at the SubPc/α-NPD or SubPc/MoO_3 interface (quenching, exciton reflection, and exciton dissociation). With increasing α-NPD thickness, there is a notable increase in photocurrent as well as a concomitant decrease in the FF (**Figure 2.6a-b**). Cnops *et al*. see a similar decrease in FF for thick SubPc layers used in cascade devices, also attributing the drop to low charge carrier mobilities in SubPc.[33] The EQE contribution from the SubPc layer (peak at λ = 585 nm) increases with α-NPD thickness, as seen in **Figure 2.6a**. We observe a reasonable fit for the quenching boundary condition at the SubPc/MoO_3 interface (**Figure 2.5b**). We note that while devices with 2 nm of α-NPD do approximate the modeled EQE with exciton reflection as the boundary condition at the SubPc/α-NPD interface, this would require a sudden and temporary change in the fundamental properties of the materials involved. Instead, it is more likely that at 2 nm, coverage of the electrode by the EDL is incomplete, resulting in only partial exciton dissociation at the α-NPD, offset by parasitic quenching at the MoO_3. The experimental EQE for the 5 nm α-NPD device is much higher than the predicted EQE for a SHJ device, corroborating the functionality of α-NPD as an EDL. If the CHJ boundary conditions are included in the model, the fit is nearly perfect for the device with 5 nm α-NPD. Experimental and modeled IQE plots (**Figure 2.5c**) are well matched, further confirming that the observed increase in J_{sc} is not due to changes in the optical field profiles or additional absorption from α-NPD, but rather from changes in boundary conditions at the SubPc/MoO_3 or SubPc/α-NPD interfaces.

We see a stable V_{oc} in all devices versus α-NPD thickness (**Figure 2.6b**), in agreement with the assumption that both heterojunctions are operating in parallel, limiting the V_{oc} to that of

the lowest-voltage (SubPc/C_{60}) heterojunction. There is a steady increase in both the J_{sc} and EQE at λ = 585 nm versus α-NPD thickness, consistent with the creation of a conformal layer for exciton dissociation. Atomic force microscopy (AFM) images of 5 nm MoO_3 on ITO show a root mean squared roughness (R_{rms}) of 3.52 nm (**Figure 2.7**). Therefore, we expect that as the α-NPD layer thickness is increased from 0-5 nm, the substrate coverage becomes more complete, resulting in a monotonic increase in photocurrent.

As the thickness of the α-NPD layer is increased, we note that while the average J_{sc} increases at a similar rate to that of the EQE at 585 nm, there is a small "jump" in the J_{sc} that occurs at 2 nm α-NPD. For the device with 2 nm α-NPD, the V_{oc} also decreases. Because there is no visible trend in the V_{oc} of each device from 0-5 nm α-NPD, and because *J-V* and EQE tests are performed on different devices and substrates, we assume these variations to be due to small variations in material purity or work function of the ITO substrate, both of which could influence V_{oc} and J_{sc}.

Table 2.2 Champion solar cell performance data for the structure: Glass/ITO/MoO_3 (5nm)/α-NPD (*x* nm)/SubPc (13nm)/C_{60} (36nm)/BCP (10nm)/Al (100nm) under simulated 1-sun, AM1.5G illumination.

α-NPD Thickness (nm)	J_{sc} (mA/cm^2)	V_{oc} (V)	FF (%)	PCE (%)
0	3.94	1.08	61.5	2.61
1	4.20	1.10	55.9	2.75
2	4.67	1.08	54.4	2.74
3	4.77	1.08	49.0	2.53
4	4.74	1.08	52.3	2.67
5	4.90	1.09	49.2	2.61
ITO/MoO_3 (5)/α-NPD (7)/ SubPc (27)/BCP (10)/Al (100)	1.72	1.34	23.5	0.54

2.5 Morphology

Atomic force micrographs show no discernible change in roughness of the SubPc layer with (**Figure 2.7c**) and without (**Figure 2.7d**) a 5 nm α-NPD spacer layer added. We see little change in the grain size or roughness of the SubPc layer (**Figure 2.7e**) deposited on different surfaces under our experimental conditions. Additionally, XRD shows no sign of induced crystallinity in SubPc, so the increase in EQE cannot be explained by an increase in L_D due to templating in the SubPc layer.

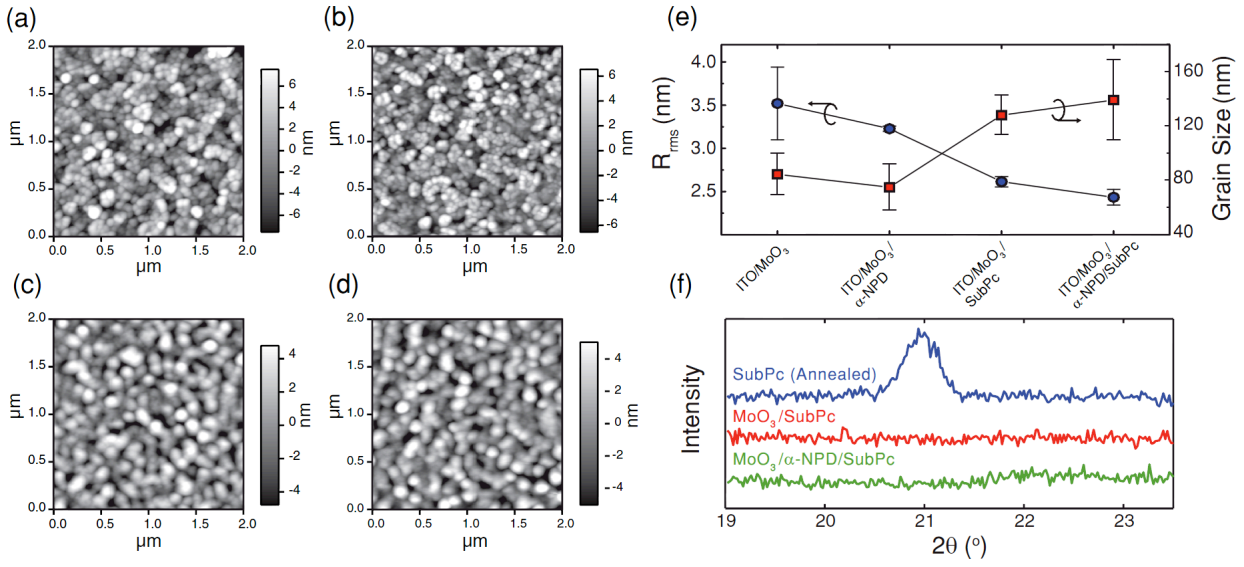

Figure 2.7 AFM images of a) ITO/MoO_3 (5 nm), b) ITO/MoO_3 (5 nm)/α-NPD (5 nm), c) ITO/MoO_3 (5 nm)/SubPc (13 nm), and d) ITO/MoO_3 (5 nm)/α-NPD (5 nm)/SubPc (13 nm). e) Grain size and R_{rms} values for each sample, and (f) XRD scans of MoO_3 (5nm)/SubPc (13nm) and MoO_3 (5 nm)/α-NPD (5 nm)/SubPc (13 nm), as well as a crystalline control sample of 13 nm SubPc annealed for 15 min at 95 ºC.

2.6 Conclusions

In summary, we have investigated the concept of an optically transparent exciton dissociation layer that boosts the internal quantum efficiency of an electron donor material in an organic heterojunction solar cell by simultaneously mitigating quenching and bulk recombination. We utilized α-NPD as the anode EDL in an archetypal SubPc/C_{60} device and presented a rigorous model for describing exciton transport within cascade heterojunction OPV architectures. By introducing the EDL, an additional interface for exciton dissociation was created, resulting in a 66% increase in IQE and EQE of the SubPc layer and a 27% increase in photocurrent of the device. Because the SHJ α-NPD/SubPc device exhibits a high V_{oc} (1.34 V), the α-NPD/SubPc/C_{60} device is able to maintain the 1.1 V open-circuit voltage of the SubPc/C_{60} system. The observed decrease in FF (an inherent problem for CHJ devices with a thick SubPc

interlayer) will need to be addressed in future work, likely by choosing a more ambipolar donor material or by improving the electron mobility of SubPc via doping and/or molecular ordering.

The EDL in this study is defined such that it improves the overall EQE of the OPV device, but it does so specifically by reducing diffusion losses in the adjacent active layer (i.e. absorption changes in the device are negligible). This makes the EDL-containing device different from other cascade geometry devices where multiple photon-harvesting layers are used – the EQE of a given device might be improved by adding a third absorbing layer in a cascade geometry, but the IQE of the outermost absorbing layers will still be lower than if a transparent EDL were inserted between the electrode and outermost active layer. Furthermore, the EDL concept is not limited to the α-NPD/SubPc/C_{60} system, nor is it limited to the anode side of the device – adding an EDL to any planar OPV cell should substantially increase its IQE by preventing quenching at the electrode and reducing bulk recombination. Because exciton transport is a fundamental bottleneck in all excitonic PV devices, the incorporation of EDLs promises to be an alternative approach to bulk heterojunctions and EBLs by circumventing the trade-off between exciton diffusion and optical absorption efficiencies in OPV active layers.

Chapter 3

Design Rules for High Fill Factor in Cascade Heterojunction OPVs

In Chapter 2, we discussed the promise for cascade heterojunction organic solar cells as an emerging alternative to conventional bulk heterojunctions and series-connected tandems due to their significant promise for high internal quantum efficiency and broad spectral coverage. However, CHJ devices demonstrated in that chapter and elsewhere in literature had also generally exhibited poor fill factor, resulting in minimal enhancements (or even decreases) in power conversion efficiency when compared with single heterojunction cells. In this chapter, the major variables controlling the CHJ maximum power point and FF are determined. By matching the maximum power point voltage (V_{MPP}) of the constituent parallel-connected heterojunctions (subjunctions) and minimizing the injection barriers intrinsic to CHJs, a high FF is maintained and the PCE is improved by 46%. Devices with a transparent exciton dissociation layer (EDL)/interlayer/acceptor structure are used, such that each CHJ has an absorption efficiency identical to its interlayer/acceptor SHJ counterpart. Using these results, a clear map of performance as a function of material parameters is developed, providing straightforward design rules to guide future molecular engineering and layer architectures for cascade heterojunction organic photovoltaic devices.

3.1 Introduction

As introduced in Chapter 2, a new approach to circumventing the absorption/diffusion tradeoff in OPVs involves cascade heterojunction devices.[32-35,60,61] In CHJs, the HOMO and LUMO levels of three or more active layers are progressively offset to create multiple energetically cascading heterojunctions within the device. In the simplest case, a planar CHJ employs a three-layer architecture consisting of a donor/interlayer/acceptor stack: the interlayer is sandwiched between two heterojunctions, enabling exciton dissociation on both the donor and acceptor sides, thereby reducing the distance excitons must travel before dissociating. This reduced diffusion distance can substantially increase the IQE of the interlayer, resulting in a higher EQE and overall device J_{sc}. Compared to BHJs, planar devices can offer nearly 100% charge collection efficiency, more straightforward optimization of optical absorption, and more refined control over individual layer morphologies.[62] Due to the nature of CHJ device design, it is also possible to broaden spectral coverage by using three (or more) active layers with absorption peaks in non-overlapping regions of the spectrum, providing an alternative or complementary approach to series tandem configurations. However, efficient charge collection in CHJs does not automatically translate to a good fill factor.[33,61] Indeed, in Chapter 2 we demonstrated a 66% increase in the IQE and EQE of boron subphthalocyanine chloride (SubPc) by introducing a large bandgap, transparent exciton dissociation layer between SubPc and the anode in a planar SHJ SubPc/C_{60} device.[61] Although the J_{sc} improved significantly, the overall PCE exhibited only a minimal increase due to a concomitant decrease in FF, leaving open questions as to the fundamental limitations of the CHJ solar cell architecture.

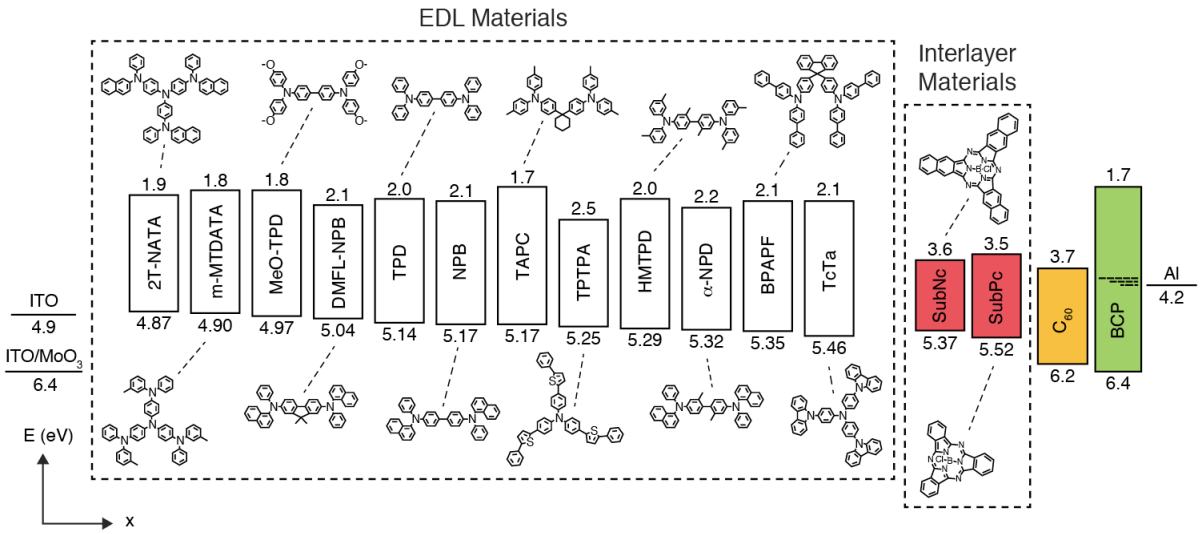

Figure 3.1 Schematic of energy levels and molecular structures for all materials used in this study. HOMO levels of all EDL and interlayer materials were measured using cylic voltammetry and bandgap energies were estimated from the absorption onset. The HOMO level of C_{60} was taken from literature and it's bandgap energy was estimated from the absorption onset.[46] Energy levels for BCP and the electrodes were taken from literature.[43,44] The prospective EDL materials were chosen such that their HOMO levels ranged semi-continously from ~4.9 eV to ~5.5 eV. The two interlayers were chosen based on their differences in V_{MPP} when in SHJ configurations with C_{60}.

In this chapter, we perform a systematic study of the EDL/interlayer/acceptor system to probe the underlying mechanisms that cause low FFs in CHJ devices. We employ 12 exciton dissociation layers, coupled with SubPc or boron subnaphthalocyanine chloride (SubNc) as interlayers and C_{60} as the acceptor. As a reminder, the FF is a simple way of relating J_{sc} and V_{oc} to the maximum power point (MPP):

$$\mathrm{FF} = \frac{V_{\mathrm{MPP}} \cdot J_{\mathrm{MPP}}}{V_{\mathrm{oc}} \cdot J_{\mathrm{sc}}} \tag{3.1}$$

where V_{MPP} and J_{MPP} are the voltage and current at the MPP, respectively. However, while FF can be a useful metric for describing device performance, it can be imprecise or misleading if both J_{sc} and V_{oc} vary between the devices under consideration. We instead focus on the MPP for comparisons between devices with the understanding that if V_{MPP} and J_{MPP} are maximized, then FF will also be maximized. For CHJs, we show that the V_{MPP} is limited by two major factors, both of which can lead to the onset of s-kink behavior in the current-voltage (J-V) characteristics

of the devices. First, we demonstrate that the two active heterojunctions (which we term "subjunctions") in the cascade operate electrically in parallel,[61] with the maximum V_{MPP} of the CHJ limited by the lowest V_{MPP} of the two subjunctions. Second, we show that the V_{MPP} of a CHJ is further limited by the energy offset between the HOMO levels (ΔE_{HOMO}) of the hole transporting donor layer and interlayer. As ΔE_{HOMO} increases, the voltage at the maximum power point (V_{MPP}) decreases, leading to a lower FF and PCE. We attribute this parasitic effect to the introduction of an energetic charge injection barrier, which results in a space charge build up within the device and a corresponding decrease in the built-in field.[63,64] Impressively, for optimized devices we observe an increase in the peak IQE of the SubPc and SubNc layers from 38% and 66% to 84% and 99%, respectively, over reference SHJ devices with no EDL. Furthermore, by matching the V_{MPP} of each subjunction and choosing an EDL with $\Delta E_{HOMO} \leq 0.2$ eV, we minimize any losses in V_{MPP} (and FF) and demonstrate a 46% enhancement in PCE for a SubNc CHJ over its SHJ reference device.

3.2 Experiment

3.2.1 Energy Levels

HOMO levels for all interlayer and EDL materials were measured *via* cyclic voltammetry. Each material was dropcast from chloroform onto a 3 mm diameter glassy carbon working electrode. Using 0.1 M tetrabutylammonium hexafluorophosphate in acetonitrile as an electrolyte, samples were scanned at a rate of 0.1 V s^{-1} relative to an $Ag/AgNO_3$ reference electrode with a Pt wire counter electrode. Scans were normalized to the onset of oxidation of ferrocene, taken as -4.8 eV. The bandgap was estimated from the onset of absorption, and the LUMO level was calculated by adding the bandgap to the HOMO level.

3.2.2 Device Fabrication

Devices were deposited on commercially available ITO (Delta Technologies, 150 nm thick, R_s<15 Ω/□). Substrates were cleaned *via* heated (40°C) sonication in detergent, water, acetone, trichloroethylene, and isopropanol, followed by boiling in isopropanol and 10 minutes of ultraviolet/ozone treatment to remove carbon residues and increase the anode work function. Device layers were deposited *via* vacuum thermal evaporation (VTE) using an Ångstrom AMOD deposition chamber. Fabrication and *J-V* testing was performed in a glovebox filled with an inert nitrogen environment (<1 ppm O_2 and H_2O). To minimize degradation in atmosphere during testing, devices were simultaneously deposited on three substrates, so that one of each could be used for testing *J-V*, EQE, and absorption. Only samples for EQE and absorption measurements were exposed to atmosphere. For EQE and *J-V* testing, aluminum island electrodes were deposited through a shadow mask with a diameter of 1 mm. All device areas were measured using a Carl Zeiss Scope A.1 optical microscope and included explicitly in calculating J_{sc}, EQE, IQE, and PCE. All organic materials were purchased from Luminescence Technology Corp. and deposited with no further purification. SubPc, SubNc, BCP, and all EDL materials (>99%) and C_{60} (>99.5%) were sublimed grade. MoO_3 (>99.99%) was purchased from Sigma Aldrich and Al (99.9%) was purchased from Alfa Aesar.

3.2.3 Device Characterization

Device *J-V* data were recorded using an HP 4156B precision semiconductor parameter analyzer. The cells were illuminated with a Newport solar simulator (model# 91191-1000) calibrated to AM1.5 (100 mW/cm^2) using an NREL Si reference cell (Model PVM233 KG5). EQE was measured by directing a collimated beam of optically chopped light (185 Hz) from a halogen lamp coupled to a Newport 1/8m monochromator (5 nm FWHM) incident on the sample. The

photocurrent was measured using a Stanford Research Systems SR530 Lock-in Amplifier and compared to the output from a calibrated Si photodiode. The spectrum of the solar simulator was measured with an Ocean Optics USB2000 spectrometer and convoluted with the experimental EQE to determine the spectral mismatch factor for each device with respect to the AM1.5G spectrum (All mismatch factors were determined to be 1 ± 0.05).[65] Absorption in the completed devices was measured in reflection mode using a Perkin Elmer Lambda 750 UV/Vis/NIR spectrometer at an incidence angle of 7.5°. The absorption spectrum for each device was then compared to a transfer matrix optical model to confirm device layer thicknesses. IQE was calculated by dividing experimental EQE by modeled active layer absorption at each wavelength at normal incidence.

3.2.4 Optical Properties of Materials

The thicknesses and optical properties of all materials were measured using a variable angle spectroscopic ellipsometer (M-2000, J.A. Woollam Co.). Measurements were performed in both transmission mode and reflection mode at angles of 55°, 65°, and 75° for each of the materials on a glass substrate. The film thickness and surface roughness were first determined by fitting the acquired ellipsometric angles Δ and Ψ to a Cauchy model over the wavelength range in which the material is transparent. The refractive index values were then determined by fixing the film thickness as well as surface roughness and parameterizing the material as a B-Spline layer. The wavelength range was gradually increased, in increments of 0.1 eV, until it included the entire measured spectral range. The resultant values were then verified to be Kramers-Kronig (KK) consistent.

3.2.5 Mobility Measurements

For hole mobility measurements, samples were fabricated with the structure ITO/PEIE(10 nm)/EDL(800 nm)/Au(80 nm). PEIE (0.4 wt% in methoxyethanol) was spin-coated at 5000 rpm for 60 s and subsequently baked at 100°C for 10 minutes prior to VTE deposition of the EDL at 1 Å/s. Circular gold contacts were deposited at 1 Å/s and defined by a shadow mask. Time-of-flight measurements were performed using a nitrogen laser (VSL337 from Newport) with a wavelength of λ = 337.1 nm, an intensity per pulse of ~120 μJ, and a pulse duration less than 4 ns, for photo-generation of charge carriers in the films (illuminated through the ITO substrate). A Keithley 2400 SourceMeter was used to apply constant voltage over devices, with the ITO cathode under positive bias to prevent charge injection. The current transients were then amplified using a FEMTO DLPCA-200 low noise current amplifier and recorded with a Tektronix TDS3052C digital oscilloscope.

3.3 Results and Discussion

3.3.1 Active Layer Energy Levels and Device Architectures

Twelve different triphenylamine derivatives were used in this study as EDLs, selected based on their high hole mobilities, transparency in the visible spectrum, and HOMO levels varying from ~4.9 eV to ~5.5 eV. **Figure 3.1** depicts a schematic energy level diagram and the molecular structure for all materials used.[43,44,46,66] In **Figure 3.2**, we show the absorption coefficients for each material, with only the interlayers and C_{60} acceptor having absorption peaks in the visible spectrum. The two interlayer materials were chosen primarily due to their different characteristic V_{MPP} when paired with C_{60} in a SHJ configuration. As demonstrated below, the EDL/interlayer V_{MPP} often limits the CHJ V_{MPP}, so choosing a reference SHJ with a lower V_{MPP} can help match V_{MPP} between the EDL/interlayer and interlayer/C_{60} subjunctions.

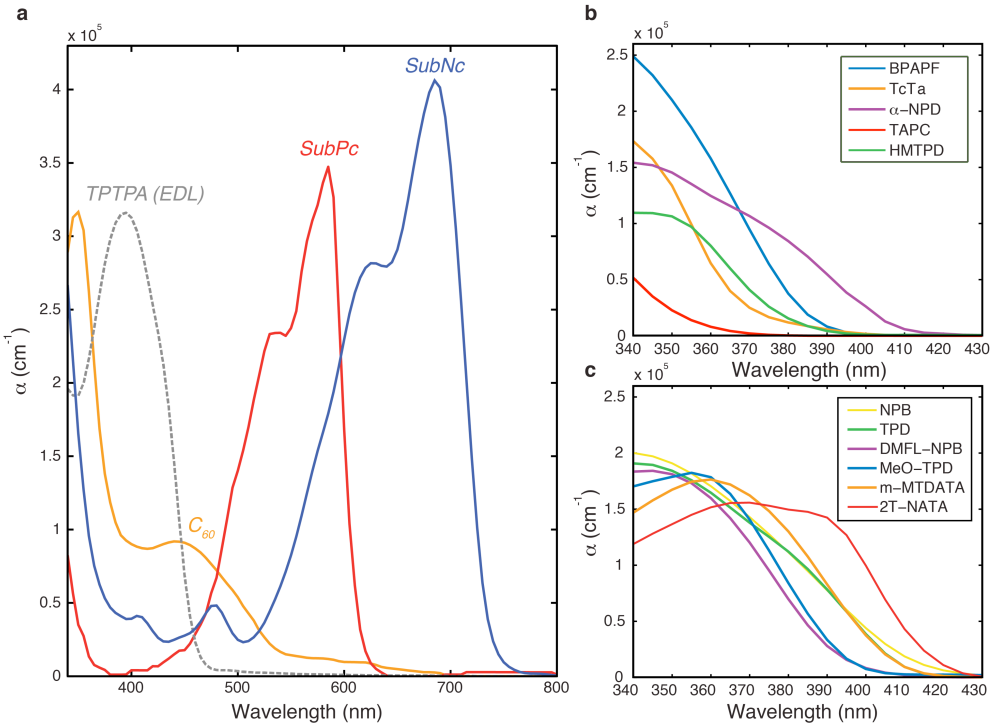

Figure 3.2 Absorption coefficients of active materials used in this study, as determined by variable angle spectroscopic ellipsometry. Spectra are shown for a) absorbing energy harvesting layers SubPc, SubNc (at normal incidence), C_{60}, and TPTPA EDL; b) EDLs BPAPF, TcTa, α-NPD, TAPC, and HMTPD; and c) EDLs NPB, TPD, DMFL-NPB, MeO-TPD, m-MTDATA, and 2T-NATA.

MoO_3 was used as an anode buffer layer in all SHJ and CHJ devices employing SubPc as an active layer. While we demonstrated in Chapter 2 that MoO_3 quenches excitons in SubPc and other common OPV materials,[53,61] its high work function is helpful for sustaining the ~1.1 V open-circuit voltage of SubPc/C_{60} devices.[67] Moreover, because it is transparent, MoO_3 causes virtually no changes to the optical field profiles within the device, unlike other commonly used buffer layers such as poly(ethylenedioxythiophene):poly(styrenesulfonate) which absorb in the visible portion of the spectrum.[68] Because MoO_3 is not required for the lower V_{oc} (~0.8 V) of SubNc/C_{60} devices, it was not used in SubNc/C_{60} SHJ or EDL/SubNc/C_{60} CHJ devices. MoO_3 was used for all EDL/SubNc SHJ devices to ensure the built-in field did not limit V_{oc}. As will be seen below, all trends in device performance were independent of the anode.

3.3.2 Electrical Operation of CHJ Devices

To understand CHJ device operation, we must consider photocurrent generation under short-circuit conditions (determined by EQE) as well as the V_{MPP} and FF limitations of the device under forward bias. In Chapter 2, we showed that during operation at zero applied bias (**Figure 3.3c**), both subjunctions in a CHJ device act as current sources operating electrically in parallel, with a barrier-free extraction of charge carriers upon exciton dissociation.[61]

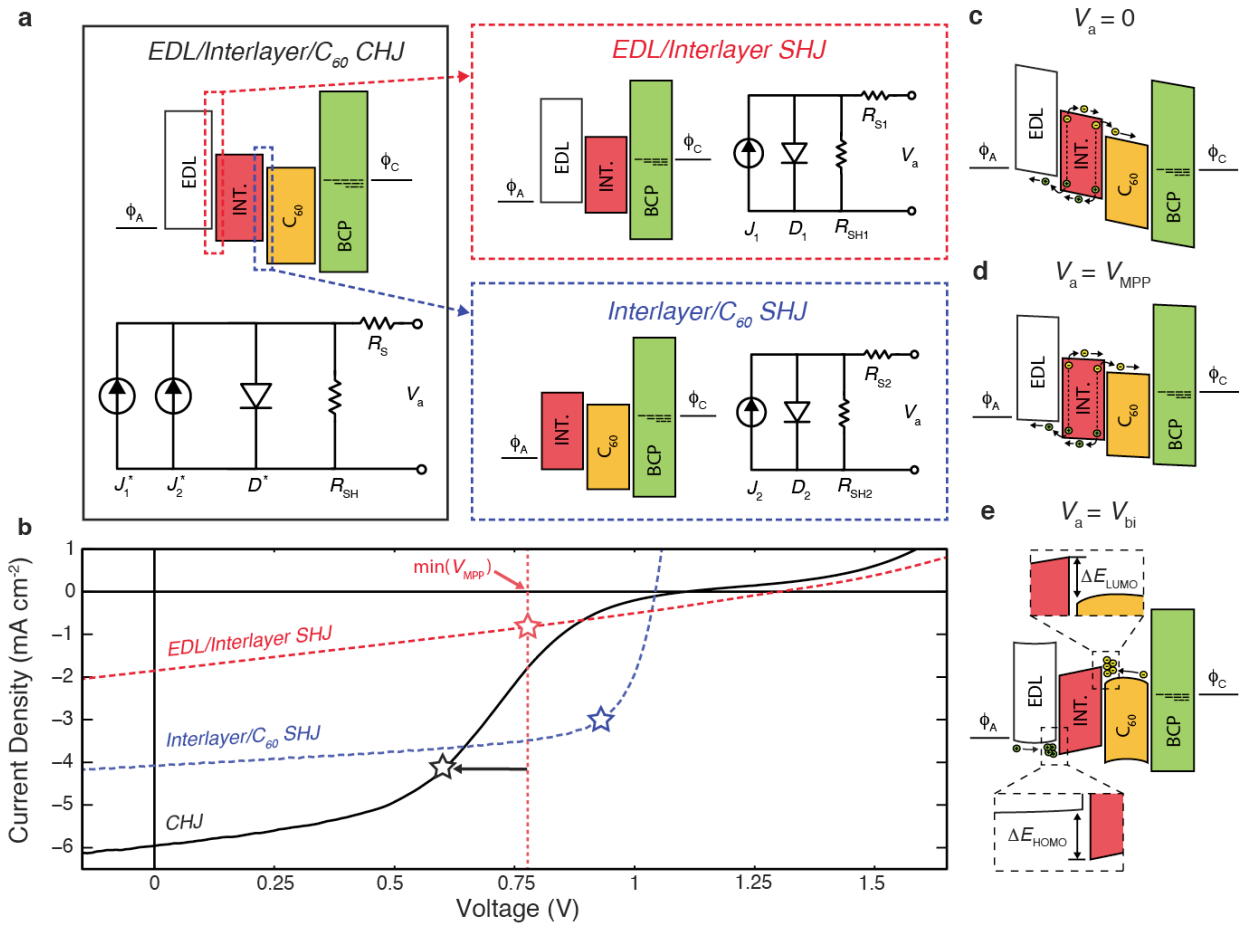

Figure 3.3 a) Schematic energy level and circuit diagrams for CHJ devices. The characteristic performance of each subjunction can be estimated by considering the *J-V* curves of corresponding SHJ devices. b) Characteristic experimental *J-V* curves of an EDL/interlayer SHJ, an interlayer/C_{60} SHJ, and an EDL/interlayer/C_{60} CHJ. The maximum power point for each device is marked by a star. From the two SHJs, it is clear the V_{MPP} of the EDL/interlayer will limit the maximum V_{MPP} of the CHJ device. Schematic band diagrams of c) exciton dissociation in a CHJ at short-circuit conditions (V_a = 0) d) exciton dissociation in a CHJ at V_{MPP}, where flat-band conditions have not been met. e) field inversion at both subjunctions in a CHJ due to the introduced hole-injection barrier with energy ΔE_{HOMO}.

By treating the subjunctions as acting electrically in parallel,[61] we can at the very least consider the qualitative *J-V* characteristics of CHJ devices under forward bias. In series-connected tandem structures, the J_{MPP} of the complete device will be limited by the lowest J_{MPP} of its two (or more) subcells.[19] Analogously, we could make an assumption that the V_{MPP} of a CHJ device will be limited by the lowest V_{MPP} of its constituent subjunctions. Due to CHJ device geometry, it is difficult to measure the V_{MPP} of each subjunction *in situ*. However, it is possible to estimate the V_{MPP} of each subjunction by measuring the *J-V* characteristics of each subjunction in separate

SHJ configurations. These concepts are illustrated in **Figure 3.3a**, where equivalent circuit diagrams are provided for each SHJ device and the CHJ device comprised of the two corresponding subjunctions. Experimental *J-V* curves for an EDL/interlayer/acceptor (TAPC/SubPc/C_{60}) system are shown in **Figure 3.3b**. A star shape marks the maximum power point for each device. From this plot, if our assumption holds that the CHJ V_{MPP} is limited by the lowest of either subjunction, then we can see that the V_{MPP} of the EDL/interlayer subjunction will limit the V_{MPP} of the CHJ device. In all experimental results, as discussed further below, the V_{MPP} of the CHJ is less than or equal to the lowest V_{MPP} of the two operating subjunctions.

To minimize losses in CHJ devices, the V_{MPP} values of the subjunctions must be closely matched. Previous studies have shown that the most important factors in determining the V_{oc} of SHJ devices are the energy of the HOMO-LUMO gap (ΔE_{HL}) and the polaron pair binding energy ($E_{B,PP}$) between the donor and acceptor layers. In the ideal case where FF = 100%, V_{MPP} would be limited by the maximum V_{oc} of the SHJ, as determined by:

$$V_{oc,\max} = \frac{\Delta E_{HL}}{q} - E_{B,PP} \tag{3.2}$$

where q is the electron charge.[69] In **Figure 3.4a**, we plot V_{oc} versus ΔE_{HL} for all EDL/interlayer SHJ devices fabricated in this study. As expected, V_{oc} does increase with larger ΔE_{HL}, but $E_{B,PP}$ also appears to increase as ΔE_{HL} approaches the interlayer bandgap energy (i.e. $\Delta E_{HOMO} \approx 0$), especially in the case of the EDL/SubNc SHJ devices. This is consistent with experimental findings by Zhang *et al.*,[70] attributable to a linear dependence of the polaron pair separation distance (a_0) on ΔE_{HOMO}.[23] **Figure 3.4b** plots simulated V_{MPP} values versus $E_{B,PP}$ for a standard SubPc/C_{60} SHJ, with V_{MPP} values taken from photocurrent curves simulated using the Onsager-Braun model, as detailed in Section 1.9 and with more detail in Section 3.3.8.[21,71] **Figure 3.4b**

shows that modeled V_{MPP} scales linearly with $E_{B,PP}$, with a 0.1 eV change in $E_{B,PP}$ causing a 45% drop in V_{MPP}. Thus we conclude that ΔE_{HL} and $E_{B,PP}$ (or a_0) are critical in matching the V_{MPP} of each subjunction in the CHJ.

3.3.3 Effect of ΔE_{HOMO} on CHJ V_{MPP}

As demonstrated in **Figure 3.3b**, the V_{MPP} of a CHJ can be lower than the V_{MPP} of either subjunction. To elucidate any other possible loss mechanisms, we investigated the effects of energy level alignment on CHJ V_{MPP}. It has been well established that injection barriers can lead to s-kink *J-V* behavior in OPVs, either due to non-ohmic contact at the electrode/donor interface[72-74] or injection bottlenecks between the *p* and *i* layers in *p-i-n* type OPV cells.[63,75] Because cascading energy levels are required for creating multiple heterojunctions, CHJs inherently contain more injection barriers than SHJs. In CHJs, injected holes and electrons could in principle recombine at either the EDL/interlayer heterojunction or the interlayer/acceptor heterojunction. In practice, however, asymmetric injection barriers and carrier mobilities will force recombination to occur at one of the subjunctions, which will in turn dictate the overall diode behavior of the CHJ.[40,55,69,76] For devices in this study, and the majority of CHJs shown previously in literature, phthalocyanines have been used as the interlayer, resulting in a large mismatch between interlayer hole (μ_h) and electron (μ_e) mobilities. Because $\mu_h > \mu_e$ for most phthalocyanines, recombination of injected charges will preferentially occur at the interlayer/acceptor interface. Recombination at that interface is favored even more if the electron injection barrier from the acceptor into the interlayer (ΔE_{LUMO}) exceeds the hole injection barrier from the EDL into the interlayer (ΔE_{HOMO}), as is the case for devices in this study with $\Delta E_{HOMO} < \sim 0.2$ eV (**Figure 3.3e**).

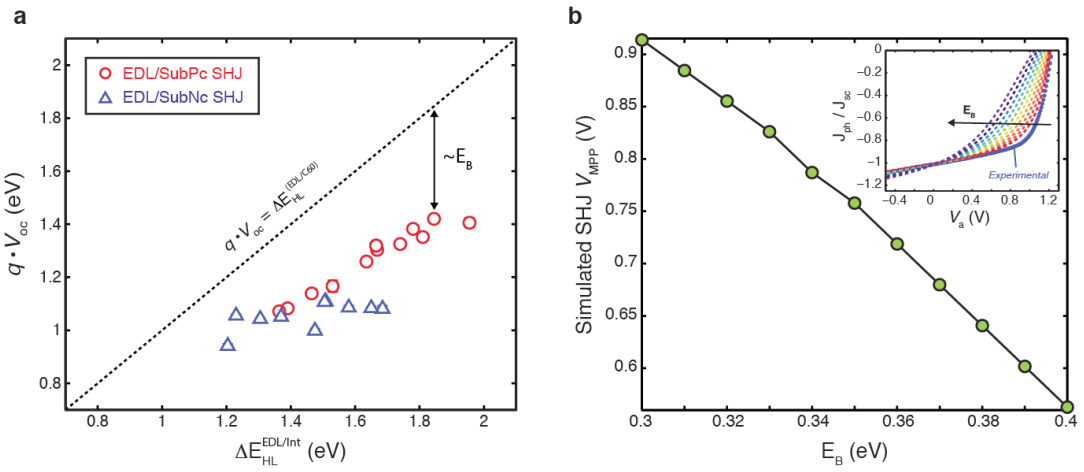

Figure 3.4 a) V_{oc} of every SHJ device in this study versus ΔE_{HL}. EDL/SubPc and EDL/SubNc SHJs are represented by open red dots and open blue triangles, respectively. b) Simulated V_{MPP} for a SubPc/C_{60} SHJ as a function of polaron pair binding energy, $E_{B,PP}$. *Inset:* Normalized photocurrent curves versus applied bias, for varying $E_{B,PP}$. Simulated photocurrent and V_{MPP} values were calculated using an Onsager-Braun model.

If recombination occurs at the interlayer/acceptor interface, we must then consider the effect of the HOMO level offset, ΔE_{HOMO}, introduced by inserting the EDL layer. While this offset is necessary for enabling dissociation at the EDL/interlayer interface and creating a second heterojunction, it also introduces an additional hole injection barrier that can lead to a buildup of charge in the device and a subsequent decrease in the built-in field.[64] At zero bias (**Figure 3.3c**), Fermi level alignment in all layers provides band bending that is beneficial to dissociating excitons at each heterojunction; as such, the photocurrent contributions from each subjunction are perfectly additive. As V_a increases ($0 < V_a < V_{oc}$), the polaron pair dissociation efficiency (η_{PPd}) decreases monotonically with the internal field until flat band conditions are reached. The maximum power point will occur at $V_a = V_{MPP}$, before flat band conditions (**Figure 3.3d**). Typically the field inside the active layers is assumed to be nearly constant below V_{oc}, although this is not necessarily the case in CHJs. Tress *et al.* employed a system using multiple hole transport layers and a transparent interlayer (called a donor layer in the study, as the only photocurrent-producing heterojunction was located at the interlayer/acceptor interface). Using a recursive transport model, ΔE_{HOMO} was shown to cause field inversion at the heterojunction

(band bending in opposition to exciton dissociation), causing a sharp drop in η_{PPd}, shutting off photocurrent production before V_{oc} and causing s-kink behavior in the *J-V* curve (**Figure 3.3e**). However, in that study, both the HTL and "donor" layers were transparent, meaning that all photocurrent generation came from absorption in the acceptor (C_{60}) layer. In this study, we employ CHJ devices with photocurrent generation occurring at *both* subjunctions, but expect a similar behavior to occur. To verify, we now experimentally determine the dependence of CHJ V_{MPP} on ΔE_{HOMO}.

In **Figure 3.5,** we show how ΔE_{HOMO} can affect *J-V* performance by varying the material used for the 5 nm transparent EDL. **Figure 3.5a-d** and **Figure 3.5e-h** show *J-V* curves for CHJ devices using SubPc and SubNc as the interlayer, respectively. The black dashed line in each plot represents the reference interlayer/C_{60} SHJ device without an EDL. The onset of s-kink behavior is most apparent in **Figure 3.5c** and **Figure 3.5g**, where we normalize the photocurrent for each device to its own J_{sc}. This provides a useful metric for the shape of the device curve regardless of the J_{sc}, and more clearly illustrates that the onset of s-kink behavior in the device is due to field inversion (and resultant shutting down of photocurrent production) at $V_a < V_{oc}$. Furthermore, in comparing the *J-V* curves of the devices under no illumination, we note that the dark current at V_{oc} is 10-100x lower in the CHJs than in the SHJ reference device without an EDL. Lower dark currents at biases close to V_{oc} indicate a decrease in recombination of injected charges at the dominant heterojunction, providing further evidence for a buildup of holes at the EDL/interlayer interface. If injected holes are unable to reach the interlayer/C_{60} interface, they cannot recombine with injected electrons and contribute to dark current.

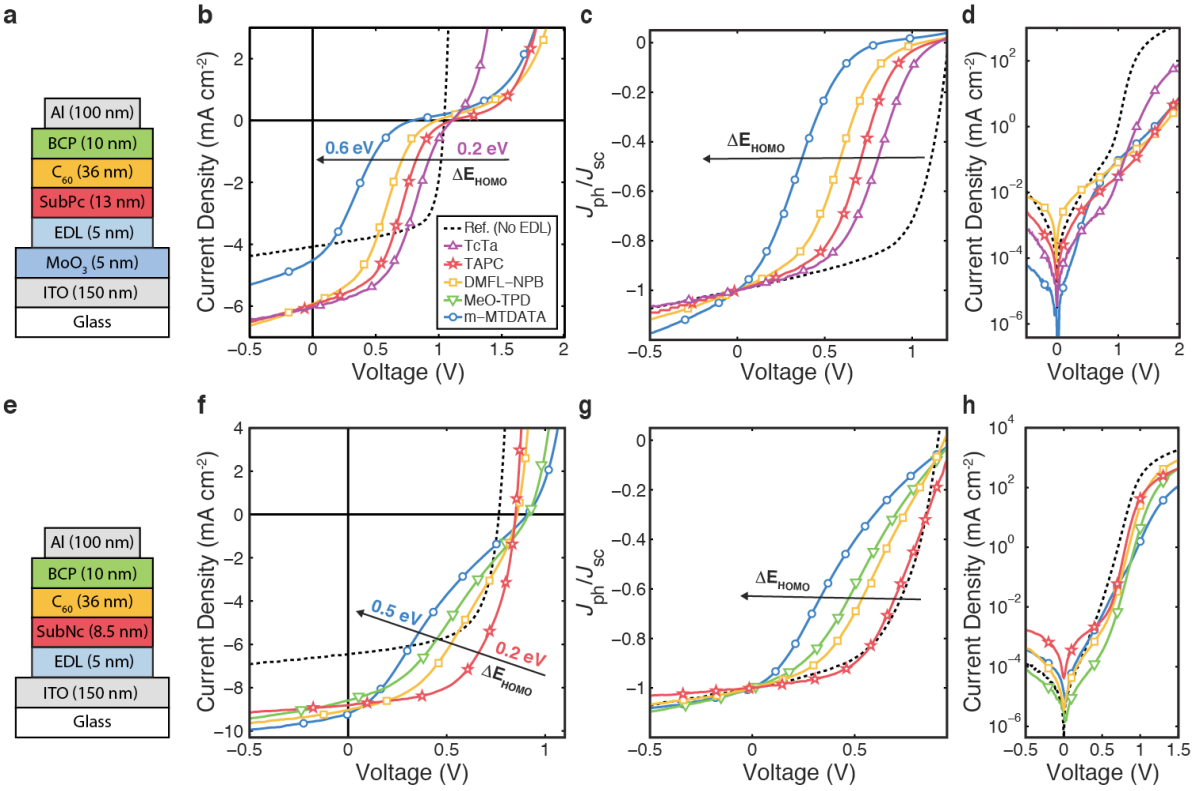

Figure 3.5 The effect of ΔE_{HOMO} on the *J-V* performance of CHJ devices. a)-d) shows the device structures, *J-V*, normalized photocurrent, and dark current for devices using SubPc as the interlayer. The device structure for SubPc devices was (all thicknesses in nm) ITO/5 MoO_3/5 EDL/13 SubPc/36 C_{60}/10 BCP/100 Al. e)-h) shows the same data for devices using SubNc as an interlayer. The SubNc device structure was ITO/5 EDL/8.5 SubNc/36 C_{60}/10 BCP/100 Al. Reference devices with no EDL are represented by dashed black lines.

3.3.4 Dependence of CHJ V_{MPP} on ΔE_{HOMO} and V_{MPP} of Subjunctions

To summarize the combined contributions of field inversion and voltage-limited operation, we measured the *J-V* performance of all EDL/interlayer and interlayer/C_{60} SHJ devices, extracting the V_{MPP} for each (performance parameters for all devices can be found in **Table 3.1** and **Table 3.2**). **Figure 3.6a** plots the normalized V_{MPP} of each CHJ versus $\Delta E_{HOMO,}$ with the normalization factor *f* defined as:

$$f = \frac{1}{\min\left(V_{MPP}^{EDL/int}, V_{MPP}^{int/C60}\right)} \tag{3.3}$$

where *f* is the inverse of the minimum V_{MPP} of either subjunction operating in the CHJ (this normalization factor is based on our assumption in Section 3.3.2 that the CHJ V_{MPP} will be

limited by the lowest V_{MPP} of either subjunction). Remarkably, the data collapse onto a single line, indicating that for $\Delta E_{HOMO} < 0.2$ eV, the CHJ is primarily limited by the lowest subjunction V_{MPP} and operates purely as a set of parallel diodes. However, for $\Delta E_{HOMO} > 0.2$ eV, the hole injection barrier becomes significant enough to shut down photocurrent production before V_{oc}, decreasing V_{MPP} below that of either subjunction. This 0.2 eV threshold is consistent with what has been shown in bilayer organic light-emitting diodes, where efficient hole injection into the electron transport layer occurs only when ΔE_{HOMO} is less than 0.1 - 0.3 eV.[77-79] Thus, **Figure 3.6a** encompasses the critical parameters that will determine the MPP of a CHJ device. From the plot, we conclude that for a high efficiency CHJ, the V_{MPP} of each subjunction must be closely matched and ΔE_{HOMO} between the EDL and interlayer should be kept below 0.2 eV.

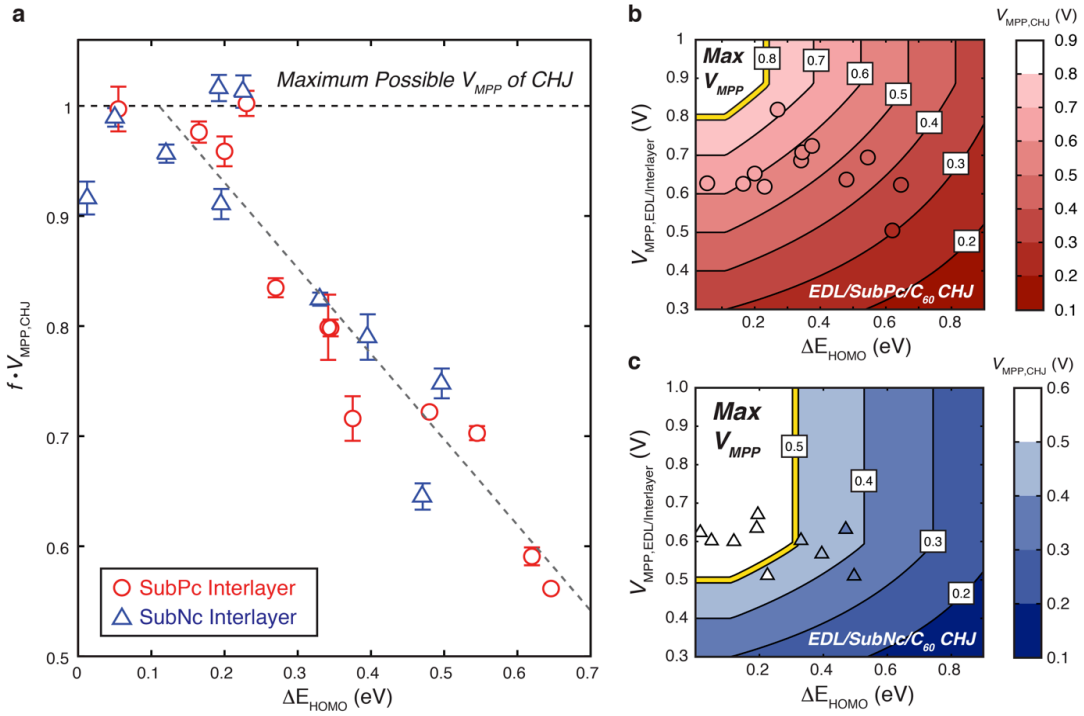

Figure 3.6 a) A plot of each CHJ V_{MPP} normalized by the minimum V_{MPP} of its constituent subjunctions versus ΔE_{HOMO}, as defined in Equation (3.3). The dashed horizontal line = 1 represents the maximum possible V_{MPP} of the CHJ based on each subcell. Beyond $\Delta E_{HOMO} \approx 0.2$ eV, the CHJ V_{MPP} is further lowered due to a decrease in V_{bi} (and therefore photocurrent) under forward bias. Error bars represent standard deviations calculated from six or more devices. b) and c) are contour plots of simulated V_{MPP} for CHJ devices with SubPc and SubNc interlayers, respectively. CHJ V_{MPP} is determined by the minimum V_{MPP} of either subjunction and further decreased by ΔE_{HOMO}, dictated by the linear fit in (a), as given in Equation (3.7). Experimental data points (circles and triangles) for CHJ devices are plotted and colored corresponding to their experimentally determined V_{MPP}.

3.3.5 J-V Curves of CHJ Devices

In **Figure 3.7a** and **Figure 3.7b** we show the experimentally determined *J-V* curves (CHJ and SHJs corresponding to each subjunction) for the TcTa/SubPc/C_{60} and BPAPF/SubNc/C_{60} systems, respectively. In **Table 3.1** and **Table 3.2** we provide tabulated *J-V* performance parameters for all SHJs (EDL/interlayer and interlayer/C_{60}) and all CHJs (5 nm EDL/interlayer/C_{60}) used in this study. Even with a nominal ΔE_{HOMO} = 0.02 eV, as is the case with the BPAPF/SubNc heterojunction, there can still be efficient dissociation of excitons (and photocurrent production) at short-circuit conditions.

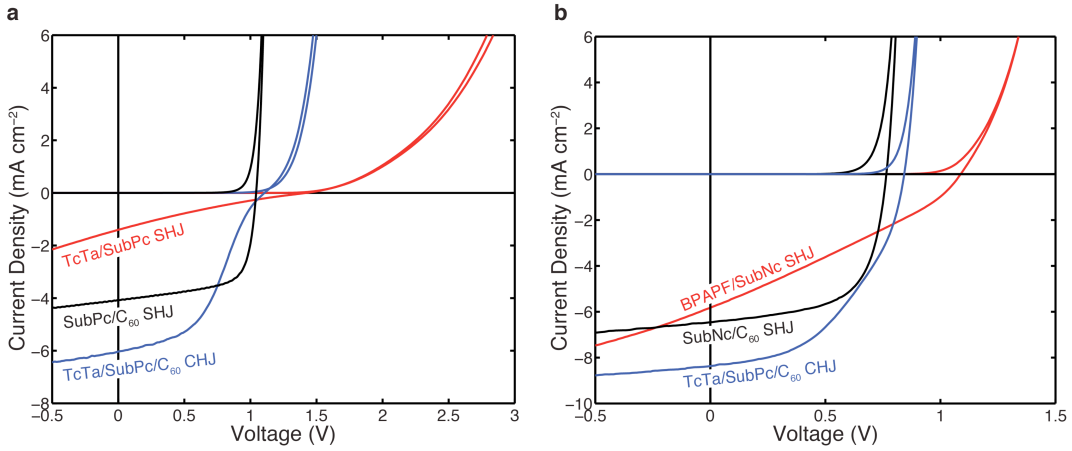

Figure 3.7 *J-V* curves for a) TcTa/SubPc SHJ, SubPc/C_{60} SHJ, and TcTa/SubPc/C_{60} CHJ devices; and b) BPAPF/SubNc SHJ, SubNc/C_{60} SHJ, and BPAPF/SubNc/C_{60} CHJ devices.

Table 3.1 Performance parameters for SHJ and CHJ devices utilizing SubPc in this study. Standard deviations, as calculated from at least six different devices, for V_{oc}, J_{sc}, FF, PCE, and V_{MPP} were all less than 3%, 11%, 6%, 12%, and 4%, respectively.

Device	ΔE_{HOMO} (eV)	V_{oc} (V)	J_{sc} (mA cm^{-2})	FF (%)	PCE (%)	V_{MPP} (V)
SubPc/C_{60} SHJ	-	1.04	3.9	67	2.74	0.89
TcTa/SubPc SHJ	0.05	1.41	1.5	21	0.44	0.63
TcTa/SubPc/C_{60} CHJ		1.11	5.8	44	2.81	0.63
BPAPF/SubPc SHJ	0.17	1.42	1.3	20	0.38	0.63
BPAPF/SubPc/C_{60} CHJ		1.15	5.7	41	2.70	0.61
α-NPD/SubPc SHJ	0.20	1.35	1.9	23	0.60	0.65
α-NPD/SubPc/C_{60} CHJ		1.13	5.7	43	2.76	0.63
HMTPD/SubPc SHJ	0.23	1.38	1.4	21	0.40	0.62
HMTPD/SubPc/C_{60} CHJ		1.11	5.7	42	2.69	0.62
TPTPA/SubPc SHJ	0.27	1.33	3.1	38	1.58	0.82
TPTPA/SubPc/C_{60} CHJ		1.03	5.3	51	2.79	0.68
TAPC/SubPc SHJ	0.34	1.30	1.9	27	0.65	0.69
TAPC/SubPc/C_{60} CHJ		1.10	5.8	38	2.42	0.55
NPB/SubPc/SHJ	0.35	1.32	1.9	28	0.71	0.71
NPB/SubPc/C_{60} CHJ		1.12	6.0	38	2.60	0.57
TPD/SubPc SHJ	0.38	1.26	2.0	30	0.77	0.72
TPD/SubPc/C_{60} CHJ		1.08	5.8	36	2.25	0.52
DMFL-NPB/SubPc SHJ	0.48	1.17	1.9	31	0.65	0.64
DMFL-NPB/SubPc/C_{60} CHJ		0.97	5.6	34	1.85	0.46
MeO-TPD/SubPc SHJ	0.55	1.14	1.6	34	0.62	0.69
MeO-TPD/SubPc/C_{60} CHJ		0.93	5.1	39	1.86	0.49
m-MTDATA/SubPc SHJ	0.62	1.08	1.2	24	0.33	0.51
m-MTDATA/SubPc/C_{60} CHJ		0.79	4.4	23	0.80	0.30
2T-NATA/SubPc SHJ	0.65	1.07	2.0	33	0.70	0.62
2T-NATA/SubPc/C_{60} CHJ		0.89	5.2	28	1.31	0.35

Table 3.2 Performance parameters for SHJ and CHJ devices using SubNc in this study. Standard deviations, as calculated from at least six different devices, for V_{oc}, J_{sc}, FF, PCE, and V_{MPP} were all less than 2%, 9%, 7%, 10%, and 3%, respectively.

Device	ΔE_{HOMO} (eV)	V_{oc} (V)	J_{sc} (mA cm^{-2})	FF (%)	PCE (%)	V_{MPP} (V)
SubNc/C_{60} SHJ	-	0.75	5.9	62	2.76	0.59
BPAPF/SubNc SHJ	0.02	1.08	5.1	30	1.64	0.62
BPAPF/SubNc/C_{60} CHJ		0.84	8.0	47	3.18	0.54
α-NPD/SubNc SHJ	0.05	1.08	4.7	29	1.50	0.60
α-NPD/SubNc/C_{60} CHJ		0.86	8.0	53	3.59	0.59
TPTPA/SubNc SHJ	0.12	1.09	5.1	29	1.63	0.60
TPTPA/SubNc/C_{60} CHJ		0.86	8.2	51	3.65	0.57
TAPC/SubNc SHJ	0.19	1.11	5.2	30	1.73	0.63
TAPC/SubNc/C_{60} CHJ		0.85	8.3	58	4.05	0.60
NPB/SubNc/SHJ	0.20	1.11	5.6	34	2.10	0.67
NPB/SubNc/C_{60} CHJ		0.84	8.2	50	3.46	0.54
TPD/SubNc SHJ	0.23	1.00	1.9	25	0.48	0.51
TPD/SubNc/C_{60} CHJ		0.86	7.2	44	2.70	0.52
DMFL-NPB/SubNc SHJ	0.33	1.05	4.0	29	1.21	0.60
DMFL-NPB/SubNc/C_{60} CHJ		0.87	7.9	41	2.79	0.49
MeO-TPD/SubNc SHJ	0.40	1.04	3.1	28	0.93	0.57
MeO-TPD/SubNc/C_{60} CHJ		0.91	7.4	33	2.21	0.45
m-MTDATA/SubNc SHJ	0.47	1.06	4.9	32	1.63	0.63
m-MTDATA/SubNc/C_{60} CHJ		0.91	8.2	23	1.74	0.38
2T-NATA/SubNc SHJ	0.50	0.94	1.8	27	0.44	0.51
2T-NATA/SubNc/C_{60} CHJ		0.77	5.2	28	1.12	0.38

The HOMO levels of the EDL and interlayer materials were obtained *via* cyclic voltammetry on individual materials (detailed in Section 3.2.1). Within the devices, however, the HOMO levels and offset energies could conceivably vary due to band bending or intermixing at the active layer interfaces. Therefore, as with the estimation of each subjunction's V_{MPP} from the V_{MPP} of its SHJ

counterpart, the measured energy levels provide an approximate value that can be used for predicting CHJ device performance. It is likely that the variations in energy levels and V_{MPP} of each subjunction within the CHJs account for some of the data spread seen in **Figure 3.6a**.

3.3.6 Champion Device Performance

In **Figure 3.8**, we show the device results for the best CHJs (highest PCE) created from the combinatorial study using either a SubPc (solid red lines) or SubNc (solid blue lines) interlayer. Both data sets are compared to the reference interlayer/C_{60} SHJ devices, which are plotted with dashed lines. We note that these results are consistent with those reported for SubPc/C_{60} and SubNc/C_{60} devices using other HTL materials.[42,80] **Figure 3.8a** shows that the J_{sc} for both CHJs is significantly higher than the J_{sc} of the respective reference devices due to the large increase in EQE (**Figure 3.8b**) and IQE (**Figure 3.8c**) of the interlayers. Here, as discussed in Section 1.7.4, we have defined the IQE as:

$$IQE(\lambda) = \frac{EQE(\lambda)}{\eta_{Abs}(\lambda)} \tag{3.4}$$

where EQE(λ) is the experimentally determined external quantum efficiency of the device and $\eta_{Abs}(\lambda)$ is the absorption of only the active layers at wavelength λ, as determined by optical modeling (fittings by the optical model are shown in **Figure 3.9**). Impressively, the IQE of the SubNc interlayer within the cascade approaches 100% (>90% from 650 nm – 700 nm, with a peak value of 99%), meaning that nearly all photogenerated excitons in the SubNc are converted to electrical current. Furthermore, the V_{MPP} of the SubNc CHJ is insensitive to the insertion of a 5 nm TAPC EDL between the ITO anode and the SubNc layer, while the SubPc CHJ sees a large drop in V_{MPP}, consistent results in Chapter 2.[33] Consequently, the FF of the SubNc/C_{60} SHJ (62%) is largely maintained in the TAPC/SubNc/C_{60} CHJ (58%), whereas the FF of the TcTa/SubPc/C_{60} CHJ (44%) decreases significantly compared to the SubPc/C_{60} SHJ (67%). This

makes empirical sense, considering the V_{MPP} of each SubPc subjunction (0.63 ± 0.01 V for the TcTa/SubPc SHJ and 0.89 ± 0.01 V for the SubPc/C_{60} SHJ), with the TcTa/SubPc subjuncton limiting the overall V_{MPP} of the CHJ to 0.63 ± 0.01 V. On the other hand, the V_{MPP} of each SubNc subjunction is closely matched (0.63 ± 0.01 V for the TAPC/SubNc SHJ and 0.59 ± 0.01 V for the SubNc/C_{60} SHJ), leading to a CHJ V_{MPP} = 0.60 ± 0.01 V.

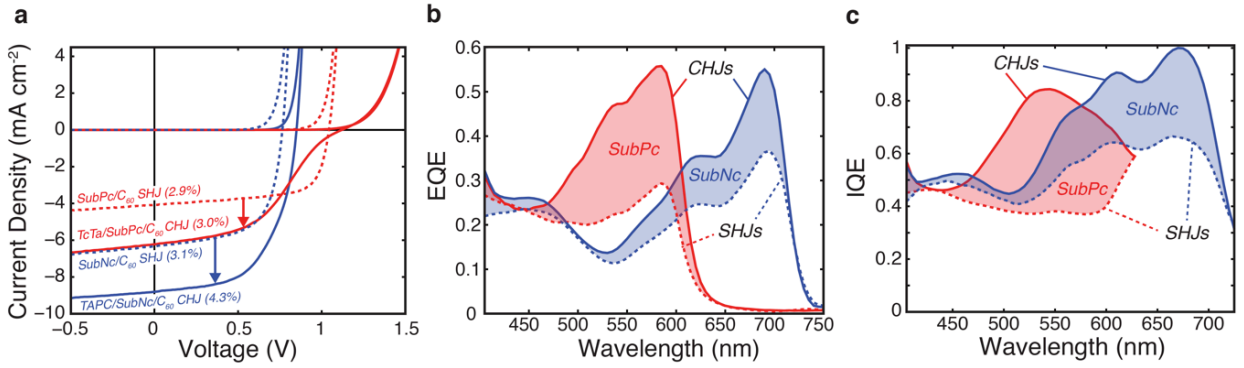

Figure 3.8 a) *J-V* curves, b) EQE, and c) IQE of optimized CHJ devices and the corresponding reference SHJ devices with no EDL. Results are shown for cascades with both SubPc and SubNc interlayers. IQE is defined as the experimental EQE divided by the modeled active layer absorption. The increase in J_{sc} in both CHJs can be explained by a substantial increase in the IQE and EQE of the interlayers. In the SubNc interlayer, the peak IQE is >99%. The more pronounced s-kink behavior in the SubPc CHJ is due to the limiting V_{MPP} of the TcTa/SubPc subjunctions.

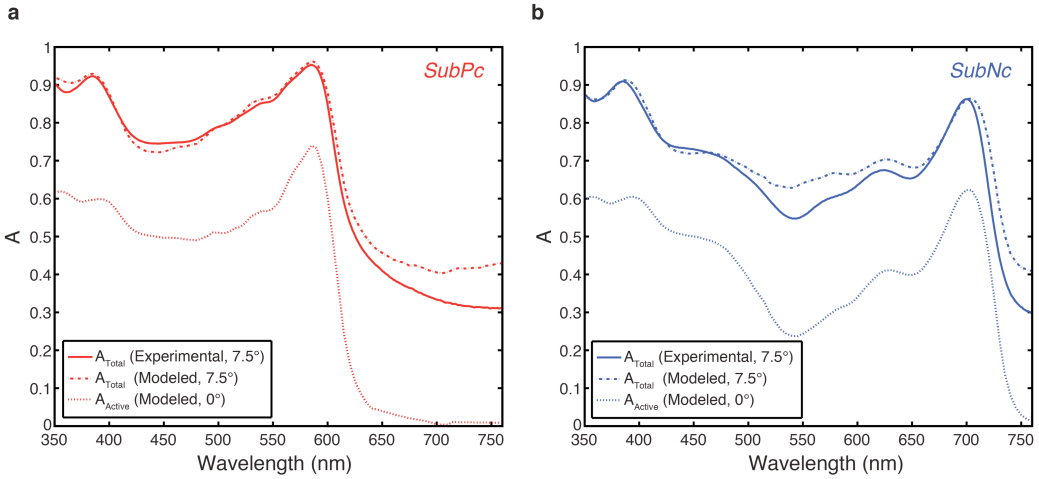

Figure 3.9 Experimental and modeled absorption spectra of a) SubPc/C_{60} and b) SubNc/C_{60} CHJ devices. Total absorption of the device stack was measured and modeled at an incidence angle of 7.5°. Active layer absorption (absorption in only the interlayer and C_{60} layers) was modeled at normal incidence and used in calculating the IQE of device stacks.

3.3.7 V_{oc} Limitations in CHJ Devices

Recently, Cnops *et al.* suggested that the V_{oc} of CHJs should be limited by the energy levels of the outermost active layers.[81] This limitation on the V_{oc} would occur due to the additional losses in energy as the free charges are extracted from the device. In **Figure 3.10**, we plot the V_{oc} of each CHJ versus $\Delta E_{HL}^{EDL/C60}$ (the difference in energy between the HOMO level of the EDL and the LUMO level of the C_{60} layer), and indeed we see that the V_{oc} can be limited for a small enough $\Delta E_{HL}^{EDL/C60}$. In the CHJ devices with a SubPc interlayer, we observe a crossover point at $\Delta E_{HL}^{EDL/C60} \approx 1.45$ eV ($\Delta E_{HOMO} \approx 0.35$ eV), above which the V_{oc} remains relatively constant, and below which the V_{oc} decreases monotonically with decreasing $\Delta E_{HL}^{EDL/C60}$. A similar transition is inferred at ≈ 1.18 eV ($\Delta E_{HOMO} \approx 0.48$ eV) for devices with a SubNc interlayer, however the limited data below this value makes it more approximate. Critically, any limitations in V_{oc} only occur for very small $\Delta E_{HL}^{EDL/C60}$ values. Conversely, for larger $\Delta E_{HL}^{EDL/C60}$ (smaller ΔE_{HOMO}) values, the CHJ devices actually exhibit an *increase* in V_{oc} compared to the reference interlayer/C_{60} SHJ, which we attribute to a decrease in dark current (**Figure 3.5d,h**). The black dotted line in **Figure 3.10** represents:

$$q \cdot V_{oc} = \Delta E_{HL}^{EDL/C60} - 0.3 \text{ eV} \quad (3.5)$$

indicating that the maximum possible V_{oc} of the CHJs is limited by $\Delta E_{HL}^{EDL/C60}$ and an effective binding energy of ~0.3 eV, consistent with our calculated $E_{B,PP}$ of the SubPc/C_{60} and SubNc/C_{60} heterojunctions. Since a majority of photocurrent in the CHJ is generated at the interlayer/C_{60} interface,[61] it is not surprising that the effective $E_{B,PP}$ of the CHJ is close to that of the interlayer/C_{60} subjunction.

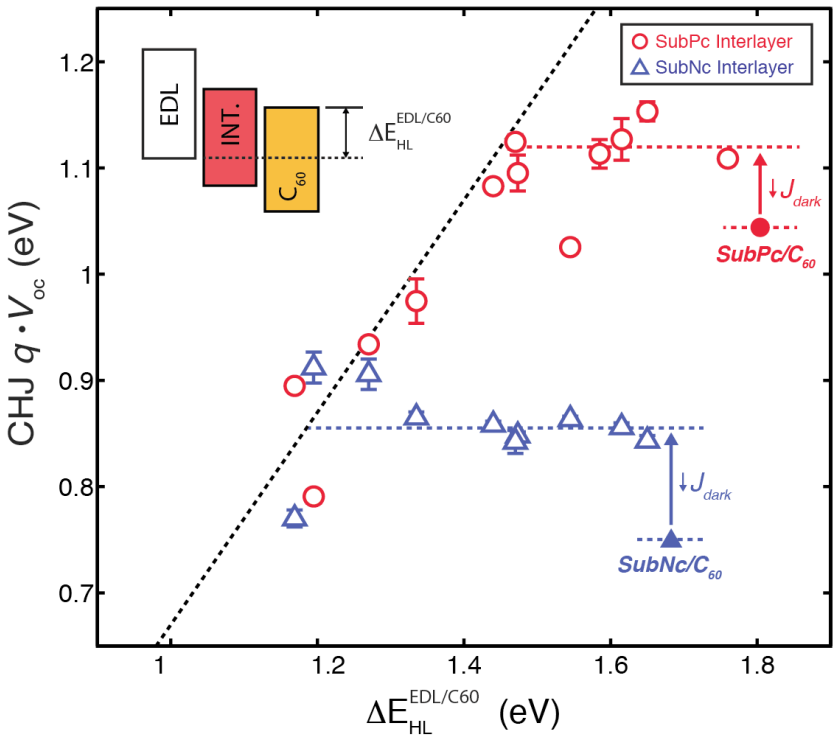

Figure 3.10 A plot of qV_{oc} for each CHJ device versus $\Delta E_{HL}^{EDL/C60}$ (the difference in HOMO and LUMO levels of the EDL and C_{60} layers). The V_{oc} of the CHJ devices increases initially upon insertion of an EDL due to a decrease in the dark current. As $\Delta E_{HL}^{EDL/C60}$ decreases, the V_{oc} of the CHJs remains relatively constant until it becomes limited by $\Delta E_{HL}^{EDL/C60}$ - $E_{B,PP}$. The diagonal black dotted line represents $\Delta E_{HL}^{EDL/C60}$ - 0.3 eV, indicating a binding energy of 0.3 eV (consistent with the fitted $E_{B,PP}$ in Section 3.3.8).

As demonstrated by the EDL/SubNc/C_{60} devices, CHJs with interlayer/acceptor subjunctions exhibiting high recombination losses can employ donor layers with a larger ΔE_{HOMO} before V_{oc} begins to drop. However, as we have already established that ΔE_{HOMO} should be kept to less than 0.2 eV to minimize charge injection barriers in the devices, properly designed CHJs will not be voltage-limited. Instead, CHJ operation can substantially reduce recombination losses and bring the V_{oc} closer to the theoretical maximum.

3.3.8 Onsager Braun Modeling for SHJ Devices

Here, we use the Onsager Braun modeling detailed in Section 1.8 to fit the normalized photocurrent for a SubPc/C_{60} junction measured under simulated AM1.5G illumination (100

mW/cm^2). As can be seen in **Figure 3.11**, the OB model produces a much higher FF than what is measured experimentally in such devices. Renshaw *et al.* have shown previously that photoconductivity (S_{pc}) must be accounted for to properly describe the photocurrent in OPVs (in particular SubPc/C_{60}) and resolve this discrepancy.[59] The total normalized photocurrent can be described by:

$$\frac{J_{ph}(V_a)}{J_{sc}} = \frac{S_{pc}}{J_{sc}} \cdot \left(V_a - V_{bi}\right) - f_{jxn} \cdot \eta_{PPd} \tag{3.6}$$

where $f_{jxn} = 1 - \frac{S_{pc} \cdot V_{bi}}{J_{sc}}$ is the fraction of photocurrent produced at short-circuit conditions from the heterojunction and not from bulk dissociation. From the slope of the photocurrent curve in reverse bias we obtained S_{pc} = 0.55 mA/cm^2-V; when S_{pc} was included in Equation (3.6), the experimental and modeled photocurrent were closely matched. Values of 0.95 V, 1.22 nm, and 10^8 Hz were used for V_{bi}, a_0, and k_r, respectively. Having determined the parameters for the SubPc/C_{60} SHJ device, it was then possible to solely vary the PP separation distance (and thus binding energy, $E_{B,PP}$) to observe its effect on the maximum power point voltage under realistic conditions. We note that the fitted values determined here are in close agreement with the reported literature values for these devices.[55]

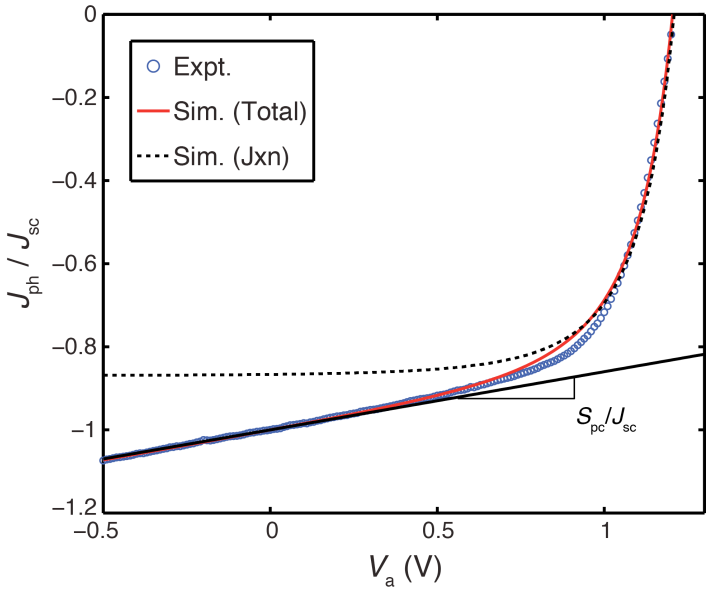

Figure 3.11 Normalized photocurrent versus applied bias for a SubPc/C_{60} SHJ device fitted to the OB model. Experimental data is shown (blue circles) to be in good agreement with the overall device fitting (solid red line) comprising contributions from dissociation at the heterojunction (dashed black line) and photoconductivity (solid black line).

3.3.9 Design Rules for CHJ Devices

These results can guide future CHJ device design, principally dictating that ΔE_{HOMO} be less than 0.2 eV and the polaron pair binding energy be minimized for the EDL/interlayer interface. It is also possible now to screen materials systems for their utility in CHJ configurations. In **Figure 3.6b** and **Figure 3.6c**, we extrapolate the relationship shown in **Figure 3.6a** to provide contour plots for predicting the V_{MPP} of an EDL/SubPc/C_{60} CHJ (**Figure 3.6b**) and an EDL/SubNc/C_{60} CHJ (**Figure 3.6c**) as a function of EDL/interlayer V_{MPP} and ΔE_{HOMO}. A linear fit of the universal trend in **Figure 3.6a** produces a general equation:

$$f \cdot V_{MPP,CHJ} = -(0.78 \cdot eV^{-1}) \cdot (\Delta E_{HOMO}) + 1.08 \tag{3.7}$$

with the caveat that the cascade V_{MPP} will not exceed the V_{MPP} of either subjunction. We note that Equation (3.7) implies no dependence of V_{MPP} on other material properties such as charge mobility. In Section 3.3.10, we consider such charge mobility effects and in fact show a strong correlation between HOMO level and hole mobility. However, we see no apparent dependence

of CHJ V_{MPP} on EDL layer thicknesses, and thus conclude that any effects due to mobility are negligible or secondary to the injection barrier introduced by ΔE_{HOMO}. As an aside, the apparent relationship between HOMO level and hole mobility for these materials warrants further investigation, as it could provide further insight into previous studies with similar systems where changes in device performance were attributed primarily to variations in the hole mobility of the HTL.[42,82]

Finally, from comparing the two contour plots (**Figure 3.6b** and **c**), we can see that a much lower EDL/interlayer V_{MPP} is required to achieve maximum V_{MPP} in the SubNc CHJ as compared to the SubPc CHJ. In many cases, the simplest route to a high-performance CHJ device may be choosing a base device system with higher J_{sc} and lower V_{oc} or V_{MPP}. By "trading" J_{sc} for V_{MPP}, the PCE of the reference SHJ device can remain high, while lowering the required V_{MPP} of the introduced subjunction in the CHJ.

3.3.10 Effect of EDL Mobility on CHJ Performance

To determine any effects of EDL mobility on the V_{MPP} of CHJ devices, we used time-of-flight methods to measure the hole mobility of select EDL materials (**Figure 3.12a**). The remaining mobilities were taken from time-of-flight measurements reported in literature.[83-86] In **Figure 3.12b**, we plot the zero-field hole mobilities ($\mu_{h,0}$) of each EDL material versus its HOMO level energy; from this plot, there is a noticeable trend between $\mu_{h,0}$ and the HOMO level. HOMO levels and mobility parameters are provided in **Table 3.3**. Assuming a Poole-Frenkel dependence of the carrier mobility on electric field,[87] the mobility can be expressed as:

$$\mu_h(E) = \mu_{h,0} \exp(\gamma E^{1/2}) \tag{3.8}$$

where $\mu_{h,0}$ is the zero-field hole mobility, γ is the field activation parameter, and E is the applied electric field.

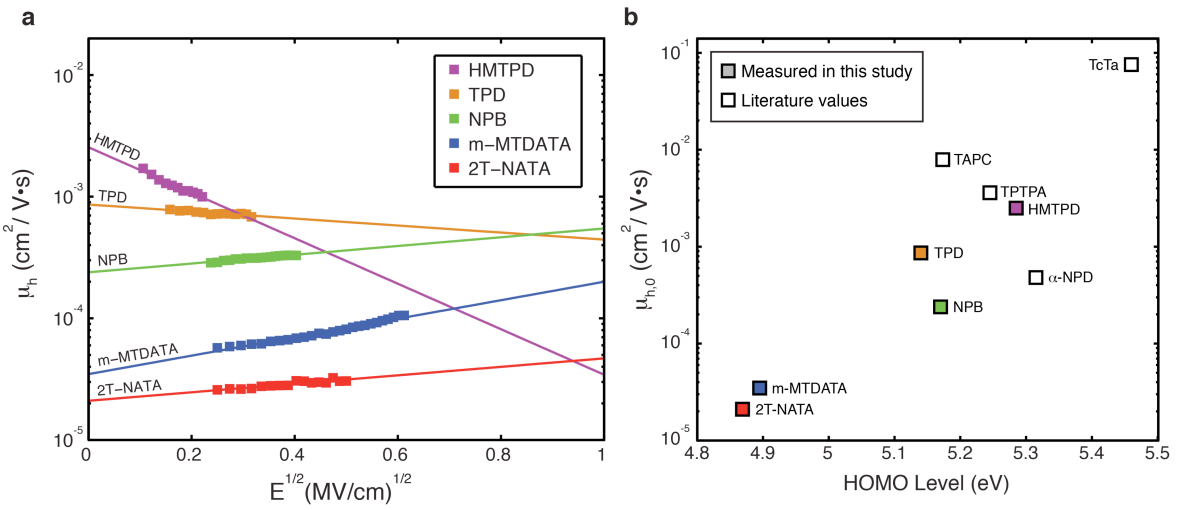

Figure 3.12 a) Field-dependent hole mobilities of EDL materials measured via time-of-flight methods. b) Zero-field hole mobilities of EDL materials versus HOMO energy level. Colored squares were measured in this study and white squares are (time-of-flight) values taken from literature.

Since both μ_h and the introduced hole injection barrier correlate with ΔE_{HOMO}, we varied EDL thickness for each device set from 5 nm to 10 nm to deconvolve any effects the two properties may have on device performance. Because the injection barrier remains constant regardless of EDL thickness, any changes in performance versus thickness could be attributed to mobility differences in the EDL layer. The normalized V_{MPP} for all CHJ devices can be seen in **Figure 3.13a**. While the EDL thickness variation introduces an additional spread to the data set, Equation (3.7) still provides a good overall fit. Furthermore, as can be seen from **Figure 3.13b**, there is no clear trend in V_{MPP} as a function of EDL thickness. In fact, some CHJ devices experience an *increase* in V_{MPP} with a thicker EDL layer. While the physical reasons for variations in CHJ performance versus EDL thickness warrant further investigation, they are outside the scope of this study. By varying EDL thickness with no clear trend for changes in V_{MPP}, we conclude that any effects due to changes in mobility are secondary and much smaller than those due to the introduced injection barrier with energy of ΔE_{HOMO}.

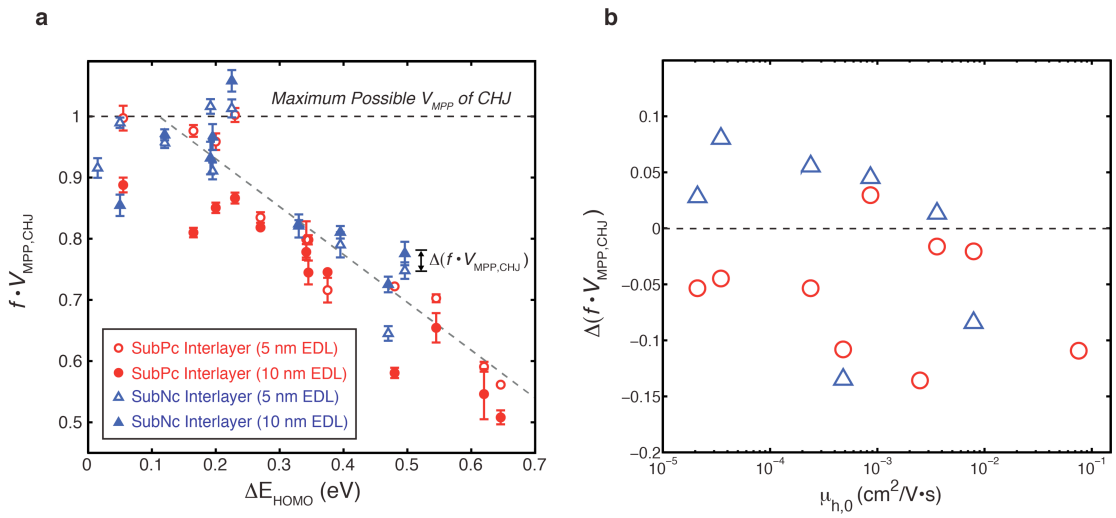

Figure 3.13 a) A plot of each CHJ V_{MPP} normalized by the minimum V_{MPP} of its constituent subjunctions versus ΔE_{HOMO} (the energy offset between the HOMO levels of the EDL and the interlayer). Whereas **Figure 3.6a** only shows EDL thicknesses of 5 nm, here we also show EDL thicknesses of 10 nm for both interlayers. b) The difference in normalized V_{MPP} for CHJs with 5 nm and 10 nm EDL thicknesses vs. the zero-field hole mobility of each EDL material. Because there is no clear dependence of V_{MPP} on EDL thickness, we conclude that any changes in CHJ V_{MPP} due to EDL material variation are due primarily to the introduced injection barrier with energy of ΔE_{HOMO}, with effects of mobility variation either negligible or secondary.

Table 3.3 Mobility parameters for all EDL materials, as determined by time-of-flight measurements. Mobility values taken from literature are noted. All other mobility values and HOMO levels were measured in this study.

Material	HOMO Level (eV)	$\mu_{h,0}$ (cm^2 V^{-1} s^{-1})	γ (cm V^{-1})$^{1/2}$	Source
TcTa	5.46	7.56E-02	5.62E-04	[83]
BPAPF	5.35	-	-	-
α-NPD	5.32	4.80E-04	5.30E-04	[84]
HMTPD	5.29	2.50E-03	-4.30E-03	This study
TPTPA	5.25	3.60E-03	2.90E-03	[85]
TAPC	5.17	7.90E-03	8.81E-04	[86]
NPB	5.17	2.39E-04	8.30E-04	This study
TPD	5.14	8.622E-04	-6.632E-04	This study
DMFL-NPB	5.04	-	-	-
MeO-TPD	4.97	-	-	-
m-MTDATA	4.90	3.478E-05	1.700E-03	This study
2T-NATA	4.87	2.100E-05	8.028E-04	This study

3.4 Conclusions

We have shown that CHJ architectures are viable options for high-efficiency planar OPVs, primarily due to their ~100% IQE within the interlayer. To ensure high fill factor, the V_{MPP} of each subjunction must be matched and the HOMO level offset between the EDL and interlayer should be < 0.2 eV. Using these proposed design rules, we demonstrated a 46% increase in the power conversion efficiency of a SubNc/C_{60} planar device by introducing a transparent EDL between SubNc and the ITO anode (from 2.8 ± 0.2% to 4.1 ± 0.2%). By introducing the 5 nm layer of TAPC, the IQE of the SubNc layer increased from 66% to 99% at its peak, while the high fill factor of the subjunctions was largely maintained.

While the PCE was significantly enhanced in properly designed CHJs, J_{sc} could be improved further through active layer absorption. Because the presence of two heterojunctions relaxes the tradeoff between absorption and exciton diffusion, the interlayer thickness can be increased to maximize absorption. Some materials are more suitable for this than others; Verreet *et al.* recently showed that replacing C_{60} with hexachlorinated boron subphthalocyanine chloride allowed the SubNc layer thickness to increase upwards of 20 nm.[80] Furthermore, by using a smaller bandgap material in place of the transparent EDL to increase spectral coverage, device J_{sc} should increase without any additional drop in V_{oc}, V_{MPP}, or FF. Because the CHJ devices have such high IQE, they are also ideal candidates for use as sub-cells in series-connected tandems, potentially allowing for high efficiency OPVs comprising six or more active layers with complementary absorption peaks.

Chapter 4

The Role of Interlayer Förster Resonant Energy Transfer in Single- and Multi-Junction OPVs

4.1 Introduction

Because interlayer Förster resonant energy transfer (FRET), the non-radiative dipole-dipole coupling of excitons from one layer to another, can occur over larger distances than the typical L_D, it has been suggested as a possible mechanism for improving diffusion efficiency (η_{Diff}) in OPVs. However, while previous studies considering Förster transfer have provided an important groundwork for what we present in this chapter, they have all assumed 100% harvesting of excitons once they have undergone energy transfer,[37,81,88] Here we develop new methods for tracking the excitons throughout the FRET-mediated diffusion process and determine those assumptions to be inaccurate. Specifically, we show that the diffusion efficiency of the Förster acceptor (FA) layer plays a crucial role in determining the overall diffusion efficiency of the device. In fact, for FA layers with low L_D, we show that the FRET process can actually *decrease* η_{Diff}. This result contrasts with conclusions that have been previously drawn from simple photoluminescence quenching experiments where interlayer FRET universally appears to *improve* η_{Diff}. Using both modeling and experiments, we consider the FRET process in both SHJ and CHJ devices, and show how device configurations can be properly optimized based on

known material properties. Furthermore, we use the results from this study to provide design rules for future OPV active layer materials in high efficiency devices.

4.2 Theory

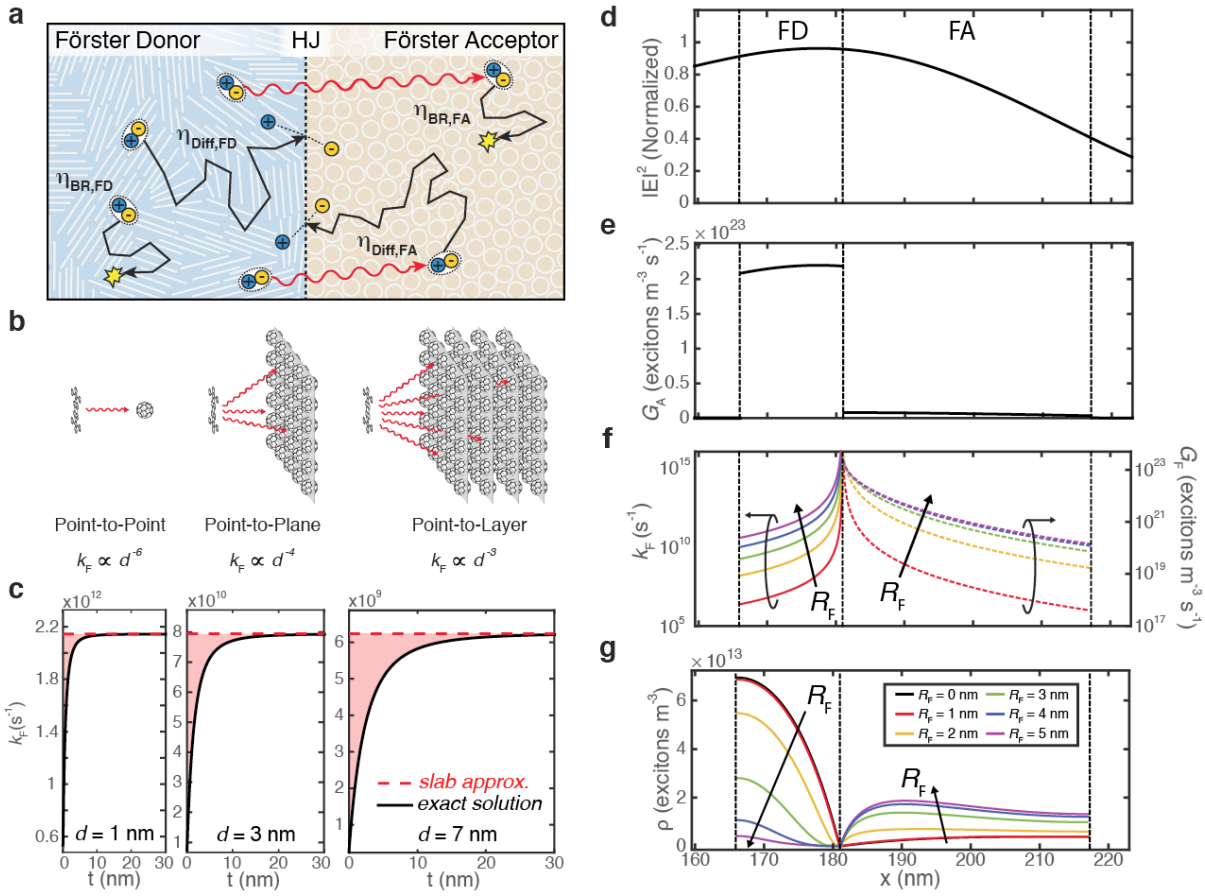

Figure 4.1 a) Possible outcomes for excitons generated in the Förster donor of an OPV device. $\eta_{Diff,FD}$: diffusion to the heterojunction without transfer into the Förster acceptor, $\eta_{BR,FD}$: recombination in the bulk of the FD before reaching the heterojunction, $\eta_{Diff,FA}$: transfer to the FA and diffusion in the FA to the heterojunction, and $\eta_{BR,FA}$: transfer to the FA and recombination in the bulk of the FA before reaching the heterojunction. b) Schematic representations of Förster transfer for point-to-point, point-to-plane, and point-to-layer configurations and the distance-dependent rates for each. c) The Förster transfer rate, k_F, from the FD to the FA as a function of FA thickness (t). In the case where $t >> d$, the slab approximation in Eq. (4.5) can be used. Modeled d) electric field, e) optical exciton generation rate, f) Förster transfer rate (solid lines) and Förster generation rate (dotted lines), and g) exciton population density profiles in a SHJ bilayer device.

As discussed in Section 1.6.1, exciton diffusion in OPVs can occur *via* thermally assisted hopping as well as self-Förster transfer. Recently, Menke *et al.*[89] developed a rigorous model for determining the effect of *intra*-layer FRET (i.e. exciton transfer between molecules of the same

material) on L_D of materials. In this chapter, we develop a model that accounts for *inter*-layer FRET (i.e. transfer between layers of differing materials). The rate of energy transfer (k_F) between two weakly coupled dipoles (**Figure 4.1b**) can be expressed as:

$$k_{F,Point-to-Point} = \frac{1}{\tau}\left(\frac{R_F}{d}\right)^6 \tag{4.1}$$

where τ is the dipole (exciton) lifetime and d is the separation distance between the two dipoles. The Förster radius for energy transfer (R_F) represents the distance at which 50% of energy from the Förster donor (FD) is dissipated *via* FRET to the Förster acceptor (FA), and is expressed as:

$$R_F^6 = \frac{9\eta_{PL}\kappa^2}{128\pi^5 n^4}\int \lambda^4 PL_{FD}(\lambda)\sigma_A(\lambda)d\lambda \tag{4.2}$$

where η_{PL} is the photoluminescent quantum yield of chromophores in the FD, κ is the dipole orientation factor, n is the index of refraction of the FD medium weighted by the overlap integral, λ is the wavelength, PL_{FD} is the probability density of the FD emission spectrum, and σ_A is the absorption cross-section of the Förster acceptor.

Compared to the point-to-point transfer rate for two dipoles, the transfer rate increases drastically for transfer from a point to a plane of FA chromophores:

$$k_{F,Point-to-Plane} = \frac{\pi C_A R_F^6}{2d^4\tau} \tag{4.3}$$

where C_A is the chromophore (molecular) density of the FA and d is the shortest distance from the dipole in the FD to the FA plane. For transfer from a point to a FA layer with finite thickness, the point-to-plane transfer rates are integrated over the FA layer thickness, providing the equation:

$$k_{F,Point-to-Layer} = \frac{\pi C_A R_F^6}{6\tau}\left(\frac{1}{d^3} - \frac{1}{(d+t_{FA})^3}\right) \tag{4.4}$$

where d is the shortest distance from the dipole in the FD to the surface of the FA layer. For thick FA layers ($t_{EA} >> d$), the energy transfer rate converges to the rate for an infinite slab:

$$k_{F,Point-to-Slab} = \frac{\pi C_A R_F^6}{6\tau d^3} \tag{4.5}$$

In **Figure 4.1e**, we illustrate the effectiveness of the slab approximation. As indicated by the shaded red regions, for large separation distances or small FA thicknesses, the slab approximation is not accurate. Thus we use the explicit form of $k_{F,Point-to-Layer}$ for all simulations in this study.

To account for Förster transfer in any active layer, we propose a modified form of the drift diffusion model detailed in Chapter 1:[12]

$$\frac{d\rho}{dt} = D\frac{d^2\rho}{dx^2} - \frac{\rho}{\tau} + G_A - k_F\rho + G_F \tag{4.6}$$

where ρ is the spatially varying exciton density and D is the exciton diffusivity. In Equation (4.6, the first term on the right corresponds to exciton diffusion, $1/\tau$ is the rate of bulk recombination, k_F is the rate of Förster transfer of excitons out of the layer, and G_A and G_F are the generation rates from optical absorption and Förster transfer into the layer, respectively. Once the steady state exciton population profile is determined within all ED layers, the exciton generation rate due to incoming Förster transfer in EA layers can be calculated by integrating over each FD layer:

$$G_F = \int_{ED} k_{F,Point-to-Plane}(d) \cdot \rho(x)\, dx \tag{4.7}$$

Figure 4.1e and **Figure 4.1f** show the modeled k_F, G_F, and ρ within a theoretical DBP/C_{60} bilayer SHJ device. As R_F increases, k_F increases in the FD (DBP) layer, resulting in a concomitant increase in G_F within the FA (C_{60}) layer. Consequently, the steady state exciton

population density is depleted from the FD and transferred into the FA. As we will discuss in more detail later, transfer of excitons from the FD to the FA means that the diffusion efficiency of excitons originally generated in the FD will be affected by a number of factors such as the FA diffusion length.

4.3 Experiment

4.3.1 Thin Film and Device Preparation

Glass and ITO substrates were cleaned *via* sonication in soapy water, deionized water, acetone, and isopropanol, followed by boiling in isopropanol and 10 minutes of UV-Ozone treatment. Organic and metal films were grown *via* vacuum thermal evaporation in an Angstrom Engineering system. TPTPA, DBP, and C_{60} were deposited at 1 Å/s; Cl_6SubPc, Ag, and MoO_3 at 0.5 Å/s; BCP at 0.6 Å/s; and SubNc at 0.2 Å/s (to prevent crystallization and high roughness of the SubNc layer). PL samples were encapsulated within an inert nitrogen environment using a glass slide.

4.3.2 Optoelectronic Characterization

Characteristic current density-voltage curves of devices were measured using an HP 4156B precision semiconductor parameter analyzer under simulated solar illumination, using a Newport solar simulator (model# 91191-1000) calibrated by an NREL Si reference cell (Model PVM233 KG5) to AM1.5G illumination conditions (100 mW/cm^2). Reflection and transmission measurements were performed using a Perkin Elmer Lambda 750 UV/Vis/NIR spectrometer.

4.3.3 PL Measurements

Photoluminescent measurements were performed with a Photon Technology International QuantaMaster spectrofluorometer.

Results and Discussion

4.3.4 Material Properties

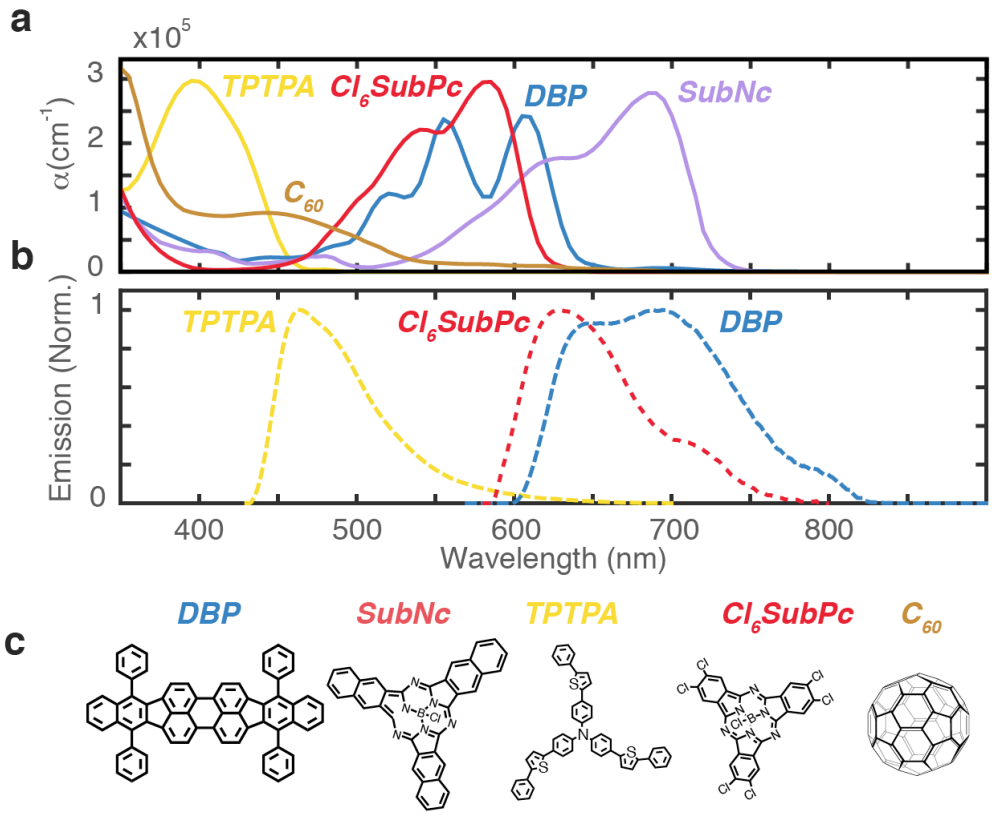

Figure 4.2 a) Absorption and b) emission spectra of all the active materials used in this study. c) Molecular structures of TPTPA, DBP, SubNc, Cl_6SubPc, and C_{60}.

In this study, we consider single heterojunction and cascade heterojunction devices utilizing combinations of five different active materials. The pertinent absorption spectra, emission spectra, and molecular structures for those materials are shown in **Figure 4.2**. TPTPA, DBP, and Cl_6SubPc were used as Förster donors, due to their relatively strong emission spectra and overlap with the absorption of DBP and Cl_6SubPc (TPTPA) and SubNc (DBP and Cl_6SubPc). While C_{60} does emit in the visible region, its quantum yield is so low (indistinguishable from zero when measured with our equipment) that any Förster transfer is negligible. We consider four Förster acceptors in this study: C_{60}, SubNc, Cl_6SubPc, and DBP. For all devices in which it was used,

TPTPA functioned solely as a FD sensitizer in an energy cascade configuration (i.e. there were no functional heterojunctions on either side of the TPTPA layer, so excitons generated in TPTPA had to be transferred into a neighboring active layer FA before contributing to photocurrent). DBP, C_{60}, Cl_6SubPc, and SubNc all functioned as active layers with at least one functional heterojunction. We note here that by the time of this thesis submission, the equipment necessary for measuring diffusion lengths and Förster radii[47] of the active materials in **Figure 4.2** was not available. Therefore, all values presented in this chapter are from fits to experimentally determined EQE spectra. All fitted values are kept constant across all devices, so while we were unable to directly measure each value, we believe that the strong fits presented in the following sections validate the proposed model. We were able to measure exciton lifetimes of Cl_6SubPc and DBP (**Figure 4.3**), and those values are also included in **Table 4.1**.

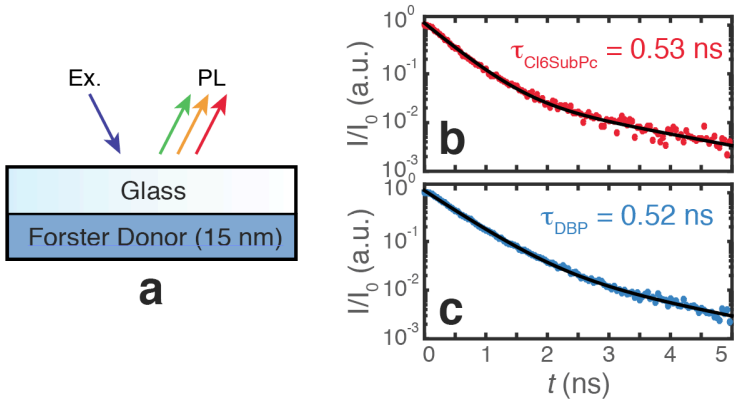

Figure 4.3 a) A schematic for measurements of exciton lifetime and measured exciton lifetime values for b) Cl_6SubPc and c) DBP.

Table 4.1 Fitted properties for all materials used in this study.

Material	L_D (nm)	τ (ns)	$R_{F,C60}$ (nm)	$R_{F,SubNc}$ (nm)
DBP	8.0	0.52 ± 0.10	1.5	2.3
SubNc	6.0	-	-	-
Cl_6SubPc	4.5	0.53 ± 0.03	-	4.0
C_{60}	17	-	-	-

4.3.5 FRET in DBP/C_{60} SHJ

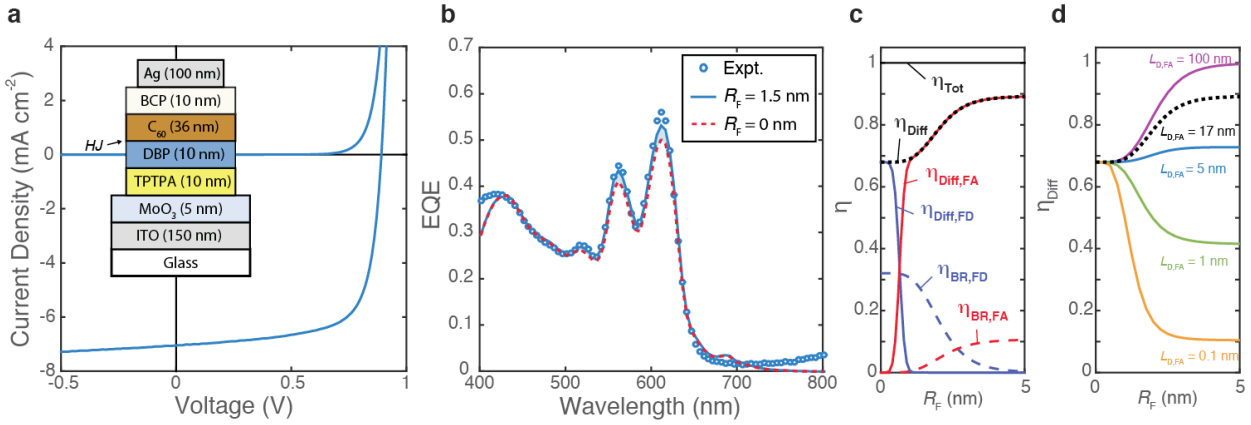

Figure 4.4 a) Measured light and dark *J-V* curves for a single heterojunction DBP/C_{60} device employing a TPTPA anode exciton blocking layer. b) Measured EQE spectra of the same device. Solid line corresponds to modeled EQE assuming a $L_{D,DBP}$ = 8 nm, $L_{D,C60}$ = 17 nm, and $R_{F,DBP:C60}$ = 1.5 nm. The dotted red line shows the model prediction for the same L_D values if FRET was not occurring (i.e. $R_{F,DBP:C60}$ = 0). c) Modeled diffusion and recombination efficiencies versus $R_{F,DBP:C60}$ corresponding to the processes illustrated in **Figure 4.1a**. (d) η_{Diff} versus R_F plotted for $L_{D,C60}$ ranging from 1Å to 100 nm.

We first consider a prototypical DBP/C_{60} SHJ device utilizing 10 nm of TPTPA as an anode blocking layer[31] to prevent quenching at the DBP/MoO_3 interface.[53,61] The entire structure for this device was (thicknesses in nm) Glass/150 ITO/5 MoO_3/10 TPTPA/10 DBP/36 C_{60}/10 BCP/100 Ag. To confirm that the TPTPA/DBP interface did not form a functional heterojunction, we fabricated a device with TPTPA and DBP as the only active layers (**Figure 4.5**). This device exhibited negligible photocurrent, corroborating our assumption that TPTPA is an effective blocking layer for DBP. The measured energy levels of DBP and TPTPA are also very similar.[90] However, as seen by the overlap in emission between TPTPA and DBP (**Figure 4.2**), TPTPA has a finite Förster radius into DBP, which means that TPTPA will transfer excitons into DBP. Since we were unable to measure either the L_D or R_F for TPTPA (and could not find consistent measured values for $L_{D,TPTPA}$ in literature) for all devices employing TPTPA, we accounted for this energy transfer in any modeling by varying the TPTPA IQE until the spectrum from 400 nm – 500 nm fit the measured EQE.

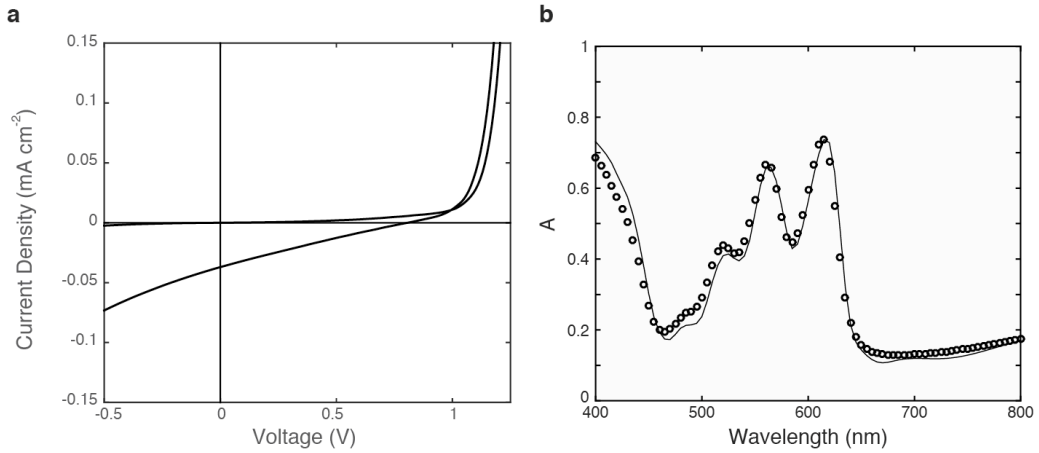

Figure 4.5 Negligible photocurrent from an ITO/MoO_3/TPTPA/DBP/BCP/Ag device stack. Since the photocurrent is two orders of magnitude lower than expected, we can treat the TPTPA/DBP interface as perfectly exciton blocking for all devices in this study.

The *J-V* performance of the device is similar to what has been shown in the literature (FF = 70% FF and V_{oc} = 0.89 V).[31] Using fitted L_D values for DBP (8 nm) and C_{60} (17 nm) as well as $R_{F,DBP:C60}$ (1.5 nm), we obtain a very close agreement between modeled and measured EQE spectra (**Figure 4.4b**). The external quantum efficiency of the device improves slightly due to transfer of excitons from the DBP layer (with an inherent η_{Diff} = 68%) into the C_{60} layer (which saturates at a higher η_{Diff} = 89%). The reason for the improvement in overall η_{Diff} of excitons generated in the DBP layer is clarified further in **Figure 4.4c**, where all of the major loss and collection mechanisms are plotted. Since changing R_F has no effect on the optical fields (or absorbed power) in the device, we can attribute this improvement in EQE to an increase in η_{Diff} of excitons initially generated in the DBP (FD) layer. For $R_{F,DBP:C60}$ = 0, 68% of excitons generated in the DBP reach the heterojunction from the DBP side (solid blue line) and 32% recombine in the bulk of the DBP layer (dotted blue line). As $R_{F,DBP:C60}$ increases, excitons generated in the DBP (FD) begin to transfer into the C_{60} (FA) layer. Excitons transferred into the C_{60} layer will either reach the heterojunction from the C_{60} side (solid red line) or recombine in the bulk of the C_{60} (dotted red line).

In the case where $R_{F,DBP:C60}$ is large (>~5nm), flux to the heterojunction and bulk recombination of excitons within the DBP layer go to zero, and flux to the heterojunction and bulk recombination of excitons occur solely in the FA layer. However, in the intermediate regime of R_F values, the rate at which each mechanism increases or decreases determines the overall η_{Diff}. For example, as $R_{F,DBP:C60}$ increases from 0 nm to 1 nm, the effective diffusivity of excitons in the DBP (FD) near the heterojunction drops precipitously, quickly reducing the flux of excitons reaching the heterojunction from the FD side. This effect is illustrated in **Figure 4.1g**, where we see the slope of the exciton population density become nearly zero (i.e. horizontal) at the heterojunction for $R_F \geq 4$ nm. However, while the flux of excitons at the HJ drops to zero, there is still a finite exciton population density within the layer furthest from the heterojunction. Due to the decreased diffusivity near the HJ, these excitons will recombine within the bulk of the FD before reaching the HJ or transferring into the FA.

Figure 4.4d shows that the η_{Diff} at which the device saturates (for large R_F) is highly dependent on the diffusion efficiency of the FA. We show this in **Figure 4.4c** by varying $L_{D,C60}$ from 1 Å to 100 nm. In the case of a FA with very low L_D (e.g. $L_{D,C60}$ = 0.1 Å), η_{Diff} in the compensation regime will never saturate higher than $\eta_{Diff,FD}$ if FRET were not occurring (i.e. $L_{D,DBP:C60}$ = 0). However, if $\eta_{Diff,FA}$ is sufficiently high (e.g. $L_{D,C60}$ = 100 nm), then η_{Diff} can saturate at 100% for large enough R_F (in **Figure 4.4d**, this occurs for $R_{F,DBP:C60}$ >~4 nm). This is because for large R_F values, 100% of the excitons are transferred out of the FD layer, so there is no bulk recombination in the FD. Thus the L_D of the FA is of crucial importance to maximizing η_{Diff} when FRET is occurring.

From **Figure 4.4c**, we can conclude that η_{Diff} can be maximized in one of two ways. First, if L_D of the FD is intrinsically high and the L_D of the FA is intrinsically low, then the best course

of action may be to lower R_F as much as possible to retain the FD's inherently high η_{Diff}. For FD materials with intrinsically low L_D, the best way to maximize efficiency would be by maximizing R_F and ensuring that η_{Diff} of the FA is high.

On a more practical note, fitting of exciton diffusion lengths with models that do not include the FRET process can lead to inaccurate values. In the case of the DBP/C_{60} SHJ, not considering FRET gives a fitted $L_{D,DBP}$ = 10.5 nm. However, if transfer of excitons into C_{60} is accounted for, the fitted $L_{D,DBP}$ = 8 nm. In this case, $L_{D,DBP}$ is overestimated, for similar reasons to those presented by Luhman *et al* when measuring L_D *via* PL measurements. However, as noted previously, if the L_D of the Förster acceptor is very low, a model not including FRET could also *underestimate* the diffusion length of the Förster donor.

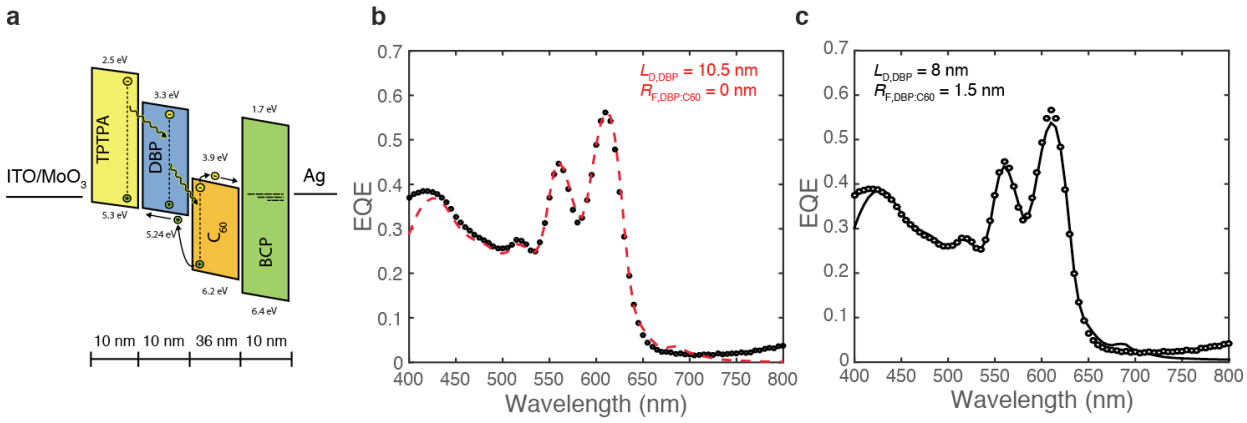

Figure 4.6 a) Energy band diagram of DBP/C_{60} SHJ device with TPTPA sensitizer and anode exciton blocking layer. Modeled EQE fits b) without considering FRET and c) considering FRET. If energy transfer from the DBP into the C_{60} layer is not taken into account, the fitted diffusion length increases from 8 nm (in agreement with L_D measured via PL) to 10.5 nm.

4.3.6 FRET in Multi-junction CHJ Devices

As determined in the previous section, if $\eta_{Diff,FA}$ is sufficiently high, it can be beneficial to efficiently transfer excitons from the FD into the FA. Due to the absorption spectra of C_{60}, however, R_F will always be limited for active layers that absorb in the green and emit in the red. Indeed, other common exciton donor layers have been reported with similar Förster radii for

transfer into C_{60}. [47,81] In an attempt to increase the amount of interlayer energy transfer within the devices, we replaced the C_{60} exciton acceptor with Cl_6SubPc, an exciton acceptor that has previously exhibited low photoconductivity and higher V_{oc} in combination with SubPc[91] and SubNc[80] exciton donors. Since SubNc absorbs strongly in the red (peak at 700 nm), it is also an ideal candidate to be a Förster acceptor for DBP and Cl_6SubPc, as both materials emit in that region of the spectrum (**Figure 4.2b**). Thus, our proposed devices in this study consisted of ITO/MoO_3/TPTPA/DBP/SubNc/Cl_6SubPc/ BCP/Ag. In that structure, TPTPA acts as an exciton blocking layer and FD to DBP; DBP acts as a FA to TPTPA, an electron donor to SubNc, and a FD to SubNc; SubNc acts as an ambipolar interlayer and FA to DBP and Cl_6SubPc; and Cl_6SubPc acts as an electron acceptor and FD to SubNc.

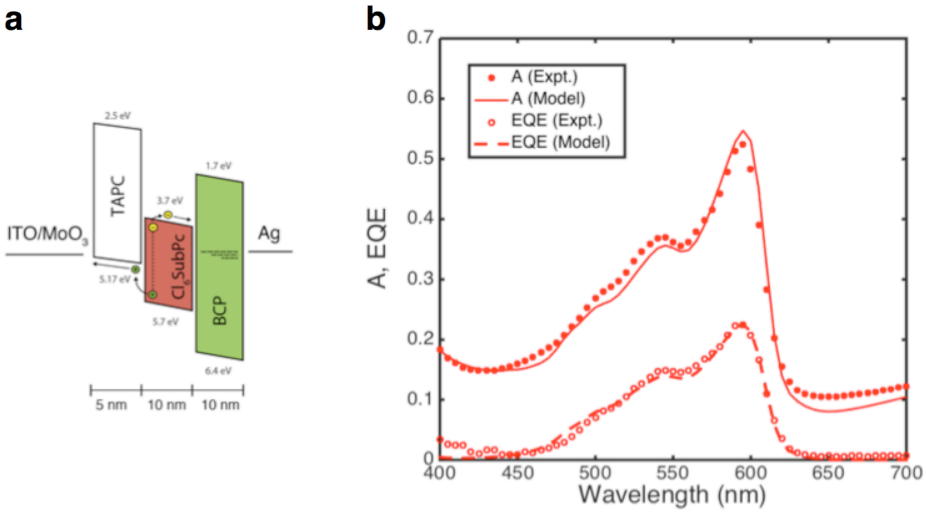

Figure 4.7 a) Energy band diagram and b) measured and modeled absorption and EQE spectra for a TAPC/Cl_6SubPc SHJ device. L_D for Cl_6SubPc was fit to be 4.5 nm and that value is used throughout this chapter.

For clarity of modeling, we begin with the simpler device configuration of (thicknesses in nm) ITO/5 MoO_3/5 TAPC/13 SubNc/x Cl_6SubPc/10 BCP/100 Ag, fabricated devices with Cl_6SubPc thicknesses of 10 nm, 20 nm, and 30 nm. In these devices, TAPC acts as a transparent exciton dissociation layer (EDL),[61,90] such that while there are two active heterojunctions in the device, there are only 2 absorbing layers (SubNc and Cl_6SubPc). The diffusion length of

Cl_6SubPc fit to be 4.5 nm in a TAPC/Cl_6SubPc SHJ device. Because the diffusion length of Cl_6SubPc is relatively low, even for the device with the thinnest (10 nm) Cl_6SubPc layer, its predicted η_{Diff} for R_F = 0 is 46%. Because the R_F is 4 nm, η_{Diff} is significantly improved for all layer thicknesses, with a demonstrated 300% improvement η_{Diff} for the 30 nm device. Because the L_D of Cl_6SubPc is low to begin with, and η_{Diff} of the SubNc layer is higher than that of the Cl_6SubPc layer, we are able to effectively stretch the absorption/diffusion limit for the Cl_6SubPc layers in these devices. In **Figure 4.10**, we show what happens if the TAPC/SubNc/Cl_6SubPc CHJ is converted to a SubNc/Cl_6SubPc SHJ. By removing the TAPC layer and changing the boundary condition at the anode from exciton dissociating to exciton quenching, η_{Diff} of the SubNc layer is reduced, resulting in a clearly reduced η_{Diff} of the Cl_6SubPc layer as well.

For the next device set, we kept the Cl_6SubPc layer thickness constant at 10 nm and introduced layers of 10 nm TPTPA and *x* nm DBP in place of the TAPC EDL layer. The DBP layer was then varied for 10 nm, 20 nm, and 30 nm. Here again, the TPTPA layer acted as an exciton blocking layer and FD to DBP. As with the Cl_6SubPc CHJ devices, $\eta_{Diff,SubNc}$ was greater than $\eta_{Diff,DBP}$, leading to a significant increase in the overall η_{Diff}. Energy level diagrams, fitted absorption curves, and *J-V* curves for all CHJ devices can be found in **Figure 4.9** and device performance parameters for all devices are provided in **Table 4.2**.

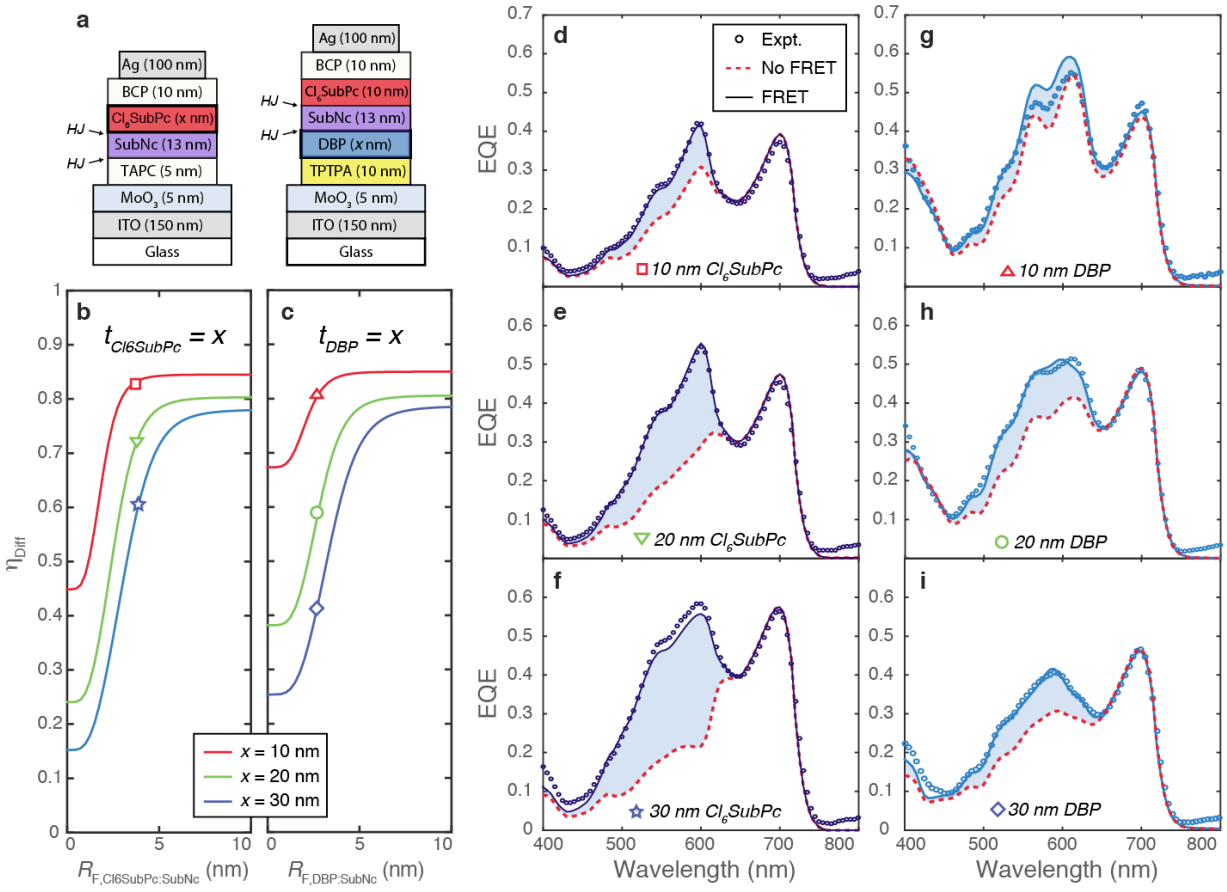

Figure 4.8 The effect of Förster transfer in multi-junction CHJ OPVs. a) Schematic device structures for the two types of CHJs used in this study. Predicted η_{Diff} for excitons generated in the b) Cl_6SubPc and c) DBP layers as a function of R_F and layer thickness. d-f) Measured and modeled EQE spectra for TAPC/SubNc/Cl_6SubPc CHJ devices with 10 nm, 20 nm, and 30 nm thick Cl_6SubPc layers, respectively. g-i) The same for TPTPA/DBP/SubNc/Cl_6SubPc devices with 10 nm, 20 nm, and 30 nm thick DBP layers, respectively. In all EQE plots, experimental data is plotted with open circles, and modeled EQE curves are represented with solid lines (considering FRET) and dotted red lines (not accounting for FRET).

We note that for all CHJ devices, the thicknesses of the Cl_6SubPc and DBP layers (up to 30 nm) had a negligible effect on FF and V_{oc}, as both were relatively constant at ~67% and ~0.98 V, respectively. We attribute the consistency of device performance to high mobility active layers. Since neither V_{oc} or FF were a function of active layer thickness within the 10-30 nm range, we were able to optimize the PCE of the device further by only optimizing J_{sc}, as will be discussed in the next section.

Table 4.2 *J-V* Performance parameters for all devices fabricated in this study. All *J-V* parameters were averaged over at least six devices on the same substrate and a spectral mismatch factor was used explicitly in calculating J_{sc} and PCE.

Device	V_{oc} (V)	J_{sc} (mA cm^{-2})	FF (%)	PCE (%)
TPTPA/DBP (No HJ)	0.58	0.04	23.0	0.00
SHJs				
TPTPA/DBP/C_{60}	0.89	6.01	70.0	3.74
TAPC/Cl_6SubPc	0.82	1.94	53.8	0.86
SubNc/Cl_6SubPc	0.89	4.07	68.1	2.47
CHJs				
TAPC/SubNc/10 Cl_6SubPc	0.97	6.24	67.7	4.10
TAPC/SubNc/20 Cl_6SubPc	0.97	7.76	66.3	4.92
TAPC/SubNc/30 Cl_6SubPc	0.98	9.06	65.6	5.84
TPTPA/10 DBP/SubNc/Cl_6SubPc	0.98	9.11	67.2	6.00
TPTPA/20 DBP/SubNc/Cl_6SubPc	0.97	9.21	66.8	6.00
TPTPA/30 DBP/SubNc/Cl_6SubPc	0.98	7.36	68.1	4.92
TPTPA/14 DBP/11 SubNc/ 28 Cl_6SubPc/BCP	0.98	9.69	67.6	6.55
TPTPA/14 DBP/11 SubNc/ 28 Cl_6SubPc/Bphen	0.99	9.65	75.7	7.25

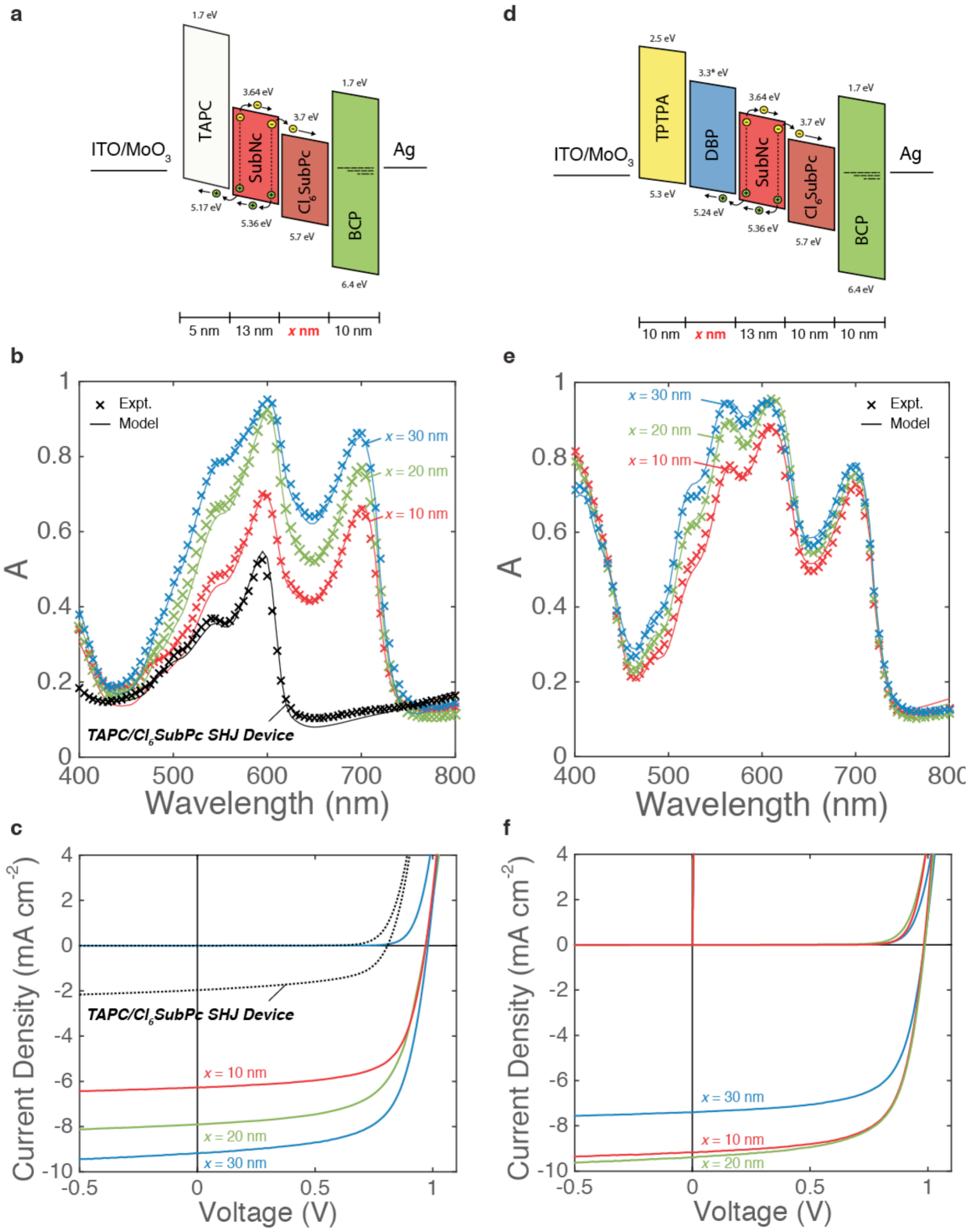

Figure 4.9 Energy level diagrams, model fits to absorption, and *J-V* curves for a-c) TAPC/SubNc/Cl_6SubPc CHJs and d-f) TPTPA/DBP/SubNc/Cl_6SubPc CHJs.

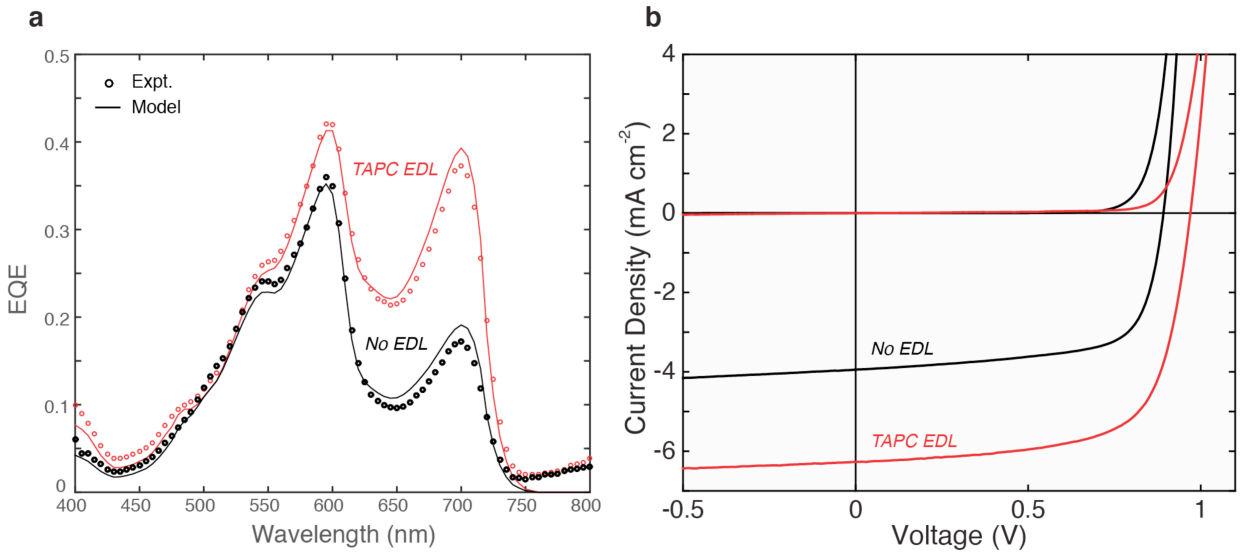

Figure 4.10 a) EQE and b) *J-V* curves for ITO/MoO_3/*TAPC (EDL)*/SubNc/Cl_6SubPc/BCP/Ag devices with (red) and without (black) the TAPC EDL at the anode. By removing the TAPC, the boundary condition of SubNc changes from exciton dissociating (at the TAPC) to exciton quenching (at the MoO_3). This drop in EQE also results in a drop in the Cl_6SubPc EQE due to transfer of excitons from the Cl_6SubPc into the SubNc layer.

4.3.7 Champion CHJ Devices

Using the model established in previous sections, we predicted the EQE of TPTPA/DBP/SubNc/Cl_6SubPc devices for every combination of reasonable active layer thicknesses (5 nm-30 nm for any individual layer). Since the FF and V_{oc} were consistent within error across all CHJ devices, the assumption was that an optimized EQE would also produce a device with optimized power conversion efficiency. The model predicted best performance for ITO/5 MoO3/10 TPTPA/14 DBP/11 SubNc/28 Cl_6SubPc/10 BCP/100 Ag. The SubNc thickness was decreased from 13 nm in the previous devices to 11 nm in the optimized to improve its η_{Diff}, which in turn improved the η_{Diff} of excitons transferring into the SubNc from both the DBP and Cl_6SubPc layers. As seen from **Figure 4.11a**, the modeled and experimentally determined EQEs matched very closely, so we conclude that this is indeed the optimized EQE for a device structure containing these materials. To theoretically improve this device further, $R_{F,DBP:SubNc}$ and $R_{F,Cl6SubPc:SubNc}$ should be increased, and the L_D of SubNc should be maximized. As BCP and

Bphen have nearly identical optical properties (refractive index values for each are provided in the Supplemental Information), and Verreet *et al.* previously showed that the cathode buffer layer has a significant impact on the FF of devices containing Cl_6SubPc,[80] we fabricated the optimized device structure with both 10 nm of BCP and Bphen. The devices with BCP exhibited FF and V_{oc} similar to the previous CHJs, but the FF and V_{oc} improved to 75.6% and 0.99 V, respectively. Since the J_{sc} and EQE were identical to within error for devices employing BCP and Bphen, the power conversion efficiency of the optimized Bphen device was 7.3%.

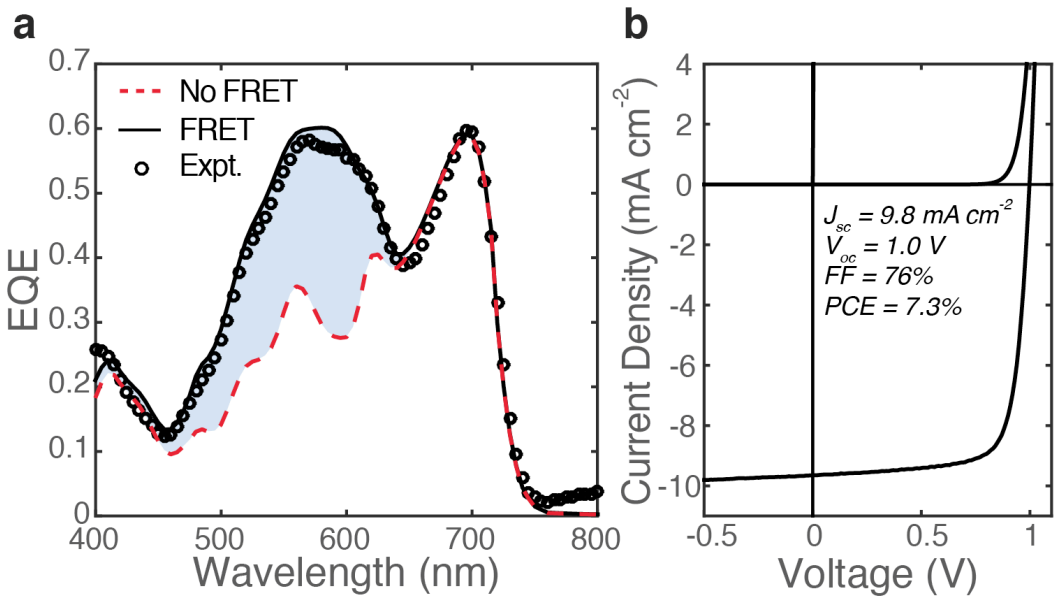

Figure 4.11 a) Experimentally determined absorption and EQE spectra of optimized devices utilizing FRET. Symbols represent experimental data. The solid line denotes the model fit accounting for FRET and the red dashed line corresponds to model predictions not considering FRET in the device. b) *J-V* curve of optimized device with Bphen cathode EBL. While the EBL had no apparent effect on the EQE or J_{sc}, switching from BCP to Bphen resulted in a substantial increase in the FF of the device.

4.4 Conclusions

In conclusion, we have developed a rigorous model for predicting and optimizing the performance of OPVs where Förster resonant energy transfer is present. In devices that exhibit FRET, we have shown that excitons transferred out of a Förster donor do not automatically contribute to photocurrent. Instead, how efficiently they are converted to photocurrent depends

dramatically on the diffusion efficiency of the Förster acceptor (specifically the diffusion length of the FA). To optimize OPVs, a judicious pairing of active layer materials must be used to maximize R_F for intrinsically low L_D Förster donors and maximize L_D of any Förster acceptor to achieve optimal η_{Diff}. Critically, intrinsic materials properties such as L_D are shown here to be potentially poor predictors of device performance on their own, and the photoluminescence methods traditionally used to characterize materials can be misleading in regard to the impact of Förster transfer on devices. Our results should provide the groundwork for new materials and devices to drive OPVs to their fundamental efficiency limit and help circumvent the diffusion bottleneck in organic semiconductors.

Chapter 5
Conclusions and Future Work

5.1 Conclusions

In this thesis, we have demonstrated progress in the field of organic photovoltaics by developing a better understanding of exciton diffusion and energy transfer within planar devices. In Chapter 2, we demonstrated the exciton quenching properties of MoO_3, a commonly used anode buffer layer, and proposed a new type of buffer layer termed an exciton dissociation layer. The EDL was thin (5 nm), transparent in the visible spectrum, and placed between the MoO_3 anode and the donor so excitons generated in the donor could not reach the quenching interface. Furthermore, the HOMO level of the EDL was chosen such that it was offset from that of the donor layer, creating a second heterojunction at the EDL/donor interface and reducing bulk recombination of excitons generated within the donor. Based on EQE measurements and material properties established in the literature, we adapted the EQE model from Chapter 1 to account for photocurrent generation from multiple heterojunctions within the cascade heterojunction devices. Using this system, we demonstrated a 66% improvement in the external and internal quantum efficiencies of the SubPc layer (and a 27% improvement in overall J_{sc}). However, due to the onset of s-kink behavior in the devices (and concomitant drop in FF), the PCE remained constant.

In Chapter 3 we performed a combinatorial study with twelve different EDL materials with HOMO levels ranging from ~4.9 eV-5.5 eV. In the case of all studied devices, the V_{MPP} of the CHJ was never higher than the V_{MPP} of the estimated V_{MPP} of its constituent subjunctions (approximated by measuring SHJ devices corresponding to each). Furthermore, we demonstrated an apparent trend between the HOMO offset (ΔE_{HOMO}) at the EDL/interlayer interface and the V_{MPP} of the CHJ devices, consistent with previous findings by Tress *et al*.[63] For ΔE_{HOMO} > ~0.2eV, the V_{MPP} of the CHJ linearly decreased below the minimum V_{MPP} of either subjunction. By matching the V_{MPP} of both subjunctions and keeping ΔE_{HOMO} < 0.2 eV, we were able to demonstrate a 46% improvement in PCE by converting a SubNc/C_{60} SHJ to a TAPC/SubNc/C_{60} CHJ device.

In Chapter 4, we further modified our EQE model to fully account for interlayer Förster resonant energy transfer of excitons in OPVs. While other studies provided the necessary groundwork by accounting for the transfer of excitons out of FD layers in OPVs (especially the work by Luhman *et al*., and Griffith *et al*.),[37,47] we believe this to be the first model to track exciton diffusion within the FA until the excitons either reach a heterojunction or recombine (in the bulk or at a quenching interface). With the model, we showed that the L_D and η_{Diff} of the Förster acceptor is crucial in determining the overall diffusion efficiency of any OPV device. If the L_D of the FA layer is low, then transfer of excitons into the FA can actually be a parasitic process. However, if the L_D of the FA layer is high enough, then FRET can be used to stretch the absorption/diffusion tradeoff by funneling excitons from FD layers into the FA over distances much longer (demonstrated up to 30 nm) than their inherent diffusion lengths (<10 nm). By using a CHJ configuration and transferring generated excitons from DBP and Cl_6SubPc into a

high IQE SubNc layer, we are able to demonstrate a 93% improvement in PCE over the highest performing SHJ device.

5.2 Future Work

5.2.1 Photoluminescence Measurements of L_D and R_F

Due to unavailable equipment, we were unable to verify our diffusion length and Förster radii fits in Chapter 4. When that equipment becomes available, we suggest performing the necessary measurements (described well by Luhman *et al.*[47]) to check that all fitting parameters were correct.

5.2.2 Series Tandem Configurations

CHJ devices are promising candidates for use in series connected tandems, due to the flexibility in determining the spectral coverage for each subcell. The absorption/diffusion tradeoff can be stretched in each subcell without broadening spectral coverage, either by utilizing transparent EDLs (such as TAPC in Chapter 3) or by using multiple active layers with overlapping absorption peaks (such as DBP and Cl_6SubPc in Chapter 4). Then, combining subcells with complementary absorption peaks could be used to broaden spectral coverage and further mitigate the absorption/diffusion bottleneck. For example, in the case of the optimized devices in Chapter 4, there is no absorption within the blue part of the spectrum or the NIR (beyond ~750 nm). A potentially complementary subcell would be a lead phthalocyanine (PbPc)/C_{60} or PbPc/C_{70} device, which absorbs strongly in both the blue and NIR.[92]

5.2.3 Judicious Material Selection and Design for FRET in CHJ Devices

While we were able to demonstrate a 93% improvement in PCE in Chapter 4 by utilizing FRET in ITO/TPTPA/DBP/SubNc/Cl_6SubPc/Bphen/Ag CHJs, the materials employed were less than

ideal for constructing an optimized device. Using the FRET design rules coupled with those established in Chapter 3, we suggest material selection and design that minimizes charge injection barriers and maximizes the diffusion efficiency of the interlayer/Förster acceptor.

A strong blue absorber could also be added to the device to broaden spectral coverage. For optimal absorption with the device, the blue absorber would be placed between the Cl_6SubPc and Bphen blocking layer (i.e. closest to the back reflector for maximum absorption at the shorter wavelengths). To prevent any additional injection barriers in the device, the blue absorber could have a LUMO level aligned with that of Cl_6SubPc and act only as a sensitizer, transferring excitons into the Cl_6SubPc layer (which would then be funneled into the SubNc interlayer). Furthermore, as noted by Equation (4.2), the Förster radii of all active layers could be improved *via* increased η_{PL}, further increasing how far the absorption/diffusion bottleneck could be stretched. Lastly, since a large majority of excitons are transferred into the SubNc layer, it would be ideal to either improve the L_D of SubNc or find a replacement FA with higher L_D and similar absorption spectrum.

5.2.4 J-V Model for CHJ Devices

While we presented a circuit diagram in **Figure 3.3a** that was helpful in qualitatively discussing CHJ device operation, we note that it provided a more simplified description than what is actually occuring within CHJ devices (especially those that exhibit strong s-kink behavior). First, as discussed in Section 3.3.3, we expect that due to asymmetric injection barriers and charge mobilities within the layers, the diode (and dark current) properties of the device are determined by preferential recombination of injected charges at a single interface. Second, as shown in **Figure 3.5c** and **Figure 3.5g**, the photocurrent contributions from one or both subjunctions shut off at applied biases below V_{oc} due to a sharp decrease in η_{CC} from a drop in the built-in field

within the device. We thus conclude that accounting for injected and photogenerated charges (and any buildup) within the device will be crucial in predicting dark current and the voltage dependence of the photocurrent production at each heterojunction.

Therefore, we propose an adapted version of the free charge drift-diffusion simulations detailed in the work by Tress *et al*.[63] to include modifications for photocurrent generation at multiple interfaces and additional spatially-distributed free charge generation throughout the absorbing active layers due to autoionization of excitons in the bulk (i.e. contributions from photoconductivity). To account for photocurrent generation, the flux of excitons to each heterojunction would be calculated using the EQE model detailed in Section 1.7 and coupled to the OB model to determine η_{CC}.

Appendix A EQE Code

```
function [output] = OPV_Back(stack, tvar, mvar, phi0, polarization,subcell_Jmpp_Jsc,
LibSave);
%%%%%%%%%%%%%%%%%%%%%%%%%%%%%%%%%%%%%%%%%%%%%%%%%%%%%%%%%%%%%%%%%%%%%%%%%%%%%%%%
%
% This method follows that developed in Pettersson JAP 1999, with
% modifications to account for:
%
% Incoherent front (usually glass) substrate (Centurioni 2005)
% Forster transfer out of ED to EA (Holmes 2011 DOI:10.1002/adfm.201001928)
% Forster transfer from ED into EA (Barito)
%
% Two corrections needed in Petterson, reflectivity term and equation 4,
% from Snell's law
%%%%%%%%%%%%%%%%%%%%%%%%%%%%%%%%%%%%%%%%%%%%%%%%%%%%%%%%%%%%%%%%%%%%%%%%%%%%%%%%

clc
% stack='BITC_DBPSHJ.txt';
% phi0 = 0; %angle of incidence in degrees
% polarization = 'TE'; %TM or TE
% subcell_Jmpp_Jsc = 1;%[.82,.85]; %Jmpp/Jsc for subcell 1,2,etc. (for matching Jmpp
in tandems) - separate by commas
% tvar=[];
% mvar={;

output = struct;
%% Constants
global c eta0 h qe dz
c = 3*10^8;        % speed of light m/s
h = 6.626E-34;     % plank constant joule-s
qe = 1.602E-19;    % electron charge C/electron
eta0 = 8.854E-12;  % free permativity (C^2)/(N m^2)= F/m = As/Vm
dz = 0.005*1E-9;   % mesh size for field distribution and Finite Difference Method
(meters)
dz_F = dz - 0.00000000001*1e-9;%0.99999*dz;
%% Compile stack properties from input%%
% read stack file only once
fid = fopen(char(stack),'r');
scan = textscan(fid, '%s %f %s');
fclose(fid);
% build stack properties
```

```
[t, film, ref, D, tau, eta_cc, ED, EA, active_priority, rho, R_F, G_Abs_Off] =
StackBuild(scan, tvar, mvar);
t_top_substrate = t(2); %Used in TMM calculation for power transmitted through glass
substrate
t(2) = 0;   %Resets substrate thickness to zero to eliminate time needed to calculate
E field in thick substrate
%% Set wavelengths to loop through
s = size(t, 1)-2;       % total number of films in the stack

%spectrum data
lambda0 = 400;          % initial wavelength (nm)
dlambda = 5;            % wavelength stepping size (nm)
lambdaf = 800;          % final wavelength
lambda_s = lambda0:dlambda:lambdaf;
M = size(lambda_s, 2);  % number of steps or data points of wavelength

lambda_sm = (lambda_s)*10^-9;  % meters

ref = ref(:,((lambda0-305)/dlambda+1):((lambdaf-305)/dlambda)+1); %put in GUI

%% Pre-allocate variables
T = zeros(1,M);
R = zeros(1,M);
IglassITOp = zeros(1,M);
A_tot = zeros(1,M);

zend = round(sum(t(1:end-1))/dz);
EE = zeros(zend, M);
G_Abs = zeros(zend, M);
G_F   = zeros(zend,M);
k_F   = zeros(zend,M);
Q = zeros(zend,M);
EQESp = zeros(s+1,M);  % EQE per layer per wavelength
EQE_G_Sp = zeros(s+1,M);
EQESp_pc = zeros(s+1,M);
EQESp_hj = zeros(s+1,M);
EQE = zeros(1,M);
EQE_G = zeros(1,M);
flux_hj = zeros(s+1, M);
flux_pop = zeros(s+1,M);
G_Abs_tot = zeros(s+1,M);
G_F_tot = zeros(s+1,M);
k_F_tot = zeros(s+1,M);
recomb_tot = zeros(s+1,M);
pp = zeros(zend,M);
a = zeros(round(max(t(2:s+1))/dz),s+1);
tauv = zeros(round(max(t(2:s+1))/dz),s+1);
d = zeros(round(max(t(2:s+1))/dz),s+1);
%% Wavelength Loop
for bb = 1:M %bb is counter for wavelength until endpoint M
    tt = zeros(1,zend);

    % lambda is wavelength over which you are currently calculating (m)
```

```
    lambda = lambda_sm(bb);
    n = ref(:, bb);         % refractive index vector for stack at lambda
    q = (n.^2 - n(1)^2*sin(phi0*pi/180)).^0.5;
    xi = q.*(2*pi/lambda);

    %% Transfer Matrix Model Calculation %%
    %%%%%%%%%%%%%%%%%%%%%%%%%%%%%%%%%%%%%%%%%%%%%%%%%%%%%%%%%%%%%%%%%%%%%%%

    % inputs
    % n:        refractive index for given wavelength, lambda
    % q:        propagation factor (angle dependent)
    % xi:       phase change wave experiences as it traverses the film
    % t:        thickness of each film
    % lambda:   wavelength currently under investigation, numerically

    % returns
    % tpp:      forward propagating transmission coefficient (p-polarized)
    % tmp:      reverse propagating transmission coefficient (p-polarized)

    [tp,tm,T(bb),R(bb),IglassITO(bb),A_tot(bb)] = TMM(n, q, xi, t, t_top_substrate,
lambda, polarization,phi0); %IglassITOp(bb)

    %% Calculate EE (electric field), Q (time avg'd abs.), and G (exc. gen. rate) for
each layer%%

    priority = 1;
    layer_priority = active_priority;

    while min(layer_priority) <100 %if satisfied, there are still active layers left
to consider

        if min(layer_priority) > priority
            priority = priority + 1;
        end

        for x = 2:s+1         % stack layer index

            dend(x) = round(t(x)/dz); %total number of points in film
            for y = 1:dend(x)     %layer segment index

                z = round(sum(t(1:x-1))/dz+y); %mesh point within entire stack
                tt(z) = sum(t(1:x-1))+y*dz;    %depth within device stack (including
glass)

                E = (tp(x)*exp(1i*xi(x)*y*dz) + tm(x)*exp(-
1i*xi(x)*y*dz))*(q(x)/n(x));
                EE(z, bb) = IglassITO(bb)*abs(E)^2;

                % time averaged absorbed power versus mesh point in stack
                Q = ((4*pi*c*eta0*imag(n(x))*real(n(x)))/(2*lambda))*EE(z, bb);
                G_Abs(z, bb) = (lambda/(h*c))*Q;  %exciton generation rate from E-
Field
```

```
            end

            %% FD-ODE calculations %%
            %%%%%%%%%%%%%%%%%%%%%%%%%%

            if layer_priority(x) == priority;

                d(x,1:dend(x)) = dz*(1:dend(x)); %depth vector within layer in meters

                % define vectors for exc gen, lifetime, and diff length

                G_Absv = G_Abs(round(sum(t(1:x-1))/dz+1):round(sum(t(1:x))/dz), bb);
                if G_Abs_Off(x) == 1 %If G_Abs_Off = 1, the
                    G_Absv = G_Absv.*0;
                end
                tauv(1:dend(x),x)=ones(dend(x),1)*tau(x);

                %% Calculate k_F (Forster transfer rate) for EDs %%
                k_Fv = zeros(dend(x),1); %initialize k_F vector

                if ED(x) == 1 %this layer is an exciton donor (ED) through Forster
transfer

                    for y = 2:s+1 %stack layer index (looking for EA's)

                        if EA(y) == 1 %then that layer is an exciton acceptor (EA)

                            t_EA = t(y); %thickness of EA
                            t_ED = ones(dend(x),1)*t(x); %vector of thicknesses of ED
layer for use in calculations below

                            %ED is on left of and/or above EA
                            if y > x
                                %calculate distance between ED and EA (if there are
layers inbetween)
                                t_int = -t(y);
                                for z = x+1:y
                                    t_int = t_int + t(z);
                                end

                                d_EA = t_ED - d(x,1:dend(x))' + t_int;% +
dz/10000;%vector of distances from points in ED to start of EA
                                d_EA = flipud(d_EA); %there's obviously a way to do
this without flipping. I just can't think that way right now
                                k_Fv = k_Fv +
(pi*rho(y)*R_F(x,y)^6)/12/dz.*(tauv(1:dend(x),x).^-1) .* ((d_EA+dz-dz_F).^-2 -
(d_EA+dz).^-2 + (d_EA+dz+t_EA).^-2 - (d_EA+dz-dz_F + t_EA).^-2);
                                k_Fv = flipud(k_Fv);
                            %ED is on right of and/or below EA
                            elseif y < x

                                %calculate distance between ED and EA (if there are
```

```
layers inbetween)
                                t_int = -t(y);
                                for z = y:x-1
                                    t_int = t_int + t(z);
                                end

                                d_EA = d(x,1:dend(x))' + t_int;% + dz/10000;
                                k_Fv = k_Fv +
(pi*rho(y)*R_F(x,y)^6)/12/dz.*(tauv(1:dend(x),x).^-1) .* ((d_EA-dz_F).^-2 - (d_EA).^-
2 + (d_EA + t_EA).^-2 - (d_EA-dz_F + t_EA).^-2);
                            end

%                             k_Fv = k_Fv +
(pi*rho(y)*R_F(x,y)^6)/6.*(tauv(1:dend(x),x).^-1) .* (d_EA.^-3 - ((d_EA + t_EA).^-
3));

                        end

                        for nn = 1:dend(x)
                            z = round(sum(t(1:x-1))/dz+nn); %mesh point within entire
stack
                            k_F(z,bb) = k_Fv(nn);
                        end
                    end
                end

                %% Calculate G_F (Forster generation rate) for EAs %%
                G_Fv = zeros(dend(x),1);

                if EA(x) == 1 %layer is an exciton acceptor

                    t_EA = t(x); %thickness of EA

                    for y = 2:s+1 %check for ED's
                        if ED(y) == 1 % then that layer is an exciton donor (FRET)

                            %EA is on left of and/or above ED
                            if y > x

                                %calculate distance between point in EA and ED (if
there are layers inbetween)
                                t_int = -t(x+1);
                                for z = x+1:y
                                    t_int = t_int + t(z);
                                end

                                d_ED = t_EA - d(x,1:dend(x))' + t_int;% + dz;%vector
of distances from point in EA to start of ED

                                for  nn=1:dend(x)
                                    d_pp = (d_ED(nn) + d(y,1:dend(y)))';
                                    %G_Fv(nn) = G_Fv(nn) + ((pi*rho(x)*R_F(y,x)^6)/2)
```

```
.* sum(dz.*p(1:dend(y),y).*(d_pp.^-4).*(tauv(1:dend(y),y).^-1));
                                    G_Fv(nn) = G_Fv(nn) + ((pi*rho(x)*R_F(y,x)^6)/12)
.* sum(1/dz.*p(1:dend(y),y).*(tauv(1:dend(y),y).^-1).*((d_pp-dz_F).^-2 - (d_pp).^-2 +
(d_pp + dz).^-2 - (d_pp-dz_F + dz).^-2));

                                    z = round(sum(t(1:x-1))/dz+nn); %mesh point
within entire stack
                                    G_F(z,bb) = G_Fv(nn); %Forster generation rate
within entire stack
                                end

                            %EA is on right of and/or below ED
                            elseif y < x

                                %calculate distance between point in EA and ED (if
there are layers inbetween)
                                t_int = -t(y);
                                for z = y:x-1
                                    t_int = t_int + t(z);
                                end

                                d_ED = d(x,1:dend(x))' + t_int;

                                for  nn=1:dend(x)
                                    d_pp = (d_ED(nn) + t(y) - d(y,1:dend(y)))';
                                    %G_Fv(nn) = G_Fv(nn) + ((pi*rho(x)*R_F(y,x)^6)/2)
.* sum(dz.*p(1:dend(y),y).*(d_pp.^-4).*(tauv(1:dend(y),y).^-1));

                                    G_Fv(nn) = G_Fv(nn) + ((pi*rho(x)*R_F(y,x)^6)/12)
.* sum(1/dz.*p(1:dend(y),y).*(tauv(1:dend(y),y).^-1).*((d_pp-dz_F).^-2 - (d_pp).^-2 +
(d_pp + dz).^-2 - (d_pp-dz_F + dz).^-2));

                                    z = round(sum(t(1:x-1))/dz+nn); %mesh point
within entire stack
                                    G_F(z,bb) = G_Fv(nn); %Forster generation rate
within entire stack
                                end
                            end


                        end
                    end
                end

                %% determine boundary conditions and choose case
                ext = char(film{x, 2}); % read the layer identifier tag
                bc = regexprep(ext, 'active','','ignorecase');
                bc = strtok(bc,','); %remove extraneous info s.a. 'tvar1' or 'mvar'

                [p(1:dend(x),x), flux_hj(x, bb), flux_pop(x, bb), G_Abs_tot(x, bb)
G_F_tot(x,bb), k_F_tot(x,bb), recomb_tot(x,bb)] = DriftDiffusion(D(x),
tauv(1:dend(x),x), G_Absv, G_Fv, k_Fv, eta_cc(x), 0, d(x,1:dend(x)), bc);
```

```
                pp(round(sum(t(1:x-1))/dz)+(1:dend(x)), bb) = p(1:dend(x),x); % exc
population versus position

                layer_priority(x) = 100; %tag this active layer as finished
            end

            %% EQE Calculation For Each Wavelength %%
            %%%%%%%%%%%%%%%%%%%%%%%%%%%%%%%%%%%%%%%%

            Nph = 0.5*c*eta0/(h*c/lambda);  % photons/(m^2 s)
            Ne = abs(flux_hj(x, bb)); %electrons/(m^2 s) from HJ
            Ne_G = abs(G_Abs_tot(x,bb));

            EQESp(x, bb) = Ne/Nph;  % EQE per layer per wavelength
            EQE_G_Sp(x,bb) = Ne_G/Nph;

        end

        EQE(bb) = sum(EQESp(:,bb));
        EQE_G(bb) = sum(EQE_G_Sp(:,bb));

    end

end
%% Use EQE and AM1.5 spectrum to calculate device current
subcell_no = size(subcell_Jmpp_Jsc);subcell_no=subcell_no(2); %total # of subcells
subcell = 1;
J_subcell = zeros(1,subcell_no);
J_pc_subcell = zeros(1,subcell_no);
J_hj_subcell = zeros(1,subcell_no);
Jmpp_subcell =  zeros(1,subcell_no);
J_layer = zeros(1,s);
J_pc_layer = zeros(1,s);
J_hj_layer = zeros(1,s);
Jmpp_layer =  zeros(1,s);

if length(lambda_s) > 1 %only interpolate if more than one wavelength being
calculated over
    for x = 1:s
        J_pc_layer(x) = sum(qe*photonDens(lambda0:lambdaf).*interp1(lambda_s,
EQESp_pc(x,:), lambda0:lambdaf)/10); % mA/(cm^2)
        J_hj_layer(x) = sum(qe*photonDens(lambda0:lambdaf).*interp1(lambda_s,
EQESp_hj(x,:), lambda0:lambdaf)/10); % mA/(cm^2)
        J_layer(x) = sum(qe*photonDens(lambda0:lambdaf).*interp1(lambda_s,
EQESp(x,:), lambda0:lambdaf)/10); % mA/(cm^2)
        Jmpp_layer(x) = J_layer(x) * subcell_Jmpp_Jsc(subcell); %mA/cm^2

        J_pc_subcell(subcell) = J_pc_subcell(subcell)+J_pc_layer(x);
        J_hj_subcell(subcell) = J_hj_subcell(subcell)+J_hj_layer(x);
        J_subcell(subcell) = J_subcell(subcell)+J_layer(x);
        Jmpp_subcell(subcell) = Jmpp_subcell(subcell)+Jmpp_layer(x);
```

```
        if strfind(film{x,2},'rz')==1
            subcell = subcell+1;
            J_subcell(subcell) = 0;
            Jmpp_subcell(subcell) = 0;
        end
end
end
%% Device Property Outputs %%
%%%%%%%%%%%%%%%%%%%%%%%%%%%%%
% G_F_tot(6,1)
% k_F_tot(7,1)
% flux_hj(6,1)
% G_Abs_tot(7,1)
% k_F_tot(7,1)./G_F_tot(6,1)

G_F_tot(7,1)
k_F_tot(6,1)
flux_hj(7,1)
G_Abs_tot(7,1)
k_F_tot(6,1)./G_F_tot(7,1)


IQE_tot = EQE./A_tot;
A_active = EQE_G;
IQE_active = EQE./A_active;

% divide the current by the number of heterojunctions (series operation)
J = min(J_subcell);
Jmpp = min(Jmpp_subcell);

output.dz = dz;
output.t = t;
output.tt = tt;
output.pp = pp;
output.subcell = subcell;
output.J = J;
output.Jmpp = Jmpp;
output.J_layer = J_layer;
output.J_pc_layer = J_pc_layer;
output.J_hj_layer = J_hj_layer;
output.J_subcell = J_subcell;
output.J_pc_subcell = J_pc_subcell;
output.J_hj_subcell = J_hj_subcell;
output.Jmpp_subcell = Jmpp_subcell;
output.EE = EE;
output.EQE = EQE;
output.IQE_tot = IQE_tot;
output.IQE_active = IQE_active;
output.A_active = A_active;
output.Qp = Q;
output.G_Abs = G_Abs;
output.G_F = G_F;
```

```
output.k_F = k_F;

output.G_Abs_tot = G_Abs_tot;
output.G_F_tot = G_F_tot;
output.k_F_tot = k_F_tot;
output.recomb_tot = recomb_tot;
output.flux_hj = flux_hj;

output.R = R;
output.T = T;
output.A_tot = A_tot;
output.IglassITOp = IglassITOp;
output.wl = lambda_s; %put in GUI
end

%% Build a stack of material properties %%
function [t, film, ref, D, tau, eta_cc, ED, EA, active_priority, rho, R_F, G_Abs_Off]
= StackBuild(scan, tvar, mvar)
% build the thickness vector and refractive index array via internal
% function, StackBuild

% inputs %
% stack:        name of text file containing stack information
% tvar:         array containing new thickness for film with tvar tag in file
% mvar:         array containing new material for film with mvar tag in file

% returns %
% t:            array containing thickness of each layer
% t_top_substrate:  thickness of second layer in stack (should be either substrate or
air)
% film:         array containing name of each film
% dev:          number of devices (defined by recombination zones [for tandems])
% ref:          matrix of refractive index vs wavelength for each film
% Ld:           array containing exciton diffusion length for each film
% tau:          array containing exciton lifetime for each film

t = scan{2}*1E-9;
s = size(t,1);
ref = zeros(s,120);
D = zeros(1,s);
Ld = zeros(1,s);
tau = zeros(1,s);
eta_cc = zeros(1,s);
EA = zeros(1,s); %for tagging exciton acceptors later (Forster transfer)
ED = zeros(1,s); %for tagging exciton donors later (Forster transfer)
G_Abs_Off = zeros(1,s);
active_priority = zeros(1,s)+100; %initialize priority for considering active layers
rho = zeros(1,s); %molecular density of material in nm^-3
% buld refractive index matrix of stack from materials database
for x = 1:s
    mat = char(scan{1}(x));
    ext = char(scan{3}(x));
```

```
    if isfinite(strfind(ext,'var')) == 1
        N = str2double(ext(strfind(ext, 'var')+3:size(ext,2)));
        switch ext(strfind(ext, 'var')-1)
            case 't'
                t(x) = tvar(N)*1E-9;
                %disp([mat,' is now ',num2str(tvar(N)),' nm']);
            case 'm'
                mat = mvar{N};
                %disp(['layer ',num2str(x),' is now ',mat]);
        end
    end

    %set priority for considering active layers

    if isempty(strfind(lower(ext), 'active')) == 0
        active_priority(x) = 1;
    end

    if isempty(strfind(ext, 'ED')) == 0
        ED(x) = 1; %tag which active layers will have be an exciton donor for Forster
transfer
        active_priority(x) = 2;
    end

    if isempty(strfind(ext, 'EA')) == 0
        EA(x) = 1; %tag which active layers will have be an exciton acceptor for
Forster transfer
        active_priority(x) = 4;
        if isempty(strfind(lower(ext), 'abs_off')) ==0
            G_Abs_Off(x)= 1;
        end
    end

    if isempty(strfind(ext, 'ED,EA')) == 0
        active_priority(x) = 3;
    end

    if isempty(strfind(lower(ext), 'active')) == 1
        active_priority(x) = 100;
    end

    % Load values from materials.mat (e.g. Ldsubpc, not Ld.subpc)
    vars = {['n',mat], ['D',mat], ['Ld',mat], ['tau',mat], ['eta_cc',mat],
['rho',mat]};
    g = load('materials.mat', vars{:});
    ref(x,:) = g.(vars{1});
    D(x) = g.(vars{2});
    Ld(x) = g.(vars{3});
    tau(x) = g.(vars{4});
    eta_cc(x) = g.(vars{5});
    rho(x) = g.(vars{6});
```

```
    film{x, 1} = mat;
    film{x, 2} = ext;
end

%populate R_F (Forster radii)
R_F = zeros(s,s);
for x = 2:s
    if ED(x) == 1
        for y = 2:s
            if EA(y) == 1
                dat = load('materials.mat');
                R_F(x,y) = dat.(strcat('R_F',film{x,1},film{y,1}));
            end
        end
    end
end
clear(mat, 'g');

end
%% Transfer Matrix Method %%
function [tpp, tmp, Ti, Ri, IglassITOp, Ai] = TMM(n, q, xi, d, d_substrate, lambda,
polarization, phi0)
incov = @(S)[abs(S(1,1))^2    -abs(S(1,2))^2;   abs(S(2,1))^2   (abs(det(S))^2-
abs(S(1,2)*S(2,1))^2)/abs(S(1,1))^2];

layers = length(d);

% Initialize variables
phi = zeros(layers,1);%zeros(1,layers);
rp_left = zeros(layers,1);
rp_left_ = zeros(layers,1);
tp_left = zeros(layers,1);
rp_right = zeros(layers,1);
tp_right = zeros(layers,1);

rs_left = zeros(layers,1);
rs_left_ = zeros(layers,1);
ts_left = zeros(layers,1);
rs_right = zeros(layers,1);
ts_right = zeros(layers,1);

d(2) = d_substrate;

x = 1;
phi(x) = phi0*pi/180;
kz(x) = 2*pi*n(x)/lambda*cos(phi(x));
beta(x) = d(x)*kz(x);
L(:,:,x) = [exp(-1i*beta(x)) 0; 0 exp(1i*beta(x))];

rp = zeros(1,layers-1);
tp = zeros(1,layers-1);
Ip = zeros(2,2,layers);
```

```
for x = 2:layers
    phi(x) = asin(n(x-1)*sin(phi(x-1))/n(x));
    kz(x) = 2*pi*n(x)/lambda*cos(phi(x));
    beta(x) = d(x)*kz(x);
    L(:,:,x) = [exp(-1i*beta(x)) 0; 0 exp(1i*beta(x))];

    rp(x-1) = -(n(x)*cos(phi(x-1))-n(x-1)*cos(phi(x)))/(n(x)*cos(phi(x-1))+n(x-
1)*cos(phi(x))); % doesn't match paper convention, but is correct
    rs(x-1) = (n(x)*cos(phi(x))-n(x-1)*cos(phi(x-1)))/(n(x)*cos(phi(x))+n(x-
1)*cos(phi(x-1))); % doesn't match paper convention, but is correct

    tp(x-1) = 2*n(x-1)*cos(phi(x-1))/(n(x)*cos(phi(x-1))+n(x-1)*cos(phi(x)));
    ts(x-1) = 2*n(x-1)*cos(phi(x-1))/(n(x)*cos(phi(x))+n(x-1)*cos(phi(x-1)));

    Ip(:,:,x-1) = 1/tp(x-1)*[1 rp(x-1); rp(x-1) 1];
    Is(:,:,x-1) = 1/ts(x-1)*[1 rs(x-1); rs(x-1) 1];
end

x0 = 3;             % first layer of coherent stack
xend = layers-1;    % last layer of coherent stack
xb   = xend;

% P-polarized (TM)
Sp_left = Ip(:,:,x0-1);
Sp_right = Ip(:,:,xend);
rp_left(x0)  = Sp_left(2,1)/Sp_left(1,1);
rp_left_(x0) = -Sp_left(1,2)/Sp_left(1,1);
tp_left(x0)  = 1/Sp_left(1,1);
rp_right(xend) = Sp_right(2,1)/Sp_right(1,1);
tp_right(xend) = 1/Sp_right(1,1);

% S-polarized (TE)
Ss_left = Is(:,:,x0-1);
Ss_right = Is(:,:,xend);
rs_left(x0)  = Ss_left(2,1)/Ss_left(1,1);
rs_left_(x0) = -Ss_left(1,2)/Ss_left(1,1);
ts_left(x0)  = 1/Ss_left(1,1);
rs_right(xend) = Ss_right(2,1)/Ss_right(1,1);
ts_right(xend) = 1/Ss_right(1,1);

for x = x0:xend
    xb = xb-1;

    % P-polarized (TM)
    Sp_left = Sp_left*L(:,:,x)*Ip(:,:,x);
    Sp_right = Ip(:,:,xb)*L(:,:,xb+1)*Sp_right;
    rp_left(x+1)  = Sp_left(2,1)/Sp_left(1,1);
    rp_left_(x+1) = -Sp_left(1,2)/Sp_left(1,1);
    tp_left(x+1)  = 1/Sp_left(1,1);
    rp_right(xb) = Sp_right(2,1)/Sp_right(1,1);
    tp_right(xb) = 1/Sp_right(1,1);
```

```
    % S-polarized (TE)
    Ss_left = Ss_left*L(:,:,x)*Is(:,:,x);
    Ss_right = Is(:,:,xb)*L(:,:,xb+1)*Ss_right;
    rs_left(x+1)  = Ss_left(2,1)/Ss_left(1,1);
    rs_left_(x+1) = -Ss_left(1,2)/Ss_left(1,1);
    ts_left(x+1)  = 1/Ss_left(1,1);
    rs_right(xb) = Ss_right(2,1)/Ss_right(1,1);
    ts_right(xb) = 1/Ss_right(1,1);

end
Ib23p = incov(Sp_left);
Ib23s = incov(Ss_left);

tpp = tp_left(1:xend)./(1-
rp_left_(1:xend).*rp_right(1:xend).*exp(1i.*2.*xi(1:xend).*d(1:xend)));
tmp = tpp(1:xend).*rp_right(1:xend).*exp(1i.*2.*xi(1:xend).*d(1:xend));
tps = ts_left(1:xend)./(1-
rs_left_(1:xend).*rs_right(1:xend).*exp(1i.*2.*xi(1:xend).*d(1:xend)));
tms = tps(1:xend).*rs_right(1:xend).*exp(1i.*2.*xi(1:xend).*d(1:xend));

% Account for incoherent front substrate
Ibp(:,:,1) = incov(Ip(:,:,1));
Ibs(:,:,1) = incov(Is(:,:,1));
Lb(:,:,2) = abs(L(:,:,2)).^2;

Sbp = Ibp(:,:,1)*Lb(:,:,2)*Ib23p;
Sbs = Ibs(:,:,1)*Lb(:,:,2)*Ib23s;
IglassITOp = [1,0]*Ib23p*[1/Sbp(1,1);0];
IglassITOs = [1,0]*Ib23s*[1/Sbs(1,1);0];

Rbfp = Sbp(2,1)/Sbp(1,1);  % Reflectance at the front interface
Tbfp = 1/Sbp(1,1);         % Transmittance at the front interface

Rbfs = Sbs(2,1)/Sbs(1,1);  % Reflectance at the front interface
Tbfs = 1/Sbs(1,1);         % Transmittance at the front interface

    if polarization == 'TM'

        Ri = Rbfp;
        Ti = Tbfp*real(n(end))/n(1);
        Ai = 1-Ri-Ti;

    elseif polarization == 'TE'

        Ri = Rbfs;
        Ti = Tbfs*real(n(end))/n(1);
        Ai = 1-Ri-Ti;

    end
end
%% Diffusion Calculations %%
```

```
function [pf, flux, flux_pop, G_Abs_tot, G_F_tot, k_F_tot, recomb_tot] =
DriftDiffusion(D, tau, G_Abs, G_F, k_F, eta_cc, R, d, type)
% Feng-Ghosh Model (Modified to include Forster Transfer)
% ddLd^2/tau*d^2(p)/(dz)^2 - p/tau + G_Abs - k_F*p + G_F = dp/dt

global dz

ddn = length(d);      % total number of mesh points in layer
p0 = zeros(ddn, 1);   % presize the population density vector

%% Calculate S.S. Exciton Population and Flux to HJs

M = zeros(ddn);   %Initialize matrix with governing equation for each mesh point
A = zeros(ddn,1); %Initialize right-hand-side vector

switch upper(type)

    %% Reflect Left, Dissociate (Quench) Right %%
    case {'RD','RQ'}
        M(1,1) = -(2 + dz^2/(D *tau(1)) + k_F(1)*dz^2/D); %First row zero flux
        M(1,2) = 2;

        M(ddn,ddn) = 1; %Zero value at right

        for i = 2:ddn-1
            for j = 1:ddn
                if i==j
                    M(i,j) = -(2 + dz^2/(D*tau(i)) + k_F(i)*dz^2/D);
                elseif i == j+1
                    M(i,j) = 1;
                elseif i == j-1
                    M(i,j) = 1;
                end
            end
        end

        A(2) = -dz^2/D*(G_Abs(1) + G_Abs(2) + G_F(1) + G_F(2));
        for i = 3:ddn - 2
            A(i) = -dz^2/D*(G_Abs(i)+G_F(i));
        end
        A(ddn-1) = -dz^2/D*(G_Abs(ddn-1) + G_Abs(ddn) + G_F(ddn-1) + G_F(ddn));

    %% Dissociate (Quench) Left, Reflect Right
    case {'DR','QR'}
        M(1,1) = 1; %Zero value at left
        M(ddn,ddn) = -(2 + dz^2/(D*tau(ddn)) + k_F(ddn)*dz^2/D);; %Last row zero flux
        M(ddn,ddn-1) = 2;
        for i = 2:ddn-1
            for j = 1:ddn
                if i==j
                    M(i,j) = -(2 + dz^2/(D*tau(i)) + k_F(i)*dz^2/D);
                elseif i == j+1
```

```
                M(i,j) = 1;
            elseif i == j-1
                M(i,j) = 1;
            end
        end
    end

    A(2) = -dz^2/D*(G_Abs(1) + G_Abs(2) + G_F(1) + G_F(2));
    for i = 3:ddn
        A(i) = -dz^2/D*(G_Abs(i)+G_F(i));
    end

%% Dissociate (Quench) Left & Right
case {'DD','DQ','QD','QQ'}
    M(1,1) = 1; %Zero value at left
    M(ddn,ddn) = 1; %Zero value at right

    for i = 2:ddn-1
        for j = 1:ddn
            if i==j
                M(i,j) = -(2 + dz^2/(D*tau(i)) + k_F(i)*dz^2/D);
            elseif i == j+1
                M(i,j) = 1;
            elseif i == j-1
                M(i,j) = 1;
            end
        end
    end

    A(2) = -dz^2/D*(G_Abs(1) + G_Abs(2) + G_F(1) + G_F(2));
    for i = 3:ddn - 2
        A(i) = -dz^2/D*(G_Abs(i)+G_F(i));
    end
    A(ddn-1) = -dz^2/D*(G_Abs(ddn-1) + G_Abs(ddn) + G_F(ddn-1) + G_F(ddn));

%% Reflect Left & Right
case {'RR'}
    M(1,1) = -(2 + dz^2/(D*tau(1)) + k_F(1)*dz^2/D); %First row zero flux
    M(1,2) = 2;
    M(ddn,ddn) = -(2 + dz^2/(D*tau(ddn)) + k_F(ddn)*dz^2/D); %Last row zero flux
    M(ddn,ddn-1) = 2;
    for i = 2:ddn-1
        for j = 1:ddn
            if i==j
                M(i,j) = -(2 + dz^2/(D*tau(i)) + k_F(i)*dz^2/D);
            elseif i == j+1
                M(i,j) = 1;
            elseif i == j-1
                M(i,j) = 1;
            end
        end
    end
```

```
        for i = 1:ddn
            A(i) = -dz^2/D*(G_Abs(i)+G_F(i));
        end

    %% Bulk Heterojunction
    case {'BHJ'}
        M = 1;
        A = 0;
end

%% Solve Matrix for S.S. Exciton Population
pf = p0;
pf = M\A;

%% Calculate Total Incident Photons in Layer (i.e. Flux to HJ if IQE=1)
flux_pop = 0;
G_Abs_tot = 0;
G_F_tot = 0;
k_F_tot = 0;
recomb_tot = 0;

for i = 1:ddn
    G_Abs_tot = G_Abs_tot + (G_Abs(i))*dz;
    G_F_tot = G_F_tot + G_F(i)*dz; %gui
    k_F_tot = k_F_tot + pf(i)*k_F(i)*dz;
    recomb_tot = recomb_tot + pf(i)/tau(i)*dz; %gui
end

%% Calculate Flux to HJ(s)
switch upper(type)
    case {'RD','QD'}
        flux = D*abs(pf(ddn)-pf(ddn-1))/(1*dz);
    case {'DR','DQ'}
        flux = D*abs(pf(1)-pf(2))/(1*dz);
    case {'DD'}
        flux = D*(abs(pf(1)-pf(2))/(dz) + abs(pf(ddn)-pf(ddn-1))/dz);
    case {'RQ','QR','QQ','RR'}
        flux = 0;
    case {'BHJ'}
        flux = eta_cc.*(G_Abs_tot+G_F_tot);
end

end
%% Photon Density AM1.5G %%
function N = photonDens(WL)
global c h

% wavelength for given power density data (in nm)
dataWL = [*data removed to save space];
% power density at AM1.5 (Global Tilt) according to ASTMG173 (W/m^2/nm)
pd_global_tilt = [*data removed to save space];
```

```
s = length(dataWL);

for i = 2:s(1,1)
    pd = pd_global_tilt(i)*(dataWL(i)-(dataWL(i-1)))/1E9; %Irradiance (W/m^2)
    nd(i) = pd./(h*c/dataWL(i)); %Photon flux
end
nd(1) = nd(2);

% interpolate the power density for the desired input wavelengths
N = interp1(dataWL,nd,WL,'linear','extrap');

end
```

Bibliography

1 Gledhill, S. E., Scott, B. & Gregg, B. A. Organic and nano-structured composite photovoltaics: An overview. *Journal of Materials Research* **20**, 3167-3179, doi:10.1557/jmr.2005.0407 (2011).

2 Hoppe, H. & Sariciftci, N. S. Organic solar cells: An overview. *Journal of Materials Research* **19**, 1924-1945, doi:10.1557/jmr.2004.0252 (2011).

3 Yue, D., Khatav, P., You, F. & Darling, S. B. Deciphering the uncertainties in life cycle energy and environmental analysis of organic photovoltaics. *Energy & Environmental Science* **5**, 9163, doi:10.1039/c2ee22597b (2012).

4 Darling, S. B. & You, F. The case for organic photovoltaics. *RSC Advances* **3**, 17633, doi:10.1039/c3ra42989j (2013).

5 Brabec, C. J. Organic photovoltaics: technology and market. *Solar Energy Materials and Solar Cells* **83**, 273-292, doi:10.1016/j.solmat.2004.02.030 (2004).

6 Che, X., Xiao, X., Zimmerman, J. D., Fan, D. & Forrest, S. R. High-Efficiency, Vacuum-Deposited, Small-Molecule Organic Tandem and Triple-Junction Photovoltaic Cells. *Advanced Energy Materials* **4**, n/a-n/a, doi:10.1002/aenm.201400568 (2014).

7 Tang, C. W. Two-layer organic photovoltaic cell. *Applied Physics Letters* **48**, 183-185, doi:10.1063/1.96937 (1986).

8 Menke, S. M. & Holmes, R. J. Exciton diffusion in organic photovoltaic cells. *Energy Environ. Sci.* **7**, 499-512, doi:10.1039/c3ee42444h (2014).

9 Gregg, B. A. Excitonic Solar Cells. *The Journal of Physical Chemistry B* **107**, 4688-4698, doi:10.1021/jp022507x (2003).

10 Pettersson, L. A. A., Roman, L. S. & Inganäs, O. Modeling photocurrent action spectra of photovoltaic devices based on organic thin films. *Journal of Applied Physics* **86**, 487, doi:10.1063/1.370757 (1999).

11 Peumans, P., Yakimov, A. & Forrest, S. R. Small molecular weight organic thin-film photodetectors and solar cells. *Journal of Applied Physics* **93**, 3693, doi:10.1063/1.1534621 (2003).

12 Ghosh, A. K. & Feng, T. Merocynanine organic solar cells. *Journal of Applied Physics* **49**, 5982, doi:10.1063/1.324566 (1978).

13 Chen, W., Nikiforov, M. P. & Darling, S. B. Morphology characterization in organic and hybrid solar cells. *Energy & Environmental Science* **5**, 8045, doi:10.1039/c2ee22056c (2012).
14 Yu, G., Gao, J., Hummelen, J. C., Wudl, F. & Heeger, A. J. Polymer Photovoltaic Cells: Enhanced Efficiencies via a Network of Internal Donor-Acceptor Heterojunctions. *Science* **270**, 1789-1791, doi:10.1126/science.270.5243.1789 (1995).
15 Chen, G. *et al*. Co-evaporated bulk heterojunction solar cells with >6.0% efficiency. *Adv Mater* **24**, 2768-2773, doi:10.1002/adma.201200234 (2012).
16 Pandey, R., Zou, Y. & Holmes, R. J. Efficient, bulk heterojunction organic photovoltaic cells based on boron subphthalocyanine chloride-C70. *Applied Physics Letters* **101**, 033308, doi:10.1063/1.4737902 (2012).
17 Halls, J. J. M. *et al*. Efficient photodiodes from interpenetrating polymer networks. *Nature* **376**, 498-500, doi:10.1038/376498a0 (1995).
18 Yakimov, A. & Forrest, S. R. High photovoltage multiple-heterojunction organic solar cells incorporating interfacial metallic nanoclusters. *Applied Physics Letters* **80**, 1667, doi:10.1063/1.1457531 (2002).
19 Lassiter, B. E., Kyle Renshaw, C. & Forrest, S. R. Understanding tandem organic photovoltaic cell performance. *Journal of Applied Physics* **113**, 214505, doi:10.1063/1.4807910 (2013).
20 Pandey, R. & Holmes, R. J. Characterizing the charge collection efficiency in bulk heterojunction organic photovoltaic cells. *Applied Physics Letters* **100**, 083303, doi:10.1063/1.3686909 (2012).
21 Braun, C. L. Electric field assisted dissociation of charge transfer states as a mechanism of photocarrier production. *The Journal of Chemical Physics* **80**, 4157, doi:10.1063/1.447243 (1984).
22 Peumans, P. & Forrest, S. R. Very-high-efficiency double-heterostructure copper phthalocyanine/C[sub 60] photovoltaic cells. *Applied Physics Letters* **79**, 126, doi:10.1063/1.1384001 (2001).
23 Peumans, P. & Forrest, S. R. Separation of geminate charge-pairs at donor–acceptor interfaces in disordered solids. *Chemical Physics Letters* **398**, 27-31, doi:10.1016/j.cplett.2004.09.030 (2004).
24 Chan, M. Y., Lai, S. L., Lau, K. M., Lee, C. S. & Lee, S. T. Application of metal-doped organic layer both as exciton blocker and optical spacer for organic photovoltaic devices. *Applied Physics Letters* **89**, 163515, doi:10.1063/1.2362974 (2006).
25 Gebeyehu, D. *et al*. Highly efficient p–i–n type organic photovoltaic devices. *Thin Solid Films* **451-452**, 29-32, doi:10.1016/j.tsf.2003.10.087 (2004).
26 Lassiter, B. E. *et al*. Organic photovoltaics incorporating electron conducting exciton blocking layers. *Applied Physics Letters* **98**, 243307, doi:10.1063/1.3598426 (2011).
27 Yi, Y. *et al*. The interface state assisted charge transport at the MoO(3)/metal interface. *J Chem Phys* **130**, 094704, doi:10.1063/1.3077289 (2009).
28 Shrotriya, V., Li, G., Yao, Y., Chu, C.-W. & Yang, Y. Transition metal oxides as the buffer layer for polymer photovoltaic cells. *Applied Physics Letters* **88**, 073508, doi:10.1063/1.2174093 (2006).
29 Hiroshi Kageyama, H. K., Yutaka Ohmori, and Yasuhiko Shirota. MoO3 as a Cathod Buffer Layer Material for the Improvement of Planar pn-Heterojunction Organic Solar

Cell Performance. *Applied Physics Express* **4**, 032301, doi:10.1143/APEX.4.032301 (2011).
30 van Dijken, A., Perro, A., Meulenkamp, E. A. & Brunner, K. The influence of a PEDOT:PSS layer on the efficiency of a polymer light-emitting diode. *Organic Electronics* **4**, 131-141, doi:10.1016/j.orgel.2003.08.007 (2003).
31 Hirade, M. & Adachi, C. Small molecular organic photovoltaic cells with exciton blocking layer at anode interface for improved device performance. *Applied Physics Letters* **99**, 153302, doi:10.1063/1.3650472 (2011).
32 Zhang, G. *et al*. Cascade-energy-level alignment based organic photovoltaic cells by utilizing copper phthalocyanine as bipolar carrier transporting layer. *Applied Physics Letters* **94**, 143302, doi:10.1063/1.3114379 (2009).
33 Cnops, K., Rand, B. P., Cheyns, D. & Heremans, P. Enhanced photocurrent and open-circuit voltage in a 3-layer cascade organic solar cell. *Applied Physics Letters* **101**, 143301, doi:10.1063/1.4757575 (2012).
34 Heidel, T. D. *et al*. Reducing recombination losses in planar organic photovoltaic cells using multiple step charge separation. *Journal of Applied Physics* **109**, 104502, doi:10.1063/1.3585863 (2011).
35 Hong, Z. R. *et al*. Antenna effects and improved efficiency in multiple heterojunction photovoltaic cells based on pentacene, zinc phthalocyanine, and C[sub 60]. *Journal of Applied Physics* **106**, 064511, doi:10.1063/1.3187904 (2009).
36 Schlenker, C. W. *et al*. Cascade Organic Solar Cells. *Chemistry of Materials* **23**, 4132-4140, doi:10.1021/cm200525h (2011).
37 Griffith, O. L. & Forrest, S. R. Exciton management in organic photovoltaic multidonor energy cascades. *Nano Lett* **14**, 2353-2358, doi:10.1021/nl501112z (2014).
38 Verreet, B. *et al*. The characterization of chloroboron (iii) subnaphthalocyanine thin films and their application as a donor material for organic solar cells. *Journal of Materials Chemistry* **19**, 5295, doi:10.1039/b902342a (2009).
39 Gommans, H. H. P. *et al*. Electro-Optical Study of Subphthalocyanine in a Bilayer Organic Solar Cell. *Advanced Functional Materials* **17**, 2653-2658, doi:10.1002/adfm.200700398 (2007).
40 Giebink, N. C., Lassiter, B. E., Wiederrecht, G. P., Wasielewski, M. R. & Forrest, S. R. Ideal diode equation for organic heterojunctions. II. The role of polaron pair recombination. *Physical Review B* **82**, doi:10.1103/PhysRevB.82.155306 (2010).
41 Morris, S. E. & Shtein, M. High efficiency organic photovoltaic cells based on inverted SubPc/C60/ITO cascade junctions. *Organic Electronics* **15**, 3795-3799, doi:10.1016/j.orgel.2014.08.046 (2014).
42 Kulshreshtha, C. *et al*. New interfacial materials for rapid hole-extraction in organic photovoltaic cells. *Journal of Materials Chemistry A* **1**, 4077, doi:10.1039/c3ta00808h (2013).
43 Greiner, M. T. *et al*. Universal energy-level alignment of molecules on metal oxides. *Nat Mater* **11**, 76-81, doi:10.1038/nmat3159 (2012).
44 Kahn, A., Koch, N. & Gao, W. Electronic structure and electrical properties of interfaces between metals and ?-conjugated molecular films. *Journal of Polymer Science Part B: Polymer Physics* **41**, 2529-2548, doi:10.1002/polb.10642 (2003).

45 Mutolo, K. L., Mayo, E. I., Rand, B. P., Forrest, S. R. & Thompson, M. E. Enhanced open-circuit voltage in subphthalocyanine/C60 organic photovoltaic cells. *J Am Chem Soc* **128**, 8108-8109, doi:10.1021/ja061655o (2006).
46 Dresselhaus, M. S., Dresselhaus, G. & Eklund, P. C. *Science of Fullerenes and Carbon Nanotubes*. 484 (Academic, 1996).
47 Luhman, W. A. & Holmes, R. J. Investigation of Energy Transfer in Organic Photovoltaic Cells and Impact on Exciton Diffusion Length Measurements. *Advanced Functional Materials* **21**, 764-771, doi:10.1002/adfm.201001928 (2011).
48 Centurioni, E. Generalized matrix method for calculation of internal light energy flux in mixed coherent and incoherent multilayers. *Applied Optics* **44**, 7532, doi:10.1364/ao.44.007532 (2005).
49 Gommans, H. *et al*. On the Role of Bathocuproine in Organic Photovoltaic Cells. *Advanced Functional Materials* **18**, 3686-3691, doi:10.1002/adfm.200800815 (2008).
50 Lunt, R. R., Giebink, N. C., Belak, A. A., Benziger, J. B. & Forrest, S. R. Exciton diffusion lengths of organic semiconductor thin films measured by spectrally resolved photoluminescence quenching. *Journal of Applied Physics* **105**, 053711, doi:10.1063/1.3079797 (2009).
51 Kawamura, Y., Sasabe, H. & Adachi, C. Simple Accurate System for Measuring Absolute Photoluminescence Quantum Efficiency in Organic Solid-State Thin Films. *Japanese Journal of Applied Physics* **43**, 7729-7730, doi:10.1143/jjap.43.7729 (2004).
52 Byrne, H. J. *et al*. Time-resolved photoluminescence of solid state fullerenes. *Chemical Physics Letters* **204**, 461-466, doi:10.1016/0009-2614(93)89187-m (1993).
53 Xiao, X., Zimmerman, J. D., Lassiter, B. E., Bergemann, K. J. & Forrest, S. R. A hybrid planar-mixed tetraphenyldibenzoperiflanthene/C70 photovoltaic cell. *Applied Physics Letters* **102**, 073302, doi:10.1063/1.4793195 (2013).
54 Beaumont, N. *et al*. Boron Subphthalocyanine Chloride as an Electron Acceptor for High-Voltage Fullerene-Free Organic Photovoltaics. *Advanced Functional Materials* **22**, 561-566, doi:10.1002/adfm.201101782 (2012).
55 Giebink, N. C., Wiederrecht, G. P., Wasielewski, M. R. & Forrest, S. R. Ideal diode equation for organic heterojunctions. I. Derivation and application. *Physical Review B* **82**, doi:10.1103/PhysRevB.82.155305 (2010).
56 Pandey, R., Gunawan, A. A., Mkhoyan, K. A. & Holmes, R. J. Efficient Organic Photovoltaic Cells Based on Nanocrystalline Mixtures of Boron Subphthalocyanine Chloride and C60. *Advanced Functional Materials* **22**, 617-624, doi:10.1002/adfm.201101948 (2012).
57 Gurney, N. F. M. a. R. W. *Electronic Processes in Ionic Crystals*. (Oxford University Press, 1940).
58 van Mensfoort, S. L. M., Shabro, V., de Vries, R. J., Janssen, R. A. J. & Coehoorn, R. Hole transport in the organic small molecule material α-NPD: evidence for the presence of correlated disorder. *Journal of Applied Physics* **107**, 113710, doi:10.1063/1.3407561 (2010).
59 Renshaw, C. K., Zimmerman, J. D., Lassiter, B. E. & Forrest, S. R. Photoconductivity in donor-acceptor heterojunction organic photovoltaics. *Physical Review B* **86**, doi:10.1103/PhysRevB.86.085324 (2012).

60 Sim, M., Kim, J. S., Shim, C. & Cho, K. Cascade organic solar cells with energy-level-matched three photon-harvesting layers. *Chemical Physics Letters* **557**, 88-91, doi:10.1016/j.cplett.2012.11.087 (2013).
61 Barito, A. *et al*. Recovering lost excitons in organic photovoltaics using a transparent dissociation layer. *Journal of Applied Physics* **113**, 203110, doi:10.1063/1.4807416 (2013).
62 Foertig, A. *et al*. Nongeminate Recombination in Planar and Bulk Heterojunction Organic Solar Cells. *Advanced Energy Materials* **2**, 1483-1489, doi:10.1002/aenm.201200718 (2012).
63 Tress, W., Leo, K. & Riede, M. Influence of Hole-Transport Layers and Donor Materials on Open-Circuit Voltage and Shape of I-V Curves of Organic Solar Cells. *Advanced Functional Materials* **21**, 2140-2149, doi:10.1002/adfm.201002669 (2011).
64 Cheyns, D. *et al*. Analytical model for the open-circuit voltage and its associated resistance in organic planar heterojunction solar cells. *Physical Review B* **77**, doi:10.1103/PhysRevB.77.165332 (2008).
65 Seaman, C. H. Calibration of solar cells by the reference cell method—The spectral mismatch problem. *Solar Energy* **29**, 291-298, doi:10.1016/0038-092x(82)90244-4 (1982).
66 Guan, Z.-L. *et al*. Direct determination of the electronic structure of the poly(3-hexylthiophene):phenyl-[6,6]-C61 butyric acid methyl ester blend. *Organic Electronics* **11**, 1779-1785, doi:10.1016/j.orgel.2010.07.023 (2010).
67 Tong, X., Lassiter, B. E. & Forrest, S. R. Inverted organic photovoltaic cells with high open-circuit voltage. *Organic Electronics* **11**, 705-709, doi:10.1016/j.orgel.2009.12.024 (2010).
68 Tseng, Y.-C., Mane, A. U., Elam, J. W. & Darling, S. B. Ultrathin molybdenum oxide anode buffer layer for organic photovoltaic cells formed using atomic layer deposition. *Solar Energy Materials and Solar Cells* **99**, 235-239, doi:10.1016/j.solmat.2011.12.004 (2012).
69 Rand, B., Burk, D. & Forrest, S. Offset energies at organic semiconductor heterojunctions and their influence on the open-circuit voltage of thin-film solar cells. *Physical Review B* **75**, doi:10.1103/PhysRevB.75.115327 (2007).
70 Zhang, M., Wang, H. & Tang, C. W. Effect of the highest occupied molecular orbital energy level offset on organic heterojunction photovoltaic cells. *Applied Physics Letters* **97**, 143503, doi:10.1063/1.3491214 (2010).
71 Onsager, L. Initial Recombination of Ions. *Physical Review* **54**, 554-557, doi:10.1103/PhysRev.54.554 (1938).
72 Wagenpfahl, A., Rauh, D., Binder, M., Deibel, C. & Dyakonov, V. S-shaped current-voltage characteristics of organic solar devices. *Physical Review B* **82**, doi:10.1103/PhysRevB.82.115306 (2010).
73 Glatthaar, M. *et al*. Efficiency limiting factors of organic bulk heterojunction solar cells identified by electrical impedance spectroscopy. *Solar Energy Materials and Solar Cells* **91**, 390-393, doi:10.1016/j.solmat.2006.10.020 (2007).
74 Lilliedal, M. R., Medford, A. J., Madsen, M. V., Norrman, K. & Krebs, F. C. The effect of post-processing treatments on inflection points in current–voltage curves of roll-to-roll processed polymer photovoltaics. *Solar Energy Materials and Solar Cells* **94**, 2018-2031, doi:10.1016/j.solmat.2010.06.007 (2010).

75 Uhrich, C. *et al*. Origin of open circuit voltage in planar and bulk heterojunction organic thin-film photovoltaics depending on doped transport layers. *Journal of Applied Physics* **104**, 043107, doi:10.1063/1.2973199 (2008).
76 Schlenker, C. W. & Thompson, M. E. The molecular nature of photovoltage losses in organic solar cells. *Chem Commun (Camb)* **47**, 3702-3716, doi:10.1039/c0cc04020g (2011).
77 Yang, J. & Shen, J. Effects of the hole barrier in bilayer organic light-emitting devices. *Journal of Physics D: Applied Physics* **33**, 1768-1772, doi:10.1088/0022-3727/33/15/303 (2000).
78 Matsumoto, N. & Adachi, C. Exciplex Formations at the HTL/Alq3Interface in an Organic Light-Emitting Diode: Influence of the Electron–Hole Recombination Zone and Electric Field. *The Journal of Physical Chemistry C* **114**, 4652-4658, doi:10.1021/jp9121062 (2010).
79 Liu, F., Paul Ruden, P., Campbell, I. H. & Smith, D. L. Exciplex current mechanism for ambipolar bilayer organic light emitting diodes. *Applied Physics Letters* **99**, 123301, doi:10.1063/1.3640232 (2011).
80 Verreet, B. *et al*. Decreased Recombination Through the Use of a Non-Fullerene Acceptor in a 6.4% Efficient Organic Planar Heterojunction Solar Cell. *Advanced Energy Materials*, n/a-n/a, doi:10.1002/aenm.201301413 (2014).
81 Cnops, K. *et al*. 8.4% efficient fullerene-free organic solar cells exploiting long-range exciton energy transfer. *Nat Commun* **5**, 3406, doi:10.1038/ncomms4406 (2014).
82 Kulshreshtha, C. *et al*. Open-circuit voltage dependency on hole-extraction layers in planar heterojunction organic solar cells. *Applied Physics Letters* **99**, 023308, doi:10.1063/1.3610962 (2011).
83 Noh, S., Suman, C. K., Hong, Y. & Lee, C. Carrier conduction mechanism for phosphorescent material doped organic semiconductor. *Journal of Applied Physics* **105**, 033709, doi:10.1063/1.3072693 (2009).
84 Fleissner, A., Schmid, H., Melzer, C. & von Seggern, H. Trap-controlled hole transport in small molecule organic semiconductors. *Applied Physics Letters* **91**, 242103, doi:10.1063/1.2820448 (2007).
85 Kageyama, H., Ohishi, H., Tanaka, M., Ohmori, Y. & Shirota, Y. High-Performance Organic Photovoltaic Devices Using a New Amorphous Molecular Material with High Hole Drift Mobility, Tris[4-(5-phenylthiophen-2-yl)phenyl]amine. *Advanced Functional Materials* **19**, 3948-3955, doi:10.1002/adfm.200901259 (2009).
86 Borsenberger, P. M., Pautmeier, L., Richert, R. & Bässler, H. Hole transport in 1,1-bis(di-4-tolylaminophenyl)cyclohexane. *The Journal of Chemical Physics* **94**, 8276, doi:10.1063/1.460112 (1991).
87 Frenkel, J. On Pre-Breakdown Phenomena in Insulators and Electronic Semi-Conductors. *Physical Review* **54**, 647-648, doi:10.1103/PhysRev.54.647 (1938).
88 Scully, S. R., Armstrong, P. B., Edder, C., Fréchet, J. M. J. & McGehee, M. D. Long-Range Resonant Energy Transfer for Enhanced Exciton Harvesting for Organic Solar Cells. *Advanced Materials* **19**, 2961-2966, doi:10.1002/adma.200700917 (2007).
89 Menke, S. M., Luhman, W. A. & Holmes, R. J. Tailored exciton diffusion in organic photovoltaic cells for enhanced power conversion efficiency. *Nat Mater* **12**, 152-157, doi:10.1038/nmat3467 (2013).

90 Barito, A. *et al*. Universal Design Principles for Cascade Heterojunction Solar Cells with High Fill Factors and Internal Quantum Efficiencies Approaching 100%. *Advanced Energy Materials*, n/a-n/a, doi:10.1002/aenm.201400216 (2014).
91 Sullivan, P. *et al*. Halogenated Boron Subphthalocyanines as Light Harvesting Electron Acceptors in Organic Photovoltaics. *Advanced Energy Materials* **1**, 352-355, doi:10.1002/aenm.201100036 (2011).
92 Vasseur, K. *et al*. Controlling the texture and crystallinity of evaporated lead phthalocyanine thin films for near-infrared sensitive solar cells. *ACS Appl Mater Interfaces* **5**, 8505-8515, doi:10.1021/am401933d (2013).